School of Civil and Mechanical Engineering School

An Innovative Lightweight Composite Sandwich Panel System for Prefabricated Buildings

Yanqiang Cui

The thesis is presented for the degree of

Doctor of Philosophy of

Curtin University

October 2020

Declaration

To the best of my knowledge and belief, this thesis contains no material previously published by another person except where due acknowledgment has been made.

This thesis contains no material which has been accepted for the award of any other degree or diploma in any university.

Signature:

Date: 13/10/2020

ABSTRACT

Traditional building construction methods involve a large amount of construction work on-site, which is time-consuming and has high associated labour costs. The prefabrication method can effectively reduce the overall costs, shorten construction time, and improve environmental performance regarding waste minimisation compared to traditional building construction methods. Panels are essential structural components of prefabricated buildings and the lightweight property is fundamental for enhancing the speed and convenience of delivery to site and quick assembly on site. In addition, eco-design and energy efficiency require new building construction solutions that are environmentally friendly and lead to reductions in material usage and energy consumption.

The primary objective of the present study is to develop an innovative lightweight panel system for prefabricated buildings considering sustainability and energy efficiency. To achieve this goal, the sandwich structural form is adopted. This study develops a new type of fibre-reinforced geopolymer (FRG) composite, and the mechanical properties and vibration characteristics of the FRG are studied. Fly ash and slag-based geopolymer binder are incorporated with the methylcellulose and the combination of copper coated micro steel fibres and high strength Polyethylene fibres to make the FRG. Results from experimental studies show that the developed FRG has excellent mechanical properties, including high compressive and flexural strengths and large deformation capability. Furthermore, damping of the material can be enhanced by the addition of methylcellulose.

A new type of lightweight sandwich panel with FRG skin layers and polyurethane (PUR) foam core is developed for prefabricated buildings. The failure mechanisms of the developed sandwich panel under point load and edgewise compressive load are studied. The failure modes under point load are core shear failure or skin tensile failure. The failure modes under edgewise compressive load are material failure or global buckling. Furthermore, the analytical models to predict the critical failure load under point load and edgewise compressive load are proposed and give reasonable predictions.

Structural performance and vibration characteristics of the developed full-size sandwich panel are further studied. Two types of sandwich panels are considered for flexural loading test. One without strengthening and another one is strengthened with Basalt Fibre Reinforced Polymer (BFRP) sheets on the FRG skin. Quasi-static four-point bending tests results show applying BFRP sheet can increase the critical failure load of the developed sandwich panel and change the failure mode from skin tensile failure to core shear failure. The hammer impact vibration test results show that applied BFRP sheet does not change the vibration characteristics significantly. The axial compressive loading test result shows that failure mode of the developed sandwich panel is governed by global buckling.

Vibration serviceability of a composite floor system for prefabricated buildings using the developed sandwich panels based on pedestrian loads is studied by finite element analysis. The structural floor system is composed of steel girders, beams, and developed sandwich panels. The simulation results under continuous walking load model show that the floor system can meet the vibration serviceability requirement for floor applications.

In summary, this study develops an innovative lightweight sandwich panel system with FRG skin and PUR foam core for prefabricated buildings considering sustainability and energy efficiency. It is made of industrial waste and good insulation materials, hence leads to low energy consumption in construction applications. It has good mechanical properties and reasonable vibration serviceability, light weight and low cost, therefore great potentials for application in prefabricated structures.

ACKNOWLEDGMENT

The completion of this thesis is attributed to the support and assistance of many people. First and foremost, I would like to extend my sincerest and deepest gratitude to my supervisor John Curtin Distinguished Professor Hong Hao for the continuous support, great patience, and invaluable encouragement throughout my study period for the PhD degree. Prof. Hong Hao also shows the kindness of a real great person to me. I will follow his kindness and provide the help for other people who need it in the rest of my life. In addition, I need to extend my heartfelt appreciation to my co-supervisor, Associate Prof. Jun Li, whose patient guidance, valuable suggestions and constant encouragement allowed me to successfully complete this thesis. Also, I would like to thank the help from Dr. Wensu Chen, whose kind help and professional instructions encouraged me to continue and complete my study.

I would also like to thank other instructors, Dr. Xihong Zhang and Dr. Kaiming Bi, for the advice, suggestions and invaluable help during this research. I am also thankful for the professional assistance and support from the staff in Civil Lab, and they are Mr. Mark Whittaker, Mr. Kevin Reilly, Mr. Gary Woodward and Dr. Arne Bredin. Special thanks also go to members from Prof. Hong Hao's research team, such as Dr. Xingyu Fan, Chao Li, Haoran Zuo, Zhejian Li, Chuang Cui, Lufeng Zhao, Lizhong Song, Ruisheng Ma, Cheng Yuan, Gao Fan, Yu Xin, Yijun Chen, Yuwen Chiu and Tung T. Tran.

Last but not least, I would like to express my deepest love to my family for the strength and encouragement that they give to me, especially my wife, Yixiao Zhang.

LIST OF PUBLICATIONS

Journal Papers:

Y. Cui, H. Hao, J. Li, W. Chen, Effect of Adding Methylcellulose on Mechanical and Vibration Properties of Geopolymer Paste and Hybrid Fiber-Reinforced Geopolymer Composite, Journal of Materials in Civil Engineering 32(7) (2020) 04020166.

Y. Cui, H. Hao, J. Li, W. Chen, Failure mechanism of geopolymer composite lightweight sandwich panel under flexural and edgewise compressive loads, Construction and Building Material (Accepted).

Conference Papers:

Y. Cui, H. Hao, J. Li, W. Chen, Mechanical properties of new short fiber reinforced geopolymer composite for skin of structural insulated Panels. Proceedings of the 13th International Conference on Steel, Space and Composite Structures SS18), (2018). Perth, Australia.

TABLE OF CONTENTS

LIST OF FIGURES

LIST OF TABLES

1 Introduction

1.1 Background

The motivation to design durable buildings that fulfil the imminent demands of prefabricated and sustainable manufacturing makes the application of new materials and production methods necessary. ‘Prefabricated housing’ refers to the construction process where the housing components are prefabricated in factories and are then shipped to sites for assembly. The panels are very important structural members of prefabricated houses and can be functionalised as the roof, wall panel, and floor panels. The lightweight properties of precast components are fundamental for enhancing the speed and convenience of delivery and assembly at the site and to decrease the building costs.

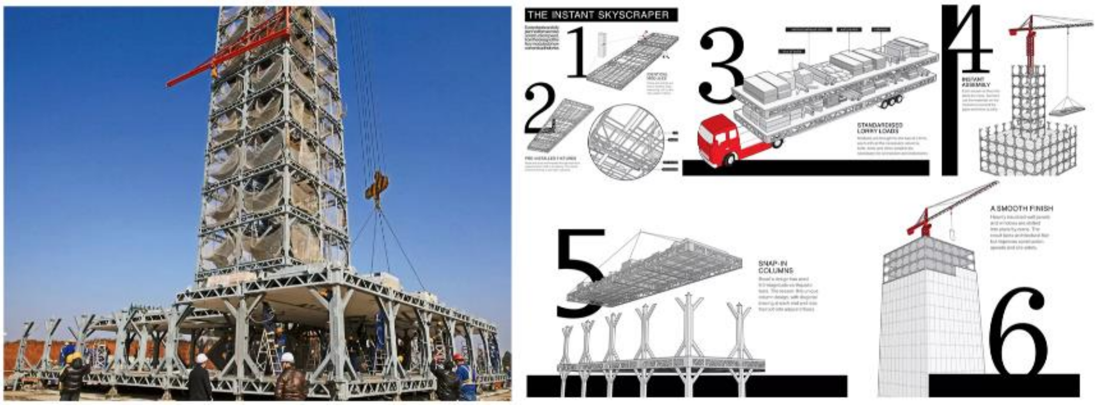

Figure 1.1 A 30-storey hotel built using the prefabrication technique (1)

The development of prefabrication and industrialisation for construction has promoted the development of innovative construction materials and technology. Based on the different maturity of the prefabrication process, which refers to the size and complexity of the prefabricated components or the configuration of the final product, the prefabricated structure can be categorised as either a panelised structure or modular structure (1). Regardless of the type of prefabricated structure, the panels are always the most fundamental component. Therefore, different types of lightweight panels have been developed for the prefabrication of buildings. For example, a 30-storey hotel near Dongting Lake in the Hunan Province of China was built in 15 days using the panel system. The panel system that was used for the floor and roof was a sandwich truss panel system (1) and the building process is shown in Figure 1.1.

One9, which are contemporary apartments built over nine storeys, were constructed using the modular prefabricated building method in Melbourne, Australia, in 2013. The manufactured apartments were erected by Vaughan and Hickory using 36 unitised building modules in just five days, with the daily schedule and progress shown in Figure 1.2 (1). The site was constrained by a nearby large shopping mall, which could not be disturbed during the construction period. The modular prefabrication building technique was the best solution to meet the client's need of constructing a 10-storey building in only a few days, which saved a significant amount of time because of the heavily congested suburb and limited working space. Another example of the modular prefabrication building method is the low-rise apartment 'Little Hero' in Melbourne. The Little Hero consists of 58 single-storey apartment modules and five double-storey apartment modules (Figure 1.3). It was assembled with finishes within 8 days in a site that had a very narrow space. The Little Hero is a noteworthy construction because it is one of the earliest multistorey modular constructions in Australia and the world (2).

Various materials have been adapted for the prefabrication building method, including concrete, steel, timber, and fibre reinforced polymer (FRP). Examples of main modular constructions made of different materials are shown in Figure 1.4. Steel-based construction is heavy and prone to damage from corrosion. Wood-based construction is prone to termite attack and swelling in floodwaters. Wooden construction can also be damaged by wind debris impact. Constructions using steel-reinforced concrete are labour-intensive and time-consuming, and steel reinforcements in structures are prone to corrosion. Wood, steel, and reinforced concrete show limitations in terms of poor thermal insulation, poor vibration serviceability, energy consumption, and labour-intensity. Hence, there is an emerging need for the development of innovative panels with new construction materials and techniques for prefabricated buildings. Innovative panels have been developed to satisfy the following properties: lightweight, good vibration serviceability, good insulation performance, and lower cost. Therefore, composite lightweight panels have drawn much attention for use in prefabricated buildings.

Figure 1.2 One9 apartment constructed by modular prefabricated building method (1)

Figure 1.3 The completed ‘Little Hero’ in Melbourne and during on-site assembly (2)

(a)

(b)

(c)

Figure 1.4 Modular prefabricated buildings using different materials (2): (a) FRP; (b) Concrete; (c) Lightweight steel

Eco-design and energy efficiency are also concepts that require searching for new building solutions that are environmentally friendly and lead to a reduction of materials and energy consumption (3). The United Nations Environmental Program (4) estimates that buildings consume approximately 40% of the global world energy, 25% of the global water, and 40% of the global resources. Buildings are also responsible for approximately 1/3 of greenhouse gas emissions of the entire planet. The U.S. Department of Energy (5) and the European Commission (6) also obtained similar conclusions from their studies. Therefore, building regulations impose a minimum level of energy efficiency for all new buildings and, in some cases, retrofitted buildings to decrease the energy demand of buildings. For example, Europe imposes the Energy Performance of Building Directive (7) together with the Energy Efficiency Directive (8), and Australia imposes the 6 Star Standard (9). Heating and cooling demands contribute to the most significant energy consumptions for the building industry and this demand is increasing based on research by the European Commission (10). Therefore, enhancing the insulation properties of building envelopes is one of the most effective strategies to reduce the energy consumption caused by the heating and cooling demand of buildings (11), and this method could play a decisive role because it could lead to significant improvements with low pay-back time (12, 13). To achieve better insulation properties of building envelopes, thermal insulation materials with low thermal conductivity have been developed and are widely used by building industries. Previous studies have shown that the most commonly used thermal insulation materials include mineral wool, cork, cellulose, expanded polystyrene

(EPS), extruded polystyrene (XPS), and polyurethane (PUR) (14, 15). Mineral wool covers glass wool (fibreglass) and rock wool. PUR is produced by a reaction between isocyanates and polyols and is usually applied as a board; however, it may also be used as an expanding foam agent at the building site to seal windows, doors, and other cavities. The typical thermal conductivity values of PUR foam are between 20 and 30 mW/(mK), which are considerably lower than mineral wool, cork, cellulose, EPS, and XPS products (15).

Another one of the significant contributors of buildings to environmental problems is the consumption of the cement-based product, with the massive CO_2 emissions caused by this consumption exacerbating global warming. When manufacturing one tonne of ordinary Portland cement (OPC), approximately 0.8 tonnes of CO_2 are emitted into the atmosphere (16). OPC production contributes approximately 5%–7% of global CO_2 emissions and is a highly energy-intensive process (17). Consequently, the concept of replacing OPC material with environment-friendly material has drawn increasing attention. Geopolymers can be obtained from a geological source or by-products from an industrial process, such as fly ash and slag, and it can react with alkaline liquid to form a strong polymer binder (18). As an innovative type of environment-friendly material, geopolymers are promising as supplementary materials to replace OPC in those building industries that are concerned with sustainability.

Based on the above discussion, the energy consumption and the influence of environment for building industry include two aspects: the massive application of cement-based material and the energy for heating and cooling the buildings. As a result, the exploration of innovative materials and structures which can reduce the cement-based material and decrease the energy loss for heating and cooling building, can lead to low energy consumption in construction applications.

In summary, the development of prefabrication and the industrialisation of buildings has driven the new requirements of building components, not only for structural purposes but also for functional purposes. This trend has induced the exploration of innovative materials and structural types that are suitable for prefabricated buildings regarding their sustainability and eco-design concepts. As a result, the exploration of an innovative lightweight panel system which can be used as the wall, roof and/or floor is beneficial for the development and application of prefabricated buildings. The structural behaviour and vibration characteristics of the lightweight panel system need to be studied thoroughly to understand the structural performance and vibration serviceability when the developed sandwich panel is used in construction.

1.2 Research objectives of this dissertation

The primary objective of the present study is to develop an innovative lightweight panel system to be used for prefabricated buildings considering the sustainability and energy efficiency. To achieve this primary goal, first, the sandwich structure type was adopted as it has high strength-to-weight ratio and can utilise the advantage of different materials. Short fibre-reinforced geopolymer (FRG) composite, as a new sustainable material, was developed as the skin layer of the sandwich panel. In addition, a proper PUR foam was chosen as the core of the sandwich panel. In this study, experimental study, theoretical analysis, and numerical simulation were conducted to reveal the failure mechanisms of the developed sandwich structures, the structural performance of the panel subjected to static loadings, and the vibration characteristics, as well as the vibration serviceability of the developed sandwich panels used as floor panels subjected to walking loads. The specific research work and objectives of this study included:

1) Developing sustainable FRG as the skin of the sandwich panel and investigating the mechanical properties and vibration characteristics of the FRG by experimental study.
2) Developing sandwich structures using FRG as the skin layer and PUR foam as the core layer and investigating the failure mechanism of the panel under flexural loading and edgewise compressive loading.
3) Investigating the structural performance of the full-size sandwich panels for prefabricated buildings under flexural loading and axial compressive loading.
4) Investigating the vibration characteristics of the developed sandwich panels by forced hammer impact vibration tests and developing and calibrating the finite element model to simulate the vibration properties of the developed sandwich panel.

5) Investigating the vibration performance of the floor system with the developed sandwich panel for the prefabricated buildings under pedestrian loads by finite element analysis.

1.3 Organisation of this dissertation

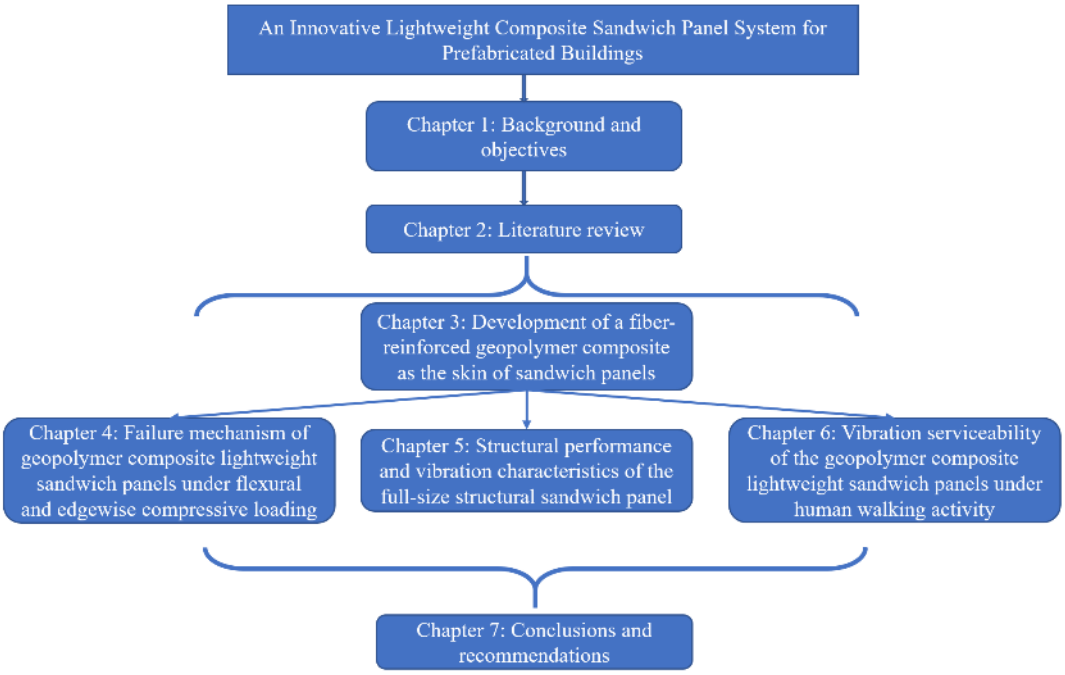

Figure 1.5 Flowchart of the thesis

This thesis comprises seven chapters. The roadmap of the research and the connectivity between chapters are shown in Figure 1.5. The contents of these seven chapters are described below:

Chapter 1: A brief introduction to the research is provided. The background knowledge is introduced in detail in this chapter and the objectives of the study are presented.

Chapter 2: A comprehensive literature review is provided in three parts. The first part describes the ongoing development of lightweight panels used in prefabricated buildings. The second part reviews the development of sustainable materials for civil engineering, especially geopolymer-based materials. In the last part, the vibration serviceability assessment methods and criteria for the buildings are presented. Then, the motivation and significance of the present study are presented.

Chapter 3: This chapter develops a new type of FRG composite. This chapter investigates the mechanical properties and vibration characteristics of the geopolymer matrix and FRG composite using methylcellulose as the organic admixture. A fly ash and slag-based geopolymer matrix incorporated with methylcellulose is developed and then reinforced by hybrid short fibres.

Chapter 4: A new type of lightweight sandwich panel with FRG composite skin layers and PUR foam core is developed for prefabricated buildings in this chapter. The failure mechanism of the developed sandwich panel under the bending moment and edgewise compression test is studied using the digital image correlation (DIC) method, which obtains the deformation information and failure mode of sandwich structures under different loading conditions. The shear failure of the core and tensile failure of the skin layers of the developed sandwich beam under flexural loading are observed under quasi-static three-point bending. Furthermore, the failure mechanism of the developed sandwich panel with different thickness-to-length ratios under edgewise compression loading is studied. Additionally, the analytical solutions for predicting the critical failure load under bending moment and edgewise compressive loading are proposed.

Chapter 5: In this chapter, the structural performance and the vibration characteristics of the developed full-size sandwich panels are studied. Two types of full-size sandwich panels are considered to study the performance under flexural loading. The first one (S1) is the full-size sandwich panel applying FRG as the skin and PUR foam as the core, same as that in Chapter 4. The second type (S2) originated from S1 is strengthened by basalt fibre-reinforced polymer (BFRP) sheet on the back FRG skin layer. Structural behaviours of the developed sandwich panels (full-size) are studied under quasi-static four-point bending and axial compression loads. The forced hammer impact vibration tests are applied to study the natural frequencies, modal shapes, and modal damping of the sandwich panel. Finite element modal analysis is performed to model the vibration characteristics of the developed sandwich panel.

Chapter 6: This chapter investigates the vibration serviceability of the floor system for the prefabricated buildings with the developed sandwich panels under pedestrian loads. The continuous walking load model are studied. Three different damping levels of the composite floor are considered for the evaluation of vibration serviceability. The root mean square (RMS) acceleration and vibration dose values (VDVs) are adopted as the vibration serviceability assessment parameters. Then, the influence of the composite floor length on the vibration serviceability is studied by finite element analysis under continuous human walking load.

Chapter 7: The conclusions and discussions of this research are given. Suggestions on future work based on this study are also provided.

2 Literature review

This chapter provides a comprehensive literature review regarding the current development of lightweight panels for prefabricated buildings. The first part of the literature review describes the ongoing development of lightweight panels used for prefabricated buildings. The second part reviews the development of sustainable materials for civil engineering, especially the geopolymer-based composite. In the last part, the vibration serviceability assessment method of buildings based on human perceptions is presented. Then, the motivation for and significance of this research are presented.

2.1 Development of lightweight panels for prefabricated buildings

Prefabrication is a manufacturing process, generally conducted at a specialised facility, in which various materials are joined to form a part of the final installation (19). Prefabrication represents the first stage of industrialisation of the building system and the remainder of the stages are mechanisation, automation, robotics, and reproduction (20). Prefabrication, as advanced construction technology, has several advantages to the traditional construction method (21). First, prefabrication can have a frozen design for the initial design for better adoption of prefabrication and better supervision for improving the quality of prefabricated products. Second, prefabricated construction can reduce the overall construction costs and shorten the construction time. Besides, the environmental performance can be improved for prefabricated construction regarding waste minimisation. Finally, prefabrication can achieve better integrity of the building design and construction with architectural beauty.

There are two main categories of prefabricated building construction methods: on-site prefabricated and off-site prefabricated construction methods (22). The on-site prefabrication method involves casting the construction members or components, such as floor slabs and columns, on-site and then delivering and assembling all components on-site. In the off-site prefabricated construction method, some or all of the building components are fabricated in the factory or prepared away from its final position and are then assembled after delivery. Depending on the different degree of prefabrication, which refers to the size and complexity of the prefabricated components or the configuration of the final product, prefabrication can be categorised into panelised buildings and modular buildings (1). Some examples (2) of prefabricated buildings are shown in Figure 1.4. The development of prefabrication and industrialisation of construction is promoting the development of innovative construction materials and technology.

With the demand for the prefabrication of buildings, researchers are also seeking new types of composite sandwich panels to be used for rapid construction, which are more lightweight, safer, more durable, and cheaper. In recent years, the sandwich panel has earned its reputation as an effective solution for building construction owing to its high strength-to-weight ratio and adequate levels of acoustic and thermal insulation. Therefore, sandwich panels have recently been applied in the field of civil infrastructures and building structures (23). The typically applied sandwich structure consists of thin skin layers to provide flexural strength and stiffness and a relatively flexible core layer to provide shear strength and stiffness. The skin layers and the core layer are usually bonded with an adhesive. Typical skin layers adapt materials, such as steel or aluminium, FRP systems, and cement-based composite. The core layer typically adopts polymeric foams, mineral wool, and balsa wood. Extensive studies have been performed to develop new generation solutions for these structural elements.

Shams et al. (24) developed innovative sandwich panels with two types of skins used for the sandwich panel: fabric textile-reinforced concrete and ultrahigh-performance fibre-reinforced concrete. PUR foams with varying types of shear connectors are used as the core and the shear connector used is a Syspro pin made of glass fiber reinforced polymer (GFRP) and shear grids made of carbon fiber reinforced polymer (CFRP). The design details of the panels are shown in Figure 2.1. The bending loading capacity under eccentric axial loading conditions can reach up to 2.1 MN/m because of the thick section of the sandwich panel. Shams (25, 26) also studied the performance of a designed sandwich panel under different thicknesses for the skins and fabric textile-reinforced concrete and different types of foam core, such as XPS, EPS, and PUR foam.

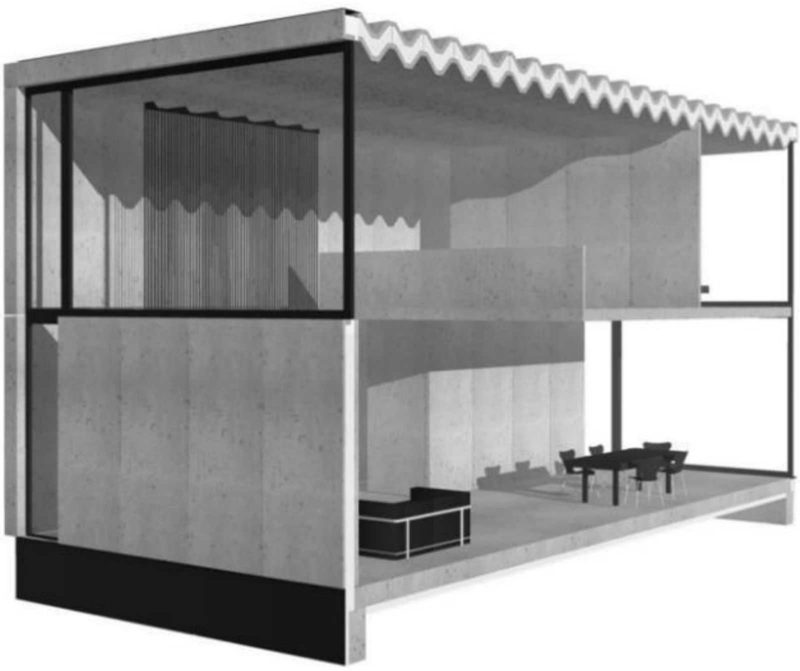

(a)

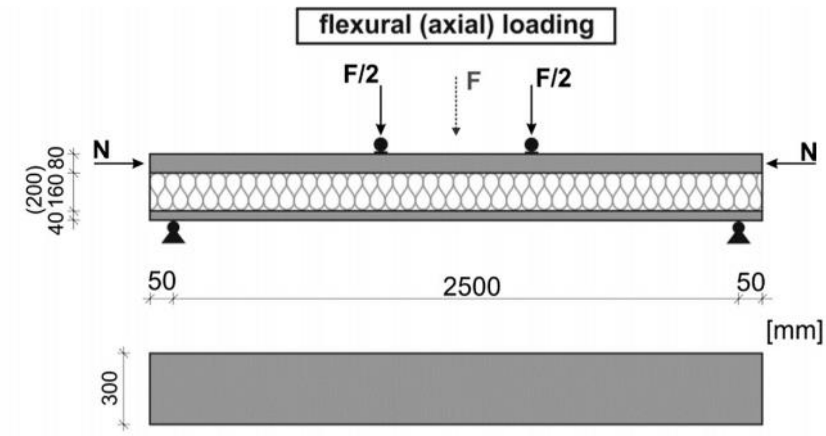

(b)

Figure 2.1 Application of sandwich structure developed by Shams (24): (a) Example of wall and roof element; (b) Flexural test setup

Mohammed et al. (27) investigated the structural behaviour of a new type of composite structural insulation panel for load-bearing wall applications. The skin of the sandwich panel was glass fibre-reinforced polypropylene with a thickness of 3 mm and the core was EPS foam with a thickness of 140 mm. The behaviour of the sandwich panel under compression along the vertical direction was studied. The failure mode under this situation was the debonding of the skin and core, with a failure load of 28

KN. Abdolpour et al. (28) used GFRP as the skin and EPS as the core to develop a sandwich panel used for modular houses (Figure 2.2). The flexural test results showed that the failure mode was the shear failure of the core. The FRP composite skin sandwich panel was found to hardly be used on the construction market because of the high cost of the FRP material and strict regulations towards the fire and high-temperature resistance of resident buildings worldwide.

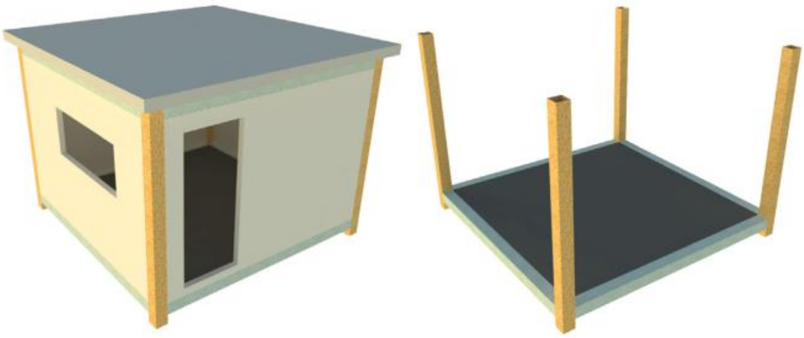

(a)

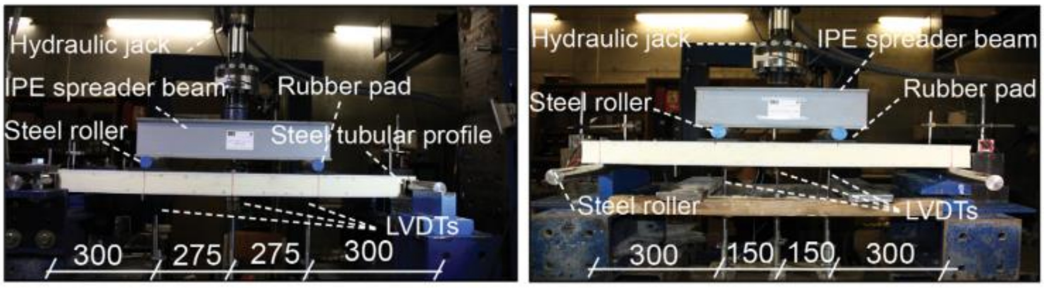

(b)

Figure 2.2 Applications of GFRP sandwich panel (28): (a) Designed building unit; (b) Experimental study

Mastali et al. (23) developed a composite sandwich panel with a GFRP laminate on the bottom tension skin, a deflection hardening cement composite on the top compression skin and a PUR foam as the core (Figure 2.3). The experimental results for the flexural test showed that the composite sandwich slab accomplished all the design requirements for serviceability and ultimate limit states.

Smakosz et al. (29) studied the strength, deformability, and failure mode of a new composite sandwich panel consisting of a magnesia cement board as the skin layers and EPS foam as the core (Figure 2.4). The experimental study showed that the designed composite sandwich panel overcame several deficiencies of the traditional structural insulated panels.

Salvador et al. (30) studied the flexural performance of two-span simply supported composite sandwich panels with wood-based composite as the skin layers and XPS foam as the core layer (Figure 2.5). Analytical models and a simple method to estimate the load were proposed based on the experimental results.

Portal et al. (31) developed a novel sandwich panel consisting of carbon-reinforced textile-reinforced concrete as the skin and a low-density foamed concrete as the core (Figure 2.6). The bending behaviour was studied by a four-point bending test and a nonlinear finite element analysis was developed to further study the bending behaviour of the composite sandwich panel.

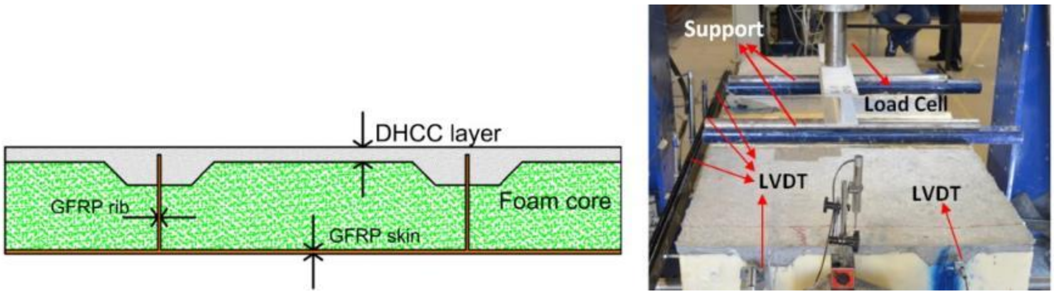

Figure 2.3 GFRP as the bottom skin layer, deflection hardening cement composite as the top skin layer, and a PUR foam core sandwich panel (23)

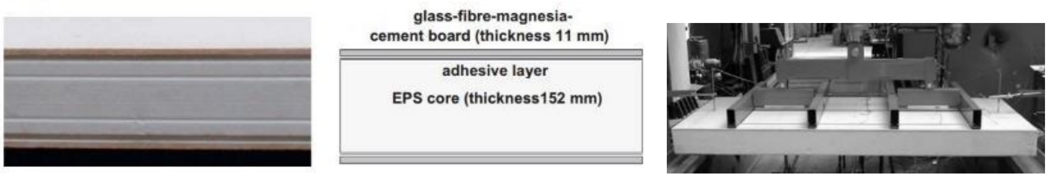

Figure 2.4 Magnesia cement board skin and EPS foam core sandwich panel (29)

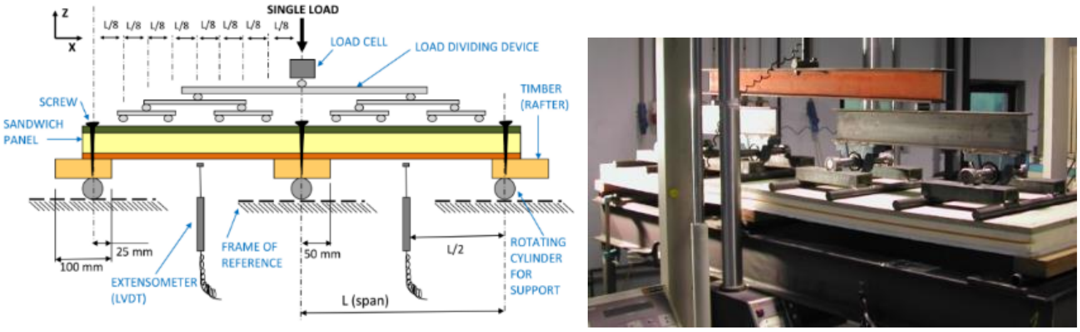

Figure 2.5 Wood-based composite skin and XPS foam core sandwich panel (30)

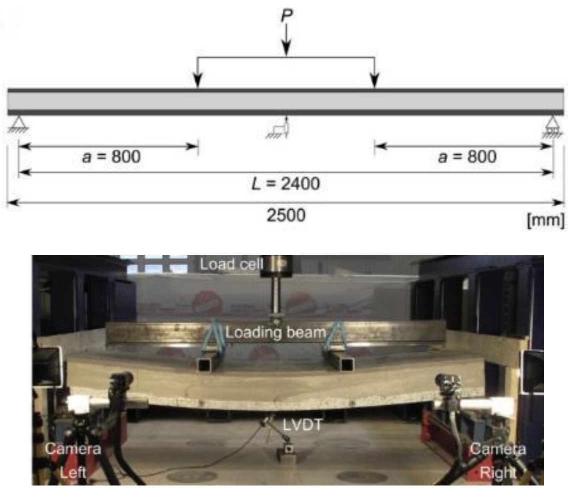

Figure 2.6 Textile-reinforced concrete skin and foam concrete core sandwich panel (31)

In summary, considering the types of panels reviewed above and the demand for prefabrication building techniques, the sandwich panel with a strong skin and functional core is very important for meeting both the structural and sustainable requirements. As cement-based materials are still widely used for constructions in civil engineering, a thin cement-based shell reinforced by fabric textile or FRP material other than conventionally used steel reinforcement is suitable to serve as the skin of the composite sandwich panel. Fly ash-based geopolymer material shares very similar properties with cement-based materials and it is more environmentally friendly and has a higher resistance to high temperatures than cement-based materials. Therefore, developing a geopolymer-based composite lightweight sandwich panel is important as an efficient material for prefabricated buildings.

2.2 Sustainability considerations in civil engineering

Eco-design and energy efficiency are concepts that require new building solutions to be environmentally friendly and lead to a reduction of materials and energy consumption (3). Cement production is one of the most significant contributors to environmental problems such as global warming. When manufacturing one tonne of OPC, approximately 0.8 tonnes of CO_2 are emitted into the atmosphere (16). OPC production contributes approximately 5%–7% of global CO_2 emissions and is a highly energy-intensive process (17). Therefore, developing alternative materials to relieve the massive demand for OPC production for the construction industry is important and has significant economic and environmental benefits. 'Geopolymer' use as a binder is promising in the construction industry and is an excellent alternative to OPC (32). Geopolymer composite does not use Portland cement as a binder. Instead, material such as fly ash, which is rich in silicon and aluminium is reacted with alkaline liquids to produce the binder (33). Usually, geopolymer material originates from geological origins, such as metakaolin and clay, or are an industrial by-product, such as fly ash and slag. Low calcium fly ash is an important part of the geopolymer that is available in Australia (34). Thus, geopolymer material is promising and feasibly practical as an alternative to OPC in Australia.

Previous studies have shown that geopolymer material has many advantages, such as excellent fire resistance (35), acid resistance (36), and high compressive strength (37, 38). However, geopolymer materials, while mechanically are similar to cementitious materials, have relatively low flexural and tensile strengths. For cement-based materials, short fibres are added to develop new fibre-reinforced cementitious (FRC) composites to improve the strength, ductility, and toughness (39-41). Short fibres have also been successfully applied to geopolymers to develop the FRG composite (32, 42-44), although only limited results have been reported to date. Steel fibres are effective for increasing the tensile strength of geopolymer composites (32).

Yu, et al (45) used fly ash, ground granulated blast-furnace slag, and limestone powder to replace cement to produce ultrahigh performance cement composite without any fibre. The compressive strength was up to 120 MPa and the flexural strength was up to 25 MPa. Nano silica was used to improve the mechanical performance in this study. Aydin (46) investigated the influence of different lengths and volume fractions of steel fibres on alkali-activated slag/silica fume mortars. With the help of high-temperature steam curing for 12 h, the compressive strength was up to 200 MPa and the highest flexural strength was 48.4 MPa. Ranjbar and Mehrali (43) investigated the effects of micro steel fibres that were coated with copper on the mechanical properties of a fly ash-based geopolymer. The sample was cured in a 65 °C oven for 24 h and then kept under ambient conditions with average temperature and humidity of 32 °C and 65%, respectively. The maximum peak flexural strength was by incorporation of the 3% micro steel fiber to the matrix that was approximately 33 MPa.

Lin and Jia (47) used the vacuum-bag technique together with high-temperature curing to make carbon fibre-reinforced metakaolin-based geopolymers. The lengths of the carbon fibres used were 2, 7, and 12 mm, and the ultrasonic vibration technique was used to help mix the fibres and geopolymer mortars. The flexural strength achieved by this technique was up to 91.3 MPa at a low volume fraction of carbon fibres (3.5%). Furthermore, Jia (44) investigated the influence of the volume fraction of carbon fibres on the flexural strength of a metakaolin-based geopolymer using the ultrasonic vibration mixing technique and found that the flexural strength was as high as 51.5 MPa, with a relatively high volume fraction of 5%.

The results from these previous studies have shown that FRG materials have the potential to achieve ultrahigh-performance. However, the choice of geopolymer matrix and its mixing design, the choice of fibres, and the interface bonding between the matrix and fibres should be studied and designed carefully.

First, as mentioned above, the main categories of geopolymers used to substitute OPC are metakaolin clay, fly ash, and slag. The limitations of metakaolin clay compared to fly ash and slag include it requiring high-temperature processing to be produced from kaolinite, which consumes more energy than fly ash and slag production. Furthermore, the plate-shaped particles increase the water demand of the system and the complexity of processing, which prohibits its mass use in geopolymer matrices (48). Fly ash is more advantageous owing to its high reactivity from its finer particle size compared to slag(32). Therefore, from the perspective of environmental greenness and the possibility of production, fly ash and slag are very competitive as geopolymer matrices.

Second, fibres are incorporated to enhance the flexural and tensile strength of geopolymer material and to change the brittle failure of this material to a ductile mode. The fibres for reinforcing cementitious materials include steel fibres, polyvinyl alcohol (PVA) fibres, basalt fibres, carbon fibres, and glass fibres. The properties of these fibres are listed in Table 2.1 based on the summarisation of Banthia (49).

Table 2.1 Properties of fibres used for reinforcing geopolymer concrete

Fibre type	Tensile strength, MPa	Tensile modulus, GPa	Tensile strain, % max to min	Fibre diameter, μm	Relative adhesion to matrix	Relative alkali stability
Steel	1000	200	2 to 1	50 to 85	Excellent	Excellent
Polyvinyl alcohol	800 to 1500	29 to 40	10 to 6	14 to 600	Excellent	Good
Basalt	600 to 3600	69 to 150	0.3 to 0.1	0.02 to 30	Excellent	Excellent
Carbon	590 to 4800	28 to 520	2 to 1	7 to 18	Poor to good	Excellent
Alkali-resistant glass	1700	72	2	12 to 20	Excellent	Good

All the fibres listed in Table 2.1 have been used in previous studies to reinforce geopolymer concrete. Some natural fibres have also been used to reinforce fly ash-based geopolymer concrete; however, the mechanical properties are not as idealised since the weaker strength of these natural fibres (50, 51).

Shaikh (52) studied steel fibre, PVA fibre, and a hybrid form of steel and PVA fibres for the reinforcement of fly ash-based geopolymer concrete. This author found that the bond of PVA fibres with a geopolymer matrix was higher than that with a cement matrix; however, an opposite trend was observed for steel fibres. The peak flexural strength could be up to 19 MPa and steel fibre-reinforced material had relatively higher strength than that of the PVA fibres. Nematollahi (53) also used PVA fibres to reinforce fly ash-based geopolymer and the splitting tensile strength was 4.7 MPa. Unlike the research on fibre concrete, relatively little research on FRG materials has been published.

Steel fibre is very attractive for developing FRG composite because of its high strength and good bonding behaviour. However, the deflection capability corresponding to the peak load of steel FRG is quite poor (43, 44), leading to lower ductility and toughness. Studies have been conducted to demonstrate that synthetic fibres, such as PVA, polyethylene, and polypropylene fibres, exhibit better post-crack strain hardening behaviour compared to steel fibres; however, they do not have adequate stiffness for improving the first-crack control capability or the ultimate load (32). FRG reinforced with short steel fibres (1%) and PVA fibres (1%) has been shown to have better energy absorption capability compared to a geopolymer matrix reinforced with mono fibres (32).

In recent studies, organic admixtures have been added to the cementitious and geopolymer composites to improve their mechanical properties (54-56). It has been shown that geopolymer mortars containing organic mixtures offer enhanced compressive strength and toughness with fewer micro-cracks (57, 58). Therefore, adding an organic substance to cementitious and geopolymer composites might be an effective way of improving the overall mechanical properties. However, it becomes difficult to disperse microfibres, such as synthetic fibres and carbon fibres, into cement- or geopolymer-based materials when increasing the mass content because they tend to cluster when mixing (59). Previous studies have demonstrated that organic ingredients, such as methylcellulose, improved the dispersion of short synthetic and carbon fibres into the cementitious matrix to achieve a more uniform distribution (60) and enhanced the bonding strength between these fibres and the cementitious matrix (61). However, studies on applying methylcellulose to improve the mechanical properties of geopolymer composites are very limited. To the best of our knowledge, no literature has reported studying the effect of adding methylcellulose on the mechanical properties and vibration characteristics of the FRG composite.

Another concern for sustainability and eco-design in civil engineering is the energy consumption of buildings. The United Nations Environmental Program (4) estimates that buildings consume approximately 40% of the global world energy, 25% of the global water, and 40% of the global resources. Buildings are also responsible for approximately 1/3 of greenhouse gas emissions of the entire planet. So, enhancing the insulation properties of building envelopes is one of the most effective strategies to reduce the energy consumption caused by heating and cooling demand of buildings (11). To achieve better insulation properties of building envelopes, thermal insulation materials with low thermal conductivity have been developed and widely used for building industries.

In summary, the application of sustainable materials and materials that can improve the energy efficiency by developing lightweight composite panels for prefabricated buildings are promising and feasible concerning eco-design and sustainability considerations.

2.3 Vibration serviceability assessment of buildings

In recent years, innovative lightweight materials and structures have been applied for the construction of prefabricated buildings, such as the wall, roof and floor panels of the modular buildings. Engineers and building owners have begun to pay special attention to the vibration serviceability of buildings as the occurrence of excessive vibrations has become more common, especial for prefabricated buildings with lightweight materials and composite structures. The response of humans to vibrations generated in buildings depends on two main factors: direct effects and indirect effects (62). Direct effects include the frequencies, magnitude, duration, and direction of the vibrations, as well as the intervals between vibration events or exposure of the humans to the vibrations. The indirect effects on the subjective response to vibrations include audible noise and infrasound, visual cues, population type, familiarity with vibrations, structural appearance, confidence in the building structure, height above the ground, warning of events, activities engaged in, and knowledge of the source of the vibrations (62). Human perception of vibrations is very sensitive, and excessive exposure to annoying vibrations causes discomfort and possible health problems for occupants. The sources causing the vibrations of buildings can be classified into two categories: external sources and internal sources (62). External sources refer to building excitations caused by ground vibrations due to passing traffic, wind excitations, or airborne acoustic excitations. Internal sources can generally be separated into two categories: mechanical excitation and human-induced excitation. Examples of mechanical vibrations include lifts, air-conditioning or ventilation plant, and heavier office machinery in commercial premises, and appliances such as vacuum cleaners and washing machines in household premises. Human-induced excitation is generally created by dynamic human activity, such as walking, running, jumping, and dancing.

Human-induced excitation is the most common and important internal source of dynamic excitation.

The vibration serviceability design and assessment have drawn much attention by researchers and engineers. ‘Rating method’ and ‘weighting method’ are the two main categories of methods adopted by standards for vibration evaluation and assessment. The rating method was adopted by the earlier standards. For this method, the measured time history series of vibration signals must be transferred to the frequency domain to obtain the frequency spectrum. Then, the largest components from the frequency spectrum are compared with the acceptable limit, which is defined as a baseline multiplied by factors representing different occupancy types, exposure periods, and types of vibrations. However, the rating method might underestimate the vibration effects when the vibration frequency range is broad (62). Therefore, many new standards now adopt the weighting method, which weights the measured time records using a frequency weighting function. The frequency weighting function is defined based on the vibration direction and expected effect on the subject, which is the reciprocal of the equivalent perception/comfort curves. Then, the peak acceleration, RMS, or VDV is compared with the accepted limit suggested by the standards. This method has been widely used by current standards, as it has the advantage of being effective for dealing with complex signals that have broad frequency content and results in a single value incorporating the frequency, magnitude, and direction effects to compare with the acceptable limits.

Standards published by ISO are one category of the most widely used standards for vibration serviceability assessment. The standards include ISO 2631-1 (63), ISO 2631-2 (64), and ISO 10137 (65). ISO 2631-1 contains the general requirements for the evaluation of human exposure to whole-body vibrations. ISO 2631-2 includes the evaluation of human exposure to vibrations in buildings from 1 to 80 Hz range. ISO 10137 contains bases for the serviceability design of building structures and walkways subjected to vibrations. The American National Standard Institute has adopted the provisions of the ISO standards for use in the United States.

The other widely used standards related to vibration evaluation and assessment are the standards published by the British Standards Institution. These standards include BS 6841(66) and BS 6472-1 (67). BS 6841 provides general requirements for the measurement and evaluation of human exposure to whole-body mechanical vibration and repeated shocks, and BS 6472-1 guides the evaluation of human exposure to building vibrations for vibration frequency in the range of 1 to 80 Hz, except for vibrations under blast loading.

All these standards adopt the weighting method rather than the rating method for vibration evaluation and assessment. However, the frequency weighting functions applied by different standards are different. For example, the variation of the frequency weighting functions for a frequency range from 0 Hz to 20 Hz is shown in Figure 2.7. The variation of the frequency weighting function is adapted by many standards: W_b and W_d are applied by BS 6472-1, W_g and W_d are used by ISO 10137, W_k and W_d are based on ISO 2631-1, and W_m is based on ISO 2631-2, which uses the thin frequency range from 0 to 20 Hz. W_d is the frequency weighting function for the horizontal direction, and W_g, W_k, and W_b are the frequency weighting functions for the vertical direction. The W_g weighting function is defined in BS 6841 and has been widely adopted as the basis for the base curve for the evaluation of vibration in the vertical direction by many standards, such as ISO 2631-2, BS 6472, and ISO 10137. Therefore, W_g was applied as the frequency weighting function in the present study.

Various parameters are involved in the evaluation and assessment of building vibrations related to human perception and comfort adapted by different guidelines. The choice of peak or RMS acceleration for the vibration evaluation and assessment is the main priority. Some design guides, for example, the AISC Design Guide 11, which is the National Building Code of Canada, adapt the peak value. However, these design guides are used for a specific method of computing the anticipated vibrations rather than for the general evaluation criteria (62). The peak acceleration is a good indicator of the vibration perception threshold and is adapted by ISO 2631-1 and BS 6841. However, the calculation of the RMS value of acceleration has been mostly used for the evaluation of vibration serviceability based on the discomfort and annoyance to humans. The main issue for the RMS value of acceleration is that the selected duration has a significant effect on the calculated result. Therefore, different integration times have been proposed by many previous studies. Rasmussen (68) suggested that a 60 s period should be used to identify the lower bound and a 1s period should be used to estimate the upper bound of the RMS values. A 10 s maxima RMS and 1s RMS for vibration evaluation is applied by ISO 2631-1 and ISO 10137.

However, the RMS value of acceleration for 1 s integration still appears too short and it might be seen as the threshold for the vibration perception rather than the evaluation for the vibration annoyance.

The current version of standards published by the ISO and the British Standards Institution, ISO 10137 and BS 6472-1, adopt the use of the VDV limit as the parameter for vibration evaluation and assessment rather than peak acceleration or RMS acceleration. The reason that VDV has been adopted is that it can include the effect of vibration duration for the evaluation of vibrations and the assessment of buildings. Therefore, it is more logical to apply the VDV as the vibration criterion because the building vibration becomes more unacceptable the longer it lasts. Other evaluation parameters, i.e. peak and RMS accelerations, cannot consider the effect of vibration duration. The RMS acceleration depends on the vibration duration, but it does not necessarily increase with the vibration duration, thus it cannot consider the accumulation effect of the duration of building vibration. The equation applied to calculate RMS acceleration is:

$$a_{rms} = \sqrt{\frac{1}{T}\int_0^T a(t)^2 dt} \tag{2.1}$$

where, T is the duration of the considered events and *a(t)* is the acceleration signal from either testing results or finite element simulation method .

The equation used to calculate VDV is given below:

$$VDV = \left[\int_0^T a_w^4(t)dt\right]^{1/4} \tag{2.2}$$

where, T is the duration during which a person is exposed to the vibration and $a_w(t)$ is the frequency weighted acceleration. As mentioned above, VDV accumulates the vibration effects rather than averaging them and increases with duration. It is sensitive to the peak vibrations (69). The present study adopted both the weighting method over the vibration evaluation technique and RMS acceleration as an evaluation parameter according to BS 6472-1.

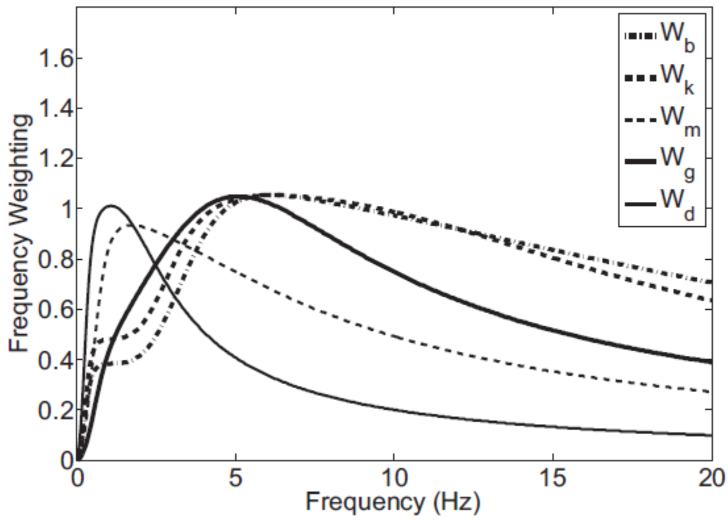

Figure 2.7 Variation of the frequency weighting function versus frequency (70)

Many previous studies have been undertaken regarding the establishment of international standards in terms of the vibration acceptance criteria and threshold, including the BS 6472, ISO 2631, and ISO 10137. These standards cover many different environments including buildings. The acceptance criteria are related to the frequency weighted ‘baseline curves’ based on the perception of human beings and other factors. The base curves of the vibration in the z-axis and x/y axis in these standards are shown in Figure 2.8. The base vibration acceptance threshold for the z-axis is 0.005 m/s^2 and the base threshold for the x/y axis is 0.003 m/s^2. The base curves for the z-axis and x/y axis are obtained based on the base vibration acceptance threshold and the frequency weighted functions W_d and W_g. The lines in Figure 2.8 represent a constant level of human perception as an isopercepability line. The areas above the base curves correspond to human perception regarding an increasing level of vibration; the areas below the base curves represent the vibration level that humans cannot perceive. However, in practice, the base curves are rarely applied because they only represent a single value of vibration acceptance threshold corresponding to a single frequency. Instead, the calculated or tested acceleration is attenuated by the frequency weighting using factors that are appropriate to the frequency of the mode considered.

Continuous vibration is one representative of the worst possible loading scenario for human perception under a given forcing function. Therefore, most standards apply a conservative assessment scenario. BS 6472 and ISO 10137 provide multiplying factors to the base curves for continuous vibrations, which correspond to a low probability of adverse comment. The multiplying factors are shown in Table 2.2. In practice, the multiplying factors in Table 2.2 are used as limits to the value of the calculated response factors. The response factor is defined as the frequency weighted RMS acceleration divided by the appropriate base value.

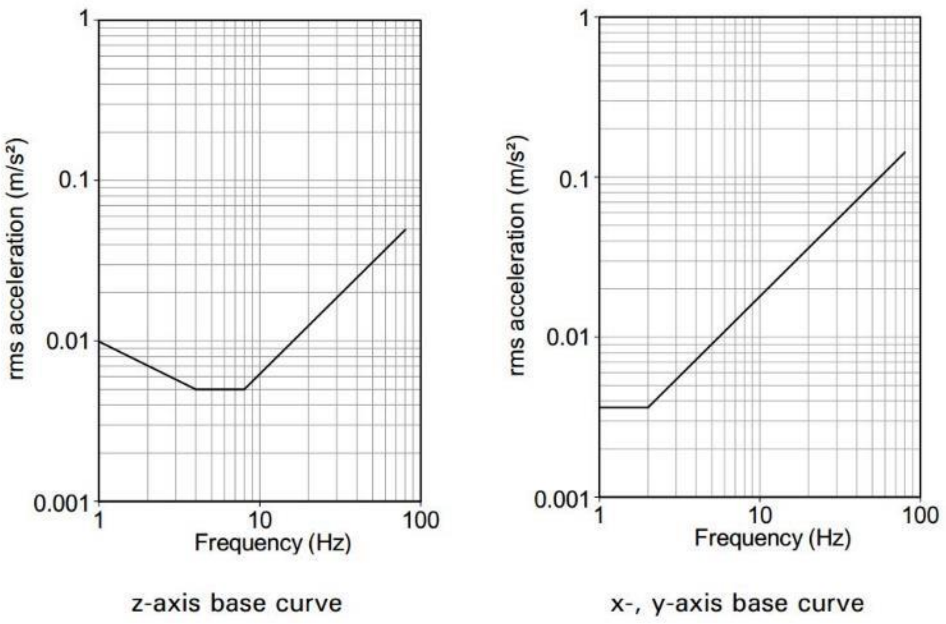

Figure 2.8 Base curves for the perception of vibration for humans in different directions (67)

Table 2.2 Multiplying factors specified for 'low probability of adverse comment'

Place	Time	Multiplying factor for exposure to continuous vibration 16 h day/8 h night	Impulsive vibration excitation with up to 3 occurrences
Critical working areas (e.g. hospital operating theatres)	Day	1	1
	Night	1	1
Residential	Day	2 to 4	60 to 90
	Night	2	20
Office	Day	4	128
	Night	4	128
Workshops	Day	8	128
	Night	8	128

To assess the excessive vibration of floor response for intermittent activities, VDV is also reliable and applied by ISO 10137 and BS 6472. The tolerance level according to BS 6472 is shown in Table 2.3. As shown in Table 2.3, the VDV threshold is the total VDVs accumulated duration of the happened activities. For example, when the VDV equals 0.4, it means that the building is possible to cause the uncomfortable feelings of occupants because of the accumulation of the happening event on the building floor through 16 hours in the daytime. As discussed above, the VDV for each event can be calculated by Eq. (2.2), and therefore the total vibration dose value (VDV_t) can be calculated by the following equation:

$$VDV_t = \left(\sum_{i=1}^{n} VDV_i^4\right)^{1/4} \tag{2.3}$$

where VDV_i is the vibration dose value for each event happening on the building floor. If the event is the repeat of single activity, such as human walking, the Eq. (2.3) can be expressed as:

$$\begin{cases} VDV_t = (n_a \cdot VDV^4)^{1/4} \\ n_a = \left(\frac{VDV_t}{VDV}\right)^4 \end{cases} \tag{2.4}$$

where n_a is the number of event occurrences. Ellis (71) suggested a method for calculating VDVs for the vibration serviceability assessment during the design stage, which is shown below:

$$VDV = 0.68 \cdot a_{rms} \sqrt[4]{n_a T_a} \tag{2.5}$$

where T_a is the period for the considered single activity on the floor. Thus, n_a can be estimated by back calculation with the value of a_{rms}:

$$n_a = \frac{1}{T_a}\left(\frac{VDV_t}{0.68 a_{rms}}\right)^4 \tag{2.6}$$

The value of n_a is also dependent on the activities occurring on the floor. When the VDV is the threshold value, n_a can be calculated. If n_a is unlikely to occur in real life, the vibration of the target floor is within the range of comfort.

Table 2.3 Tolerance level of VDV according to BS 6472 (Unit: $m/s^{1.75}$)

Place	Low probability of adverse comment	Adverse comment possible
Building 16 h day	0.2 – 0.4	0.4 – 0.8
Building 8 h night	0.13	0.26

2.4 Summary and implications

According to this literature review, the development of lightweight sandwich panels has drawn greater attention because of the increase in the use of the prefabricated building method. Additionally, eco-design and energy efficiency has become more important for the building sector and they drive the demand for innovative material and structures. Currently, most of the lightweight panels that have been developed use applied wood-based, cement-based, or FRP composite-based material. However, wood-based material is vulnerable to flood and termite damage and cement-based material is not sustainable. The cost of FRP materials makes them difficult to be massively used in civil engineering. Therefore, the present study developed an innovative lightweight panel system to use in prefabricated buildings considering sustainability and energy efficiency factors. It is made of industrial waste and good insulation materials, hence leads to low energy consumption in construction applications. The developed lightweight panels adapted the concept of the sandwich structure, which applied FRG as the skin layer and PUR foam as the core layer. The failure mechanism and structural behaviour of the developed sandwich panel were studied in the present study. Excessive vibrations in buildings have drawn greater attention in recent years regarding the human perception of comfort, especially for lightweight structures. Therefore, the vibration serviceability of developed lightweight sandwich panels was also studied in the present study.

3 Development of a fibre-reinforced geopolymer composite as the skin of sandwich panels

3.1 Introduction

This chapter investigates the mechanical properties and vibration characteristics of geopolymer paste (GP) and FRG with added methylcellulose. Fly ash and slag are applied to manufacture the GP and FRG. Short fibres including 1% copper coated steel (CS) and 1% high strength polyethylene (HSPE) fibres in volume fraction are used to develop the FRG. Different contents of methylcellulose as the organic binder are added separately to the GP and FRG. The mechanical properties, including compressive strength, flexural strength, ductility, and toughness, are compared to investigate the effect of adding methylcellulose to the GP and FRG. Furthermore, the vibration characteristics of the nylon thread hung GP and FRG beam with the dimensions of 20 × 75 × 300 mm (height × width × length) are studied using the force hammer impact vibration test. The fundamental frequencies and damping ratios of the tested beams are identified. The main objective of the impact vibration tests is to investigate the influence of adding methylcellulose on the vibration characteristics of GP and FRG, especially the damping ratio and dynamic modulus of elasticity (DMOE).

3.2 Experimental studies

3.2.1 Materials and sample preparation of GP and FRG

In this study, fly ash and slag are the primary ingredients of the GP and the main geopolymer binders in the FRG. A combination of HSPE and CS fibres are used as reinforcement to make the FRG. Fly ash and slag are supplied by Gladstone and Choice of Builders, respectively. Based on the ASTM C618-12 (72), the fly ash is classified as class F. The chemical compositions of the fly ash and slag are given in Table 3.1. A 12 M sodium hydroxide solution and D-grade sodium silicate solution are used as the activator. The 12 M sodium hydroxide solution is prepared by mixing pure sodium hydroxide powder with tap water. The D-grade sodium silicate solution is commercially available and obtained from PQ Australia Ltd. Commercially available HSPE and CS fibres are used and the properties of these two short fibres are given in Table 3.2. The organic ingredients (MKX 6000 PF 01 hydroxyethyl methylcellulose) are supplied by DOW Chemical Pty. Ltd. The fly ash, slag, and methylcellulose are shown in Figure 3.1, and the CS and HSPE fibres are shown in Figure 3.2.

Table 3.1 Chemical compositions of the fly ash and slag

Content wt%	SiO_2	Al_2O_3	Fe_2O_3	CaO	MgO	MnO	K_2O	Na_2O	P_2O_5	TiO_2	SO_3
Fly ash	51.11	25.56	12.48	4.3	1.45	0.15	0.7	0.77	0.885	1.32	0.24
Slag	32.45	13.56	0.85	41.22	5.1	0.25	0.35	0.27	0.03	0.49	3.2

Table 3.2 Geometric and material properties of short fibres

Type of fibre	Length (mm)	Diameter (mm)	Modulus of elasticity (MPa)	Fibre strength (MPa)	Density (g/cm^3)
HSPE	12	0.012	123	3500	0.97
CS	13	0.2	200	2850	7.8

(a) (b) (c)

Figure 3.1 Solid ingredients: (a) Fly ash; (b) Slag; (c) Methylcellulose

(a) (b)

Figure 3.2 CS fibre (a) and HSPE fibre (b)

The GP and FRG were manufactured and cured under an ambient environment, as per the following manufacturing processes. For the GP, the sodium hydroxide and sodium silicate solutions were mixed and placed for 30 min at room temperature. Geopolymer ingredients including the fly ash, slag, and methylcellulose were placed into a Harbert mixer and mixed at a low speed for 3 min. Then, the alkaline solution as an activator was poured into the mixer and mixed with the other ingredients for another 3 min. Finally, the GP was poured into plywood moulds. The manufacturing process for the FRG was nearly identical to that for the GP. The only difference was that the CS and HSPE fibres were placed into the mixer and mixed for another 3 min after the ingredients for the GP were mixed in the mixer. Both the wet GP and FRG in the plywood moulds were placed on a vibration table and vibrated for 2 min. The GP and FRG samples were then covered with plastic sheets and placed in the curing room at ambient temperature for 24 h before demoulding. After demoulding, the GP and FRG samples were placed in the curing room for 28 days, which were then used for the subsequent tests. No apparent fibre cluster for FRG was observed during the mixing process and relatively uniform fibre distribution was achieved. However, adding methylcellulose to the FRG made the mixing easier and produced a proper distribution of fibres in a short time compared to the sample without any methylcellulose.

The different mix designs for the GP and FRG that are applied in this study are shown in Table 3.3. For each sample, the GP group represents the geopolymer paste with varying methylcellulose content. ‘GP0’ refers to the geopolymer matrix without fibres and methylcellulose, whereas ‘GP1’, ‘GP2’, and ‘GP3’ are modified samples based on GP0 by adding 0.4%, 0.8%, and 1.2% of methylcellulose, respectively. The FRG group represents the FRG composite with varying methylcellulose content. ‘FRG0’ refers to the geopolymer composite with 1% HSE and 1% CS fibres without methylcellulose, whereas ‘FRG1’, ‘FRG2’, and ‘FRG3’ are modified samples based on FRG0 by adding 0.4%, 0.8%, and 1.2% of methylcellulose, respectively. At least three samples are prepared for the compressive, flexural, and vibration tests for each case listed in Table 3.3. A total of 48 samples are made and tested in this study. The average density of the GP group is 2024 kg/m^3 and the average density of the FRG group is 2070 kg/m^3. The addition of methylcellulose does not affect the density of either the GP or FRG composites because the content of methylcellulose added is very small.

Table 3.3 Mix proportions of geopolymer composites

Group No.	Composite types	Mix proportions (by weight)					Fibre types (by volume)	
		Solid ingredients			Solution			
		Fly ash (g)	Slag (g)	Methylcellulose (%)	Na(OH) (12M) (g)	Na_2SiO_3 (g)	HSPE (%)	CS (%)
GP	GP0	0.6	0.4	-	0.14	0.36	-	-
	GP1	0.6	0.4	0.4	0.14	0.36	-	-
	GP2	0.6	0.4	0.8	0.14	0.36	-	-
	GP3	0.6	0.4	1.2	0.14	0.36	-	-
FRG	FRG0	0.6	0.4	-	0.14	0.36	1	1
	FRG1	0.6	0.4	0.4	0.14	0.36	1	1
	FRG2	0.6	0.4	0.8	0.14	0.36	1	1
	FRG3	0.6	0.4	1.2	0.14	0.36	1	1

3.2.2 Experimental setup and testing program

3.2.2.1 Study of the influence of methylcellulose on GP and FRG using the quasi-static test

The effect of using methylcellulose as an organic admixture on the mechanical properties of GP and FRG is studied by conducting a quasi-static test. The behaviour of GP and FRG under compressive and flexural loads is studied. The GP and FRG have the same test setup for the compression and flexural tests. The setup for the compression test is designed based on ASTM C109-13(73). The dimension of the samples for the compressive tests is 50 mm × 50 mm × 50 mm and the loading rate is set at 900 N/s. The applied load is recorded by the load cell and the corresponding deflection is recorded with a displacement transducer.

The behaviour of GP and FRG under the flexural load is studied by conducting the four-point bending test, which is designed according to the methodology described by a previous study (74). The dimensions of the prisms for the flexural test are 20 × 75 × 300 mm (height × width × length) based on the previous study. The four-point bending tests on all samples are performed using an Instron testing machine with a loading rate of 0.5 mm/min. The span of each sample is kept at 280 mm. During the four-point bending test, the applied load and the corresponding deflection at the mid-span were recorded. The experimental setup for the flexural test is shown in Figure 3.3. According to ASTM C1609 (75), the modulus of rupture (MOR) for each composite panel can be determined from the following equation:

$$f = \frac{P \cdot L}{b \cdot d^2} \tag{3.1}$$

where, f is the strength (MPa), P is the load (N), L is the span length (mm), b is the average width of the sample (mm), and d is the average depth of the sample (mm).

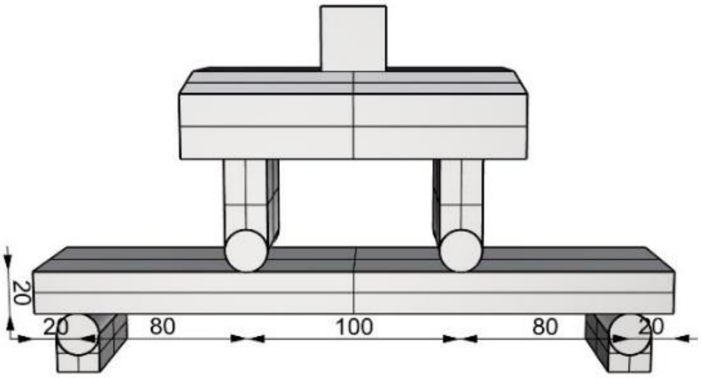

(a)

(b)

Figure 3.3 Experimental setup for flexural tests: (a) Schematic diagram (unit: mm); (b) Test setup

3.2.2.2 Study of the influence of methylcellulose on the vibration characteristics of GP and FRG

The influence of adding methylcellulose on the vibration characteristics of GP and FRG is studied with the force hammer impact vibration test. Vibration characteristics of the samples, including natural frequency and damping ratio, are obtained by analyzing the dynamic responses. The GP and FRG samples apply the same setup for the force hammer impact vibration test, which is designed based on the standard testing method for concrete structures as specified in ASTM C215 (76). The fundamental frequency is directly determined by signal analysis and, therefore, the dynamic modulus is calculated accordingly. However, this standard does not suggest a specific method for determining the damping ratio of the tested samples by the force vibration tests. The acceleration responses are recorded from the vibration tests and the damping ratio is obtained by various methods. Usually, the recorded dynamic responses from the vibration tests can be analysed either in the time domain or frequency domain to obtain the fundamental frequency and damping ratio of the tested samples. The logarithmic decrement method is one of the traditional ways of identifying the damping ratios. However, there are some difficulties and uncertainties with determining the peak value of the time history records and the number of cycles needed to calculate the damping ratio. Therefore, the exponential fitting-based method (77) is used to identify the damping ratio of the tested samples.

The GP and FRG prisms with dimensions of 20 ×75 ×300mm (height × width × length) are prepared for the hammer impact vibration tests. For these tests, all samples are hung by nylon threads to simulate free boundary conditions. An instrumented hammer is used to apply an excitation force at the mid-span of the samples. An accelerometer is attached on the opposite side to where the impact force is applied by the hammer. The mass of the installed accelerometer is assumed to have a negligible effect on the vibration of the tested specimens because it is very light compared to the tested samples. The detailed schematic test setup, including the boundary condition and installed sensor location, is shown in Figure 3.4. The National Instruments (NI9234) data acquisition system and commercial software Signal Express is used to record the acceleration responses from the vibration tests. High sensitivity accelerometers PCB 393B04 are employed in the tests and the sampling rate is set at 2000 Hz to record the time-domain vibration responses.

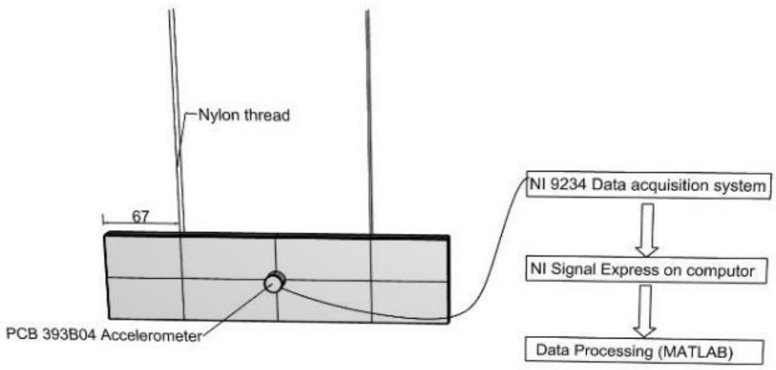

(a)

(b)

Figure 3.4 Test setup for hammer impact vibration test: (a) Schematic diagram; (b) Test setup

A signal processing technique, the fast Fourier transform (FFT) with a low-pass filter is used for the data analysis. Low-pass filtering is performed to remove the high-frequency noise and FFT is conducted to identify the natural frequency of the tested samples. In the present study, the fundamental vibration frequency and corresponding damping ratio are extracted. The natural frequency is dependent on the structural properties, i.e. dimensions, boundary conditions, and material properties. In the present study, all the GP and FRG samples are designed to have the same dimensions and are tested under the same boundary conditions. Therefore, comparing the natural frequencies indicated the stiffness of the structure and indirectly reflects the stiffness of the materials that are used. The first step is to use the Hilbert transform to obtain the envelope of the recorded time history of the acceleration. The second step is to apply exponential curves to fit the obtained envelope of the signals and identify the damping ratio of the tested samples.

The DMOE of the GP and FRG samples is determined by the obtained fundamental frequency from the force hammer impact vibration test. Previous studies have shown that DMOE is higher than the SMOE (78). Therefore, it is meaningful to study the influence of methylcellulose on the DMOE for GP and FRG to provide more accurate information to evaluate the vibration characteristics. DMOE is adopted to evaluate the influence of adding methylcellulose on the vibration performance of GP and FRG under dynamic loads in the present study. DMOE can be calculated based on the identified fundamental frequency according to ASTM C215 (76) using the equation below:

$$DMOE = C \cdot M^2 \tag{3.2}$$

where, M is the mass of the sample (kg), n is the fundamental frequency (Hz), and C equals $0.9464(L^3T/bt^3)$ ($N{\cdot}s^2(kg{\cdot}m^2)$) for the prismatic specimen, in which L is the length of specimen (m), t and b are the dimensions of the cross-section (m), and T is the correction factor that can be obtained from ASTM C215 (76).

For each mix design of GP and FRG, three samples are prepared. Five repeated hammer impact vibration tests are conducted on each sample and the corresponding time history responses are recorded. Therefore, a total of 15 measurements for each mix design are recorded and used to identify the vibration characteristics.

3.3 Results and discussions

3.3.1 Influence of methylcellulose on the static mechanical properties of GP and FRG

3.3.1.1 Influence of methylcellulose on the behaviour of GP and FRG under compressive load

The behaviour of GP and FRG under compressive load is studied using the quasi-static test. The typical damage modes of the GP and FRG samples under the compressive tests are shown in Figure 3.5. It is observed that the GP samples are damaged suddenly during the test; however, the FRG samples experience slow damage with the appearance of multiple cracks. This phenomenon indicates that the inclusion of HSPE and CS fibres effectively change the brittle failure mode to the ductile failure mode. However, GP1, GP2, and GP3 have the same brittle damage mode as that of GP0 and the damage modes of FRG1, FTG2, and FRG3 are similar to that of FRG0. Therefore, the addition of methylcellulose into GP and FRG has little influence on the damage modes of GP and FRG.

Another crucial feature of the GP and FRG samples under compressive load is the compressive strength. The compressive strengths of the GP and FRG samples are shown in Figure 3.6(a). The normalised strength ratios for GP and FRG are also calculated and are shown in Figure 3.6(b) to reflect the influence of methylcellulose on the compressive strength of GP and FRG. The legends of the *X*-axis are M0%, M0.4%, M0.8%, and M1.2% representing the added contents of methylcellulose are 0%, 0.4%, 0.8%, and 1.2% by weight, respectively. As shown in Figure 3.6(a), the compressive strengths of GP1, GP2, and GP3 are higher than that of GP0 and the same trend is found for FRG, with the compressive strength of FRG1, FRG2, and FRG3 being higher than that of FRG0. Furthermore, as shown in Figure 3.6(b), the maximum strength ratio of GP2 is 1.14, with a content of 0.8% methylcellulose. This indicates that adding 0.8% of methylcellulose into GP0 have a 14% improvement in the compressive strength. Similarly, the maximum strength ratio of FRG2 is 1.18, with a content of 0.8% methylcellulose. This indicates that adding 0.8% of methylcellulose into FRG0 has an 18% improvement in the compressive strength. The experimental results show that adding methylcellulose effectively increases the compressive strength of both GP and FRG.

Another trend that is found is that adding 0.8% of methylcellulose achieves the highest improvement in compressive strength for both GP and FRG but adding 0.4% and 1.2% of methylcellulose does not achieve the same increase of compressive strength. As shown in Figure 3.6(b), the strength ratio for GP2 is 1.14, which is higher than that of GP1 (1.03) and GP3 (1.06). In addition, the strength ratio for FRG2 is 1.18, which is higher than that of FRG1 (1.04) and FRG2 (1.07). This is consistent with the existing test results from a previous study (79) whereby adding 0.25% to 1% of methylcellulose to cement increases the compressive strength of the cement composite, but 2% addition decreases the compressive strength of the composite. The reason for this might be because of the change of the microstructure of the geopolymer composite when adding more methylcellulose. It has been previously found that the total porosity of cement composite increased markedly when the content of methylcellulose is greater than 1.47% of the cement composite (80). Therefore, the porosity also prominently increases when 1.2% of methylcellulose is added, which in turn leads to a decrease in the compressive strength of GP3 and FRG3. A similar observation is made after the addition of methylcellulose to the cement matrix (81).

The FRG group of samples has a slightly higher compressive strength than that of the GP group of samples when the content of added methylcellulose is the same.

Similar findings are observed for the GP with 2% PVA fibres as reinforcement in a previous study, whereby the compressive strength is higher than that of the GP without the added fibres (53). Steel fibres have been found to increase the compressive strength of lightweight cement-based composites because of the adequate bonding strength between steel fibres and the cement matrix (82). The inclusion of short fibres into the GP restrains the propagation of cracks, which changed the brittle damage failure mode to the ductile damage failure mode. However, the improvement in the compressive strength by the addition of HSPE and CS fibres is minimal. The reason could be the porosity in the GP, which is induced by the viscous geopolymer binding matrix (81).

(a)

(b)

Figure 3.5 Damage modes of the samples after the quasi-static compressive tests: (a) GP0; (b) FRG0

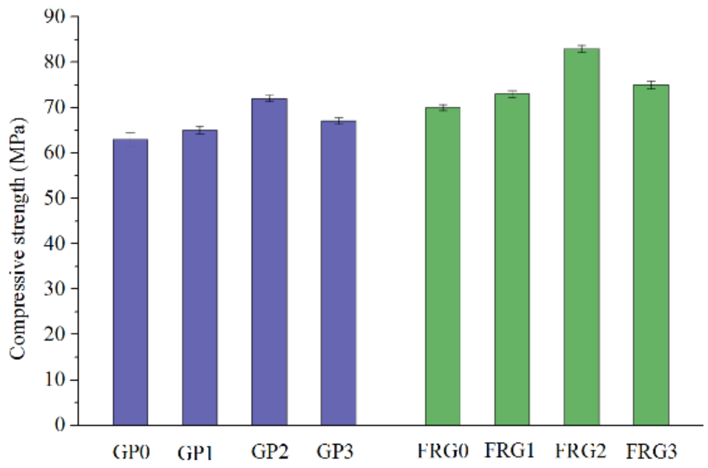

(a)

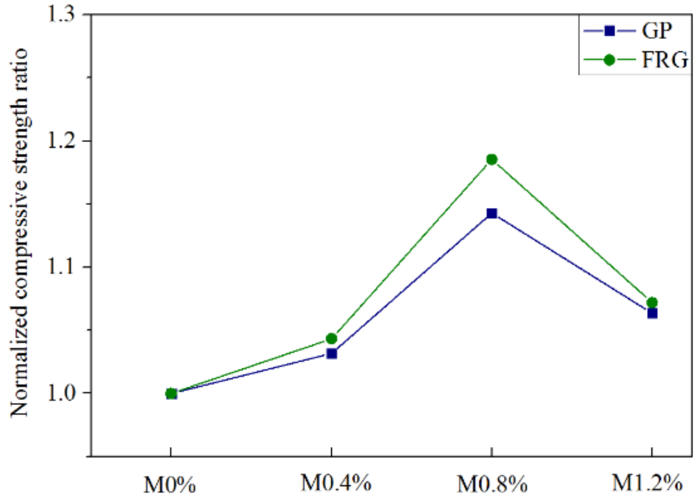

(b)

Figure 3.6 Effect of adding methylcellulose on the compressive strength of GP and FRG: (a) Compressive strength of GP and FRG; (b) Normalised compressive strength ratio of GP and FRG

SMOE is another critical property under compressive loading for GP and FRG, which can be obtained from stress-strain curves of the compression test. The typical stress-strain curves of the GP and FRG under compression tests are shown in Figure 3.7 and Figure 3.8, respectively. GP with and without the addition of methylcellulose has linear elastic behaviour and brittle failure; therefore, the SMOE for GP can be directly calculated from the stress-strain curves shown in Figure 3.7. For FRG, it exhibits elastic-plastic behaviour (Figure 3.8). The strain hardening state appeared after the initial elastic state and the strain-softening state occurs after the strain hardening state with the appearance of multiple cracks in the test samples. The addition of HSPE and CS fibres effectively improves the ductility of GP, which results in the change of damage mode from brittle to ductile. It has been shown that FRC experiences elastic behaviour until 40% of the ultimate load, followed by plastic behaviour (81). In the present study, the elastic limit of FRG is determined at approximately 30% of the ultimate stress and the SMOE was calculated accordingly.

The SMOE results for the GP and FRG samples are shown in Figure 3.9(a). The normalised SMOE ratios are calculated and shown in Figure 3.9(b). The SMOE of GP decreases when the methylcellulose content increases (Figure 3.9). The most significant decrease for GP is 8% when 1.2% methylcellulose (GP3) is added compared to GP0 (Figure 3.9(b)). A similar trend of SMOE is found for the FRG group. Increasing the methylcellulose content in the FRG decreases the SMOE of the FRG samples and the most substantial decrease is 12% for the samples with 1.2% methylcellulose (FRG3) compared to FRG0 with no addition of methylcellulose (Figure 3.9(b)). A previous study (61) confirms that the inclusion of methylcellulose increases the flexural strength of the cement matrix but decreased the SMOE. Methylcellulose is an organic polymer with the nature of viscosity and its modulus is very low. For example, the storage modulus of methylcellulose at room temperature in the frequency range from 10 to 10^4 Hz is 10^2 to 10^3 Pa (83). Therefore, the inherent low modulus of methylcellulose might be one of the reasons for the decreasing elastic modulus when increasing the methylcellulose content. Another reason might be the increasing porosity of the geopolymer composite when adding more methylcellulose.

It is also found that the SMOE of FRG is smaller than that of GP when the same amount of methylcellulose is added, as shown in Figure 3.9(a), indicating that the addition of CS and HSPE fibres decreased the SMOE of GP. Previous studies (32, 84) have reported that the addition of synthetic fibres such as HSPE fibres resulted in a decrease in stiffness compared to GP. The reason why adding HSPE fibres decreases the elastic modulus might be because the elongation of HSPE fibres is 3%, which is very high compared to GP and CS fibres (85). However, Khan et al. (84) found that the addition of steel fibres improved the modulus of GP. In the present study, because the diameter of the HSPE fibres is smaller than that of the steel fibres, the number of HSPE fibres is greater than that of the steel fibres given the same volume fraction. Therefore, the influence of adding HSPE fibres on the SMOE of the geopolymer composite (i.e. the decrement of SMOE) might be more severe than that of adding steel fibres on the SMOE of the geopolymer composite (i.e. the increment of SMOE), resulting in the overall decrement of SMOE for the FRG with steel fibre and HSPE fibre reinforcement. It should be mentioned that SMOE of the FRG is smaller that of concrete, it is because the developed FRG applies only geopolymer binder, fly ash and slag, without aggregates. Previous research on PVA fiber reinforced geopolymer composites by Nematollahi et al. (86) also has the similar results.

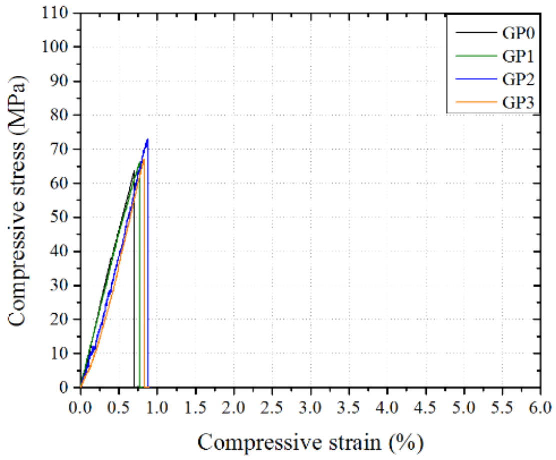

Figure 3.7 Typical stress-strain curves of GP in compression tests

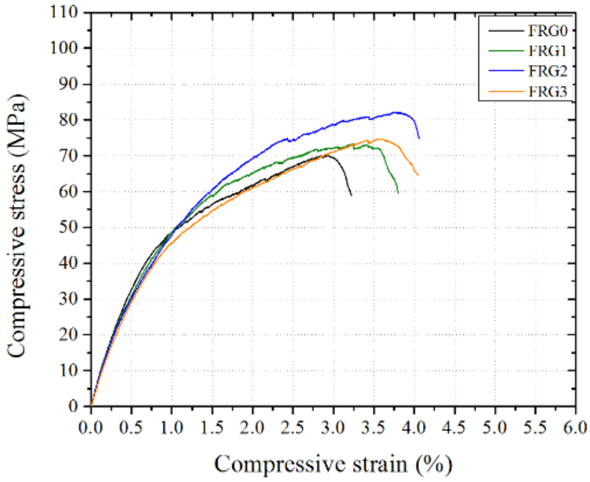

Figure 3.8 Typical stress-strain curves of FRG in compression tests

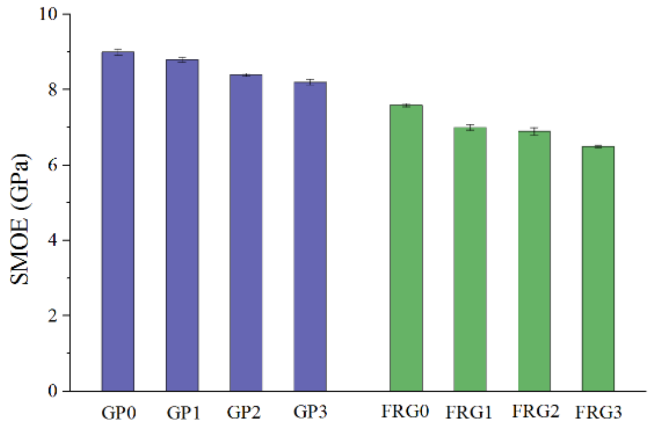

(a)

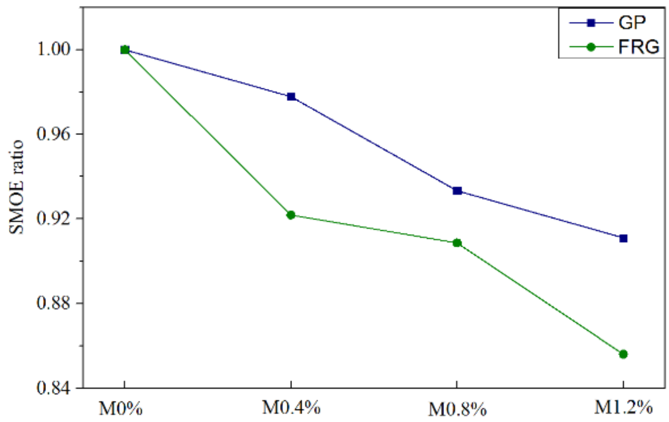

(b)

Figure 3.9 Influence of methylcellulose on the SMOE of GP and FRG: (a) SMOE of GP and FRG; (b) Normalised SMOE ratio of GP and FRG

3.3.1.2 Influence of methylcellulose on the behaviour of GP and FRG under flexural load

The behaviour of GP and FRG under flexural load is studied using the quasi-static test. The failure modes of GP and FRG under the flexural test are shown in Figure 3.10. The failure mode of GP under flexural load is the brittle failure mode; therefore, the test samples immediately collapsed after the failure load (Figure 3.10(a)). Similar trends are found for GP0, GP1, GP2, and GP3; therefore, the addition of methylcellulose does not affect the failure mode of GP0. The failure mode of FRG changes to a more ductile failure mode with a large deformation because of the inclusion of micro HSPE and CS fibres (Figure 3.10(b)). However, FRG1, FRG2, and FRG3 have similar failure modes to that of FRG0. After unloading, many fine cracks are observed in all FRG samples, e.g. the multiple fine cracks shown in Figure 3.11, indicating that HSPE and CS fibres could effectively hold the cracks of GP. Therefore, the addition of methylcellulose does not influence the failure mode of FRG0. It can be concluded that the addition of methylcellulose does not affect the failure mode of GP and FRG.

(a)

(b)

Figure 3.10 Typical failure modes: (a) GP1; (b) FR1

(a)

(b)

Figure 3.11 Photograph of FRG sample after failure: (a) Topview of FRG3; (b) Sideview of FRG3

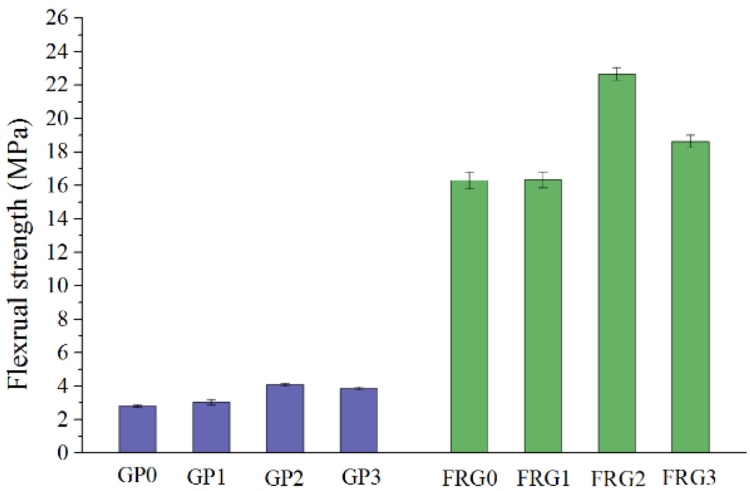

(a)

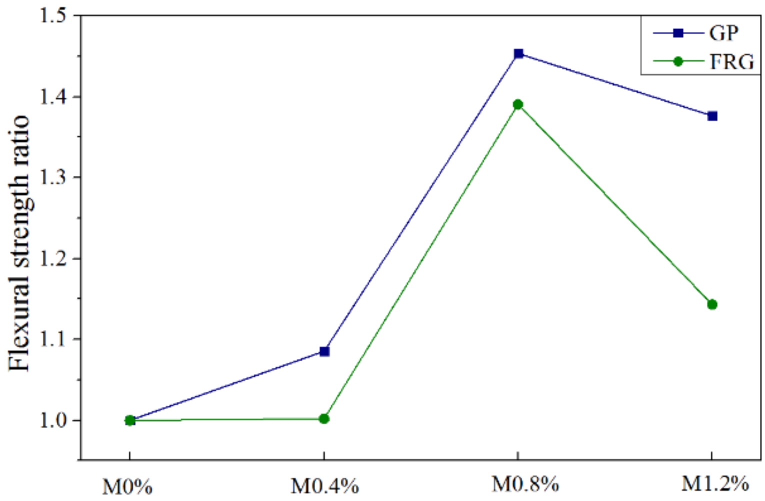

(b)

Figure 3.12 Influence of methylcellulose on the flexural strength of GP and FRG: (a) Flexural strength of GP and FRG; (b) Normalised flexural strength ratio

The average flexural strengths of GP and FRG are shown in Figure 3.12(a). The normalised flexural strength ratios of GP and FRG were calculated and are shown in Figure 3.12(b). The flexural strength of GP is the flexural stress when it suddenly drops to 0 MPa. The flexural strength of FRG is taken as P_{MOR}, which is the flexural stress vs the mid-span deflection curves, where the strain-softening stage is about to begin. As shown in Figure 3.12(b), the flexural strength ratios of GP1, GP2, and GP3 are larger than that of GP0, and the highest flexural strength ratio is 1.47 for GP2. Therefore, the addition of methylcellulose into GP0 increases the flexural strength and 0.8% addition of methylcellulose achieved the most significant improvement of flexural strength for GP. A similar trend is found for FRG. The flexural strength ratios of FRG1, FRG2, and FRG3 are larger than that of FRG0, with FRG2 having the largest flexural strength ratio (1.39). Therefore, the addition of methylcellulose into FRG improves the flexural strength and adding 0.8% of methylcellulose by weight achieved the best performance. The flexural test results for GP and FRG reflect that adding more than 0.8% methylcellulose into GP0 and FRG0 does not obtain a better flexural strength. This might be because of the influence of fibre distribution. It is found that adding 0.8% of methylcellulose to the cement composite achieved the best carbon fibre distribution; however, flocculation might occur if too high a methylcellulose content was added (60).

The flexural stress vs mid-span deflection curves of GP and FRG shows much more information about the behaviour of the test samples under flexural loading than that of the failure modes and flexural strength. The typical flexural stress vs mid-span deflection curves of GP and FRG are shown in Figure 3.13 and Figure 3.14, respectively. The horizontal axis represents the mid-span deflection (bottom in both Figure 3.13 and Figure 3.14) and the ratio of mid-span deflection to the span length (top in Figure 3.14). The flexural stress is estimated, according to Eq. (3.1). As shown in Figure 3.13, GP is very brittle and the flexural strength, as well as the deformation capacity, are very low compared to FRG, as shown in Figure 3.14. The load-deflection curves of GP exhibit greater linearity compared to the load-deflection curves of FRG. The load-deflection curves of FRG are nonlinear and showed both deflection hardening and softening behaviours. Therefore, it is more complex to explain the influence of adding methylcellulose on the flexural behaviour for FRG. The theory to analyse the behaviour of FRC materials is applied to study the flexural behaviours of the FRG samples.

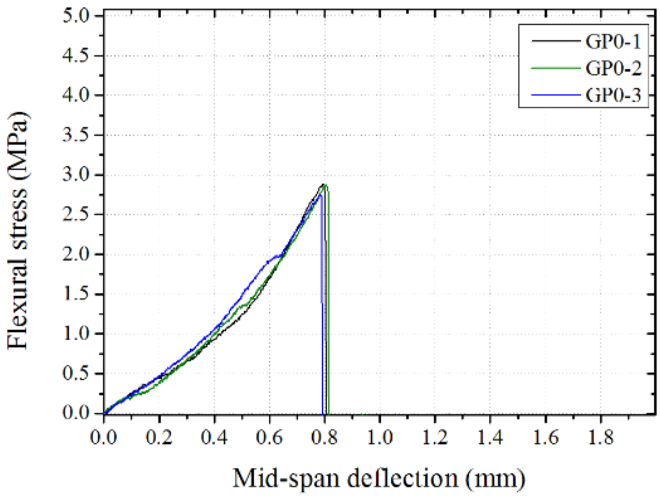

(a)

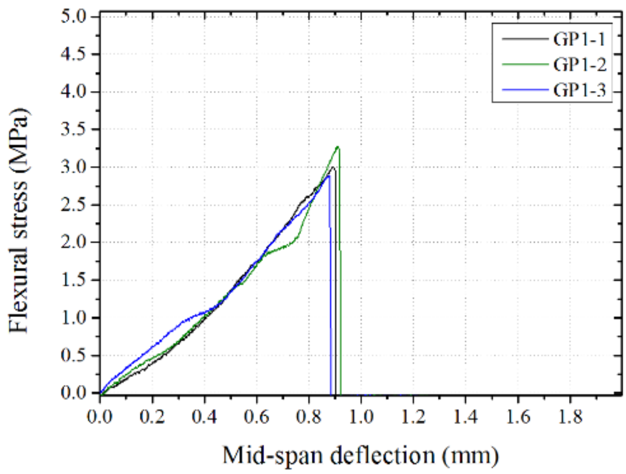

(b)

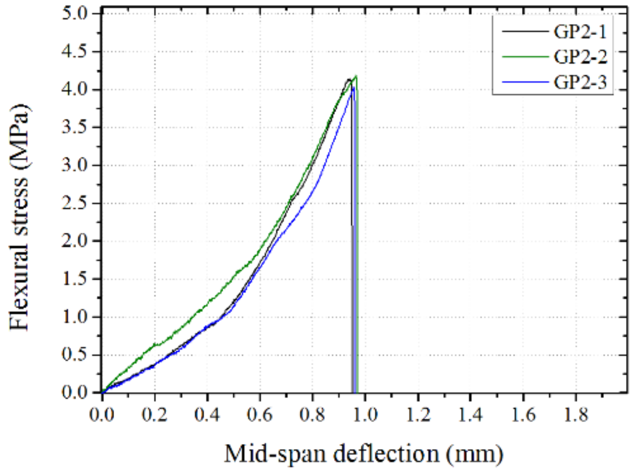

(c)

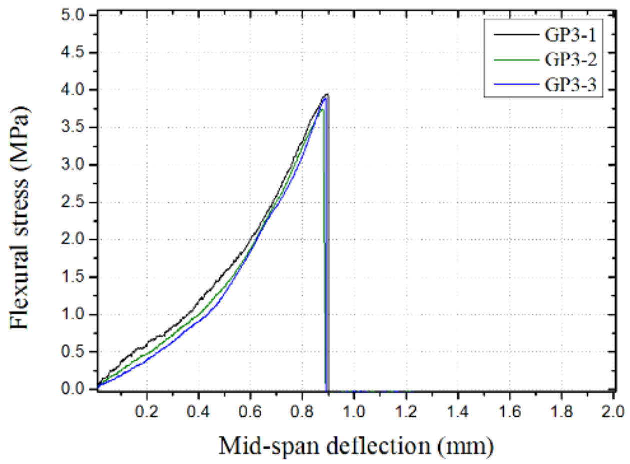

(d)

Figure 3.13 Flexural stress vs mid-span deflection curves: (a) GP0; (b) GP1; (c) GP2; (d) GP3.

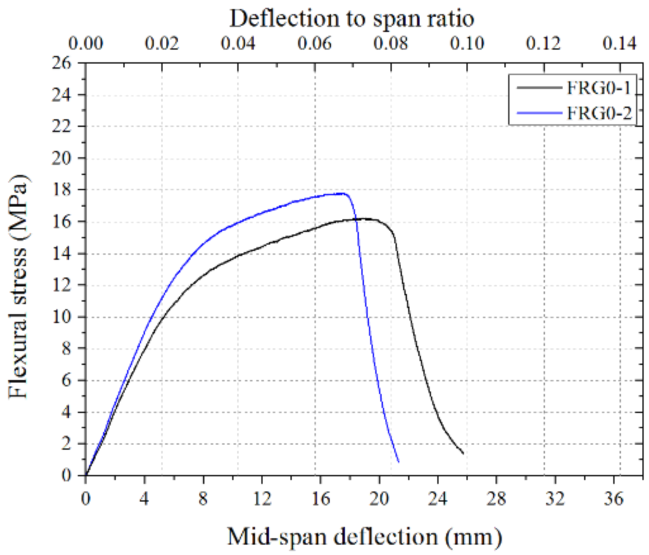
Deflection to span ratio
Flexural stress (MPa)
Mid-span deflection (mm)
FRG0-1
FRG0-2

(a)

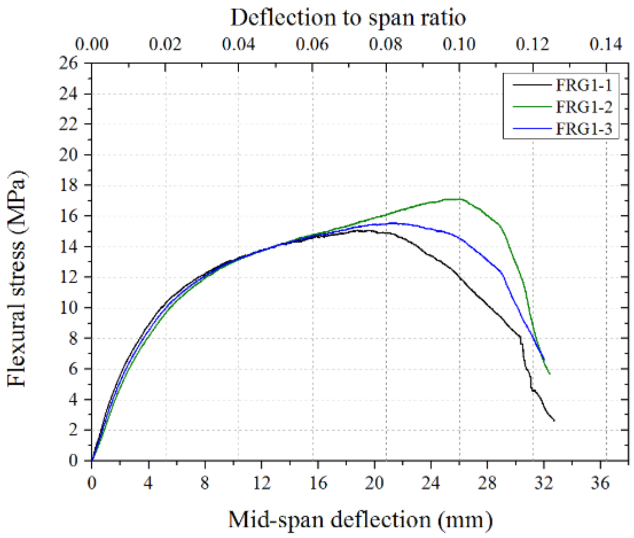
Deflection to span ratio
Flexural stress (MPa)
Mid-span deflection (mm)
FRG1-1
FRG1-2
FRG1-3

(b)

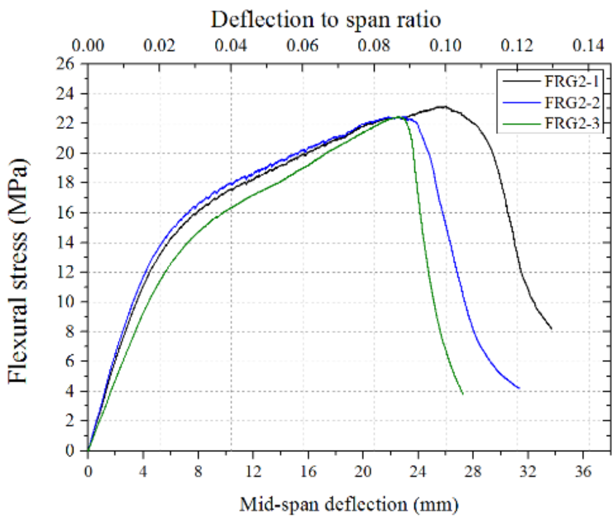
Deflection to span ratio
Flexural stress (MPa)
Mid-span deflection (mm)
FRG2-1
FRG2-2
FRG2-3

(c)

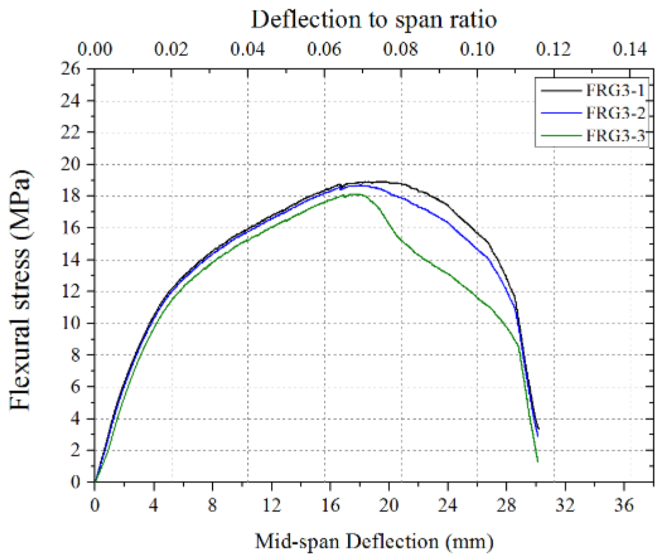

(d)

Figure 3.14 Flexural stress vs mid-span deflection curves: (a) FRG0; (b) FRG1; (c) FRG2; (d) FRG3.

The FRC materials have complex load vs deflection behaviour and are usually analysed by the method shown in Figure 3.15 (87). However, accurately identifying the first cracking load for FRC composite is complicated (32). In the present study, the method suggested by a previous study (87), which defined the point where the nonlinearity of the load-deflection curve appeared, is adopted to identify the first cracking point in the load-deflection curve. The typical load-deflection curves defined by the previous study (87) are shown in Figure 3.15. The load at the limit of proportionality (LOP) is designated as P_{LOP} and the corresponding deflection is defined as δ_{LOP}. MOR is defined as the ultimate flexural strength, which is characterised as the peak point of the load-deflection curve where deflection softening began. The load value at MOR is designated as P_{MOR} and the corresponding deflection is termed as δ_{MOR}.

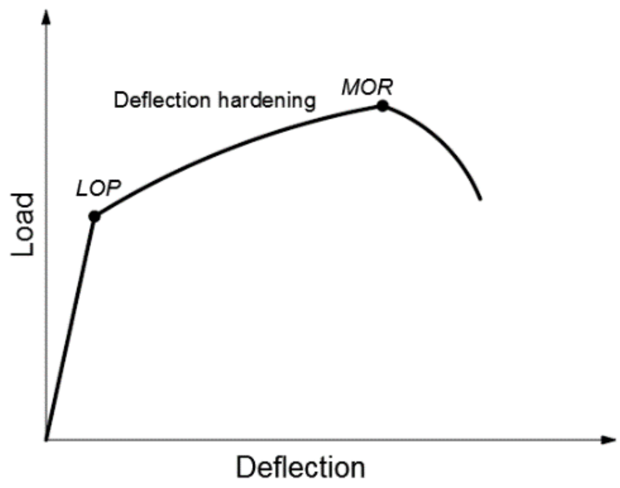

Figure 3.15 Typical load-deflection curve of FRG

The typical deformation behaviour of the FRG sample under flexural loading is shown in Figure 3.15, indicating a good ductility. As shown in Figure 3.14, the flexural stress vs mid-span deflection curves have a similar trend compared to the curve in Figure 3.15, including the deflection hardening and softening stages. Table 3.4 provides the average values of flexural behaviours for FRG. The effect of adding methylcellulose into FRG on its mechanical behaviour is investigated.

The deflection hardening behaviour of the composite can be enhanced by increasing the gap between the strength of LOP and MOR and their corresponding deflections. As shown in Table 3.4, the P_{MOR} is significantly larger than that of P_{LOP}, demonstrating deflection hardening behaviour. The average P_{MOR} value for FRG2 is 23.9 MPa, which is the highest among all the tested samples. The P_{MOR} of FRG3 is18.6 MPa, which is larger than that of FRG0 of 16.6 MPa. The P_{MOR} values are almost the same for FRG1 and FRG0. Therefore, adding methylcellulose is beneficial for increasing the P_{MOR} values of the short HSPE and CS FRG composite.

Table 3.4 Average values of flexural behaviours

Deflection		GP0	GP1	GP2	GP3	FRG0	FRG1	FRG2	FRG3
LOP	P_{LOP} (MPa)	-	-	-	-	5.5	5.1	6.2	5.6
	δ_{LOP} (mm)	-	-	-	-	1.8	1.9	2.1	1.9
L/100	$P_{L/100}$ (MPa)	-	-	-	-	6.1	6.7	7.9	7.8
	$\delta_{L/100}$ (mm)	-	-	-	-	2.8	2.8	2.8	2.8
L/20	$P_{L/20}$ (MPa)	-	-	-	-	16.0	14.2	18.8	17.4
	$\delta_{L/20}$ (mm)	-	-	-	-	14.0	14.0	14.0	14.0
MOR	P_{MOR} (MPa)	2.8	3.0	4.1	3.9	16.6	16.6	22.6	18.6
	δ_{MOR} (mm)	0.8	0.9	0.95	0.9	17.9	22.8	23.9	19.1
L/10	$P_{L/10}$ (MPa)	-	-	-	-	12.5	13.0	15.2	11.5
	$\delta_{L/10}$ (mm)	-	-	-	-	28.0	28.0	28.0	28.0

As specified in ASTM C1609 (75) and ASTM C1018 (88), the index representing the energy absorption capacity is the toughness, which is defined as the area under the load-deflection curve up to a certain value of deflection. It is found that the deflection at δ_{LOP} is not affected by adding the short HSPE and CS fibres. In contrast, the δ_{MOR}

of all samples is much higher than that of δ_{LOP}, indicating that adding short fibres significantly increases the ductility of GP. To quantify the influence of methylcellulose on FRG, the average δ_{MOR} values of FRG1, FRG2, and FRG3 are normalised by the average δ_{MOR} value of FRG. The results show that the normalised δ_{MOR} values of FRG1, FRG2, and FRG3 were 1.28, 1.33, and 1.06, respectively; therefore, the deflection hardening is increased by the addition of methylcellulose to FRG0. However, the increase is not monotonic with the content of methylcellulose, for example, 1.2% vs 0.8% in the present study. As discussed above, the amount of methylcellulose should be limited to 1.0% to achieve the best performance.

3.3.1.3 Influence of methylcellulose on the energy absorption capacity of FRG (toughness and toughness indices)

Energy absorption capacity is vital to ensure structural safety. Toughness and toughness indices of FRG are used to evaluate the energy absorption capacity. The influence of adding methylcellulose on the energy absorption capacity of FRG is studied by calculating the corresponding toughness and toughness indices. It is imperative to choose a proper value of deflection to calculate the toughness and compare the overall energy absorption capacity of different composites (86). In the present study, the toughness corresponding to the deflections of *L/100*, *L/20*, $\delta_{MOR,}$ and *L/10* are calculated and compared to evaluate the influence of adding methylcellulose on the energy absorption ability of FRG. The toughness of FRP0, FRP1, FRP2, and FRP3 corresponding to the deflections of *L/100*, *L/20*, $\delta_{MOR,}$ and *L/10* are shown in Table 3.5. The normalised toughness ratios of FRG0, FRG1, FRG2, and FRG3 are also calculated and are shown in Figure 3.16(a). The toughness ratios of FRG1, FRG2, and FRG3 at the deflections of *L/100*, *L/20*, δ_{MOR}, and *L/10* are generally higher than those of FRG0, except for the toughness ratio of FRG1 at the deflection of *L/20*. The flexural strength of FRG1 at the deflection of L/20 is also slightly smaller than that of FRG0 at the same deflection. This inconsistent behaviour could be caused by a testing error. Overall, adding methylcellulose increases the toughness of FRG. Besides, the toughness ratio after the addition of 0.8% methylcellulose is the largest for all selected deflections, such as *L/100*, *L/20*, $\delta_{MOR,}$ and *L/10*. Therefore, adding 0.8% of methylcellulose to FRG0 obtains the best improvement of toughness.

Table 3.5 Average toughness and toughness indices corresponding to different deflections for FRGs

	Deflection	FRG0	FRG1	FRG2	FRG3
Toughness (Unit: Nm)	L/100	8.4	10.3	11.4	11.5
	L/20	153.4	147.1	182.4	168.0
	δ_{MOR}	218.0	257.4	391.5	260.1
	L/10	272.5	350.1	452.6	399.0
Toughness indices	δ_{MOR}	45	56	59	50
	L/10	56	71	73	70

As specified in ASTM C1018 (88), the toughness indices are also used to evaluate the energy absorption capacities, which is defined by the area of the load-deflection curve up to a certain deflection level. Therefore, the toughness indices ratios of FRG corresponding to the deflection of δ_{MOR} and *L/10* are calculated to reflect the influence of methylcellulose on the energy absorption capacity, as shown in Figure 3.16. The toughness indices ratio for FGR1, FRG2, and FRG3 are larger than that of FRG0; therefore, the addition of methylcellulose effectively improves the toughness indices (Figure 3.16(b)). According to a study conducted by Naaman and Reinhardt (89), the composites are characterised as deflection hardening if the toughness indices are larger than 20. As shown in Table 3.5, the I_{MOR} and $I_{L/10}$ of all mix designs are larger than 20. Therefore, their flexural behaviour under bending can be classified as deflection hardening and the capacity can be quantified. The addition of methylcellulose is significantly beneficial for the deflection hardening behaviour of FRG0, with this influence most substantial when 0.8% methylcellulose by weight is added.

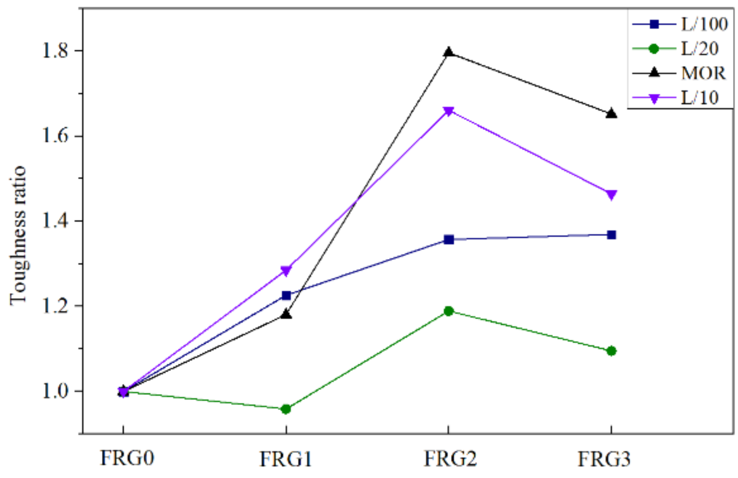

(a)

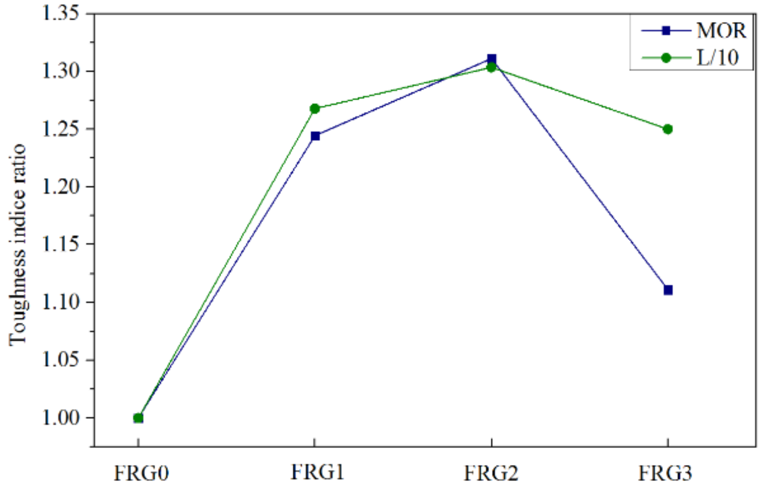

(b)

Figure 3.16 Normalised toughness ratio and toughness indices ratio: (a) Toughness ratio; (b) Toughness indices ratio

Therefore, the addition of methylcellulose up to 1.2% improves the mechanical properties of GP and FRG including the compressive strength, flexural strength, deformation ability, and toughness. In the present study, adding 0.8% of methylcellulose achieves the best mechanical properties for both GP and FRG. When the methylcellulose content is higher than 0.8%, the mechanical properties such as compressive strength and flexural strength decreases for both GP and FRG. From the perspective of material science, the mechanical properties should be related to the microstructures of the material. A previous study used a scanning electron microscope to study the microstructure of the cement-based composite with the addition of methylcellulose (80). The incorporation of Si-HPMC was found to help form a more homogeneous cement matrix, which contributed to the improvement of the mechanical properties. When too high a methylcellulose content was added, the cement-based composite had more micro pores compared to the cement-based composite with none or with a lower methylcellulose content. Thus, the development of the best mechanical properties of GP and FRG is determined by both the homogenisation of the GP and FRG microstructure and the porosities induced by the additional cellulose. This might be why adding a small amount of methylcellulose increased the mechanical properties of GP and FRG, but the mechanical properties of GP and FRG are compromised when too much methylcellulose is added. Additionally, the reinforced fibres played an essential role in the mechanical properties of FRG. The inclusion of 0.8% methylcellulose creates the best dispersion of carbon fibres and perfect bounding with the cement-based matrix, and a further increase in the methylcellulose content has been found to lead to fibre flocculation (60).

3.3.2 Influence of methylcellulose on the vibration characteristics of GP and FRG

The influence of methylcellulose on the vibration characteristics of GP and FRG is studied with the force hammer impact vibration test. From the hammer impact vibration tests, two main vibration characteristics of the samples are obtained, the fundamental frequency and the damping ratio. The fundamental frequency, which can be used to obtain the DMOE, and the damping ratio of the tested beams are identified to study the influence of adding methylcellulose on the stiffness and damping of GP and FRG.

3.3.2.1 Influence of methylcellulose on the fundamental frequency and DMOE of GP and FRG

The time-domain vibration responses of GP and FRG measured by the hammer impact vibration tests on the tested beam samples are transformed into the frequency domain using FFT. The signals measured from the test are normalised and filtered with a low-pass filter at a cut off frequency of 1200 Hz. The fundamental frequency of the tested GP and FRG samples are identified by examining the resonant frequency under the hammer impact vibration tests, which is the first significant peak value of the

Fourier spectrum of GP and FRG. The time-domain response and corresponding spectrum of GP and FRG obtained from the hammer impact vibration test are similar. A typical time-domain response and the corresponding FFT spectrum of FRG in the frequency domain are shown in Figure 3.17. The DMOEs of the tested GP and FRG samples are calculated from the fundamental frequency using Eq. (3.2).

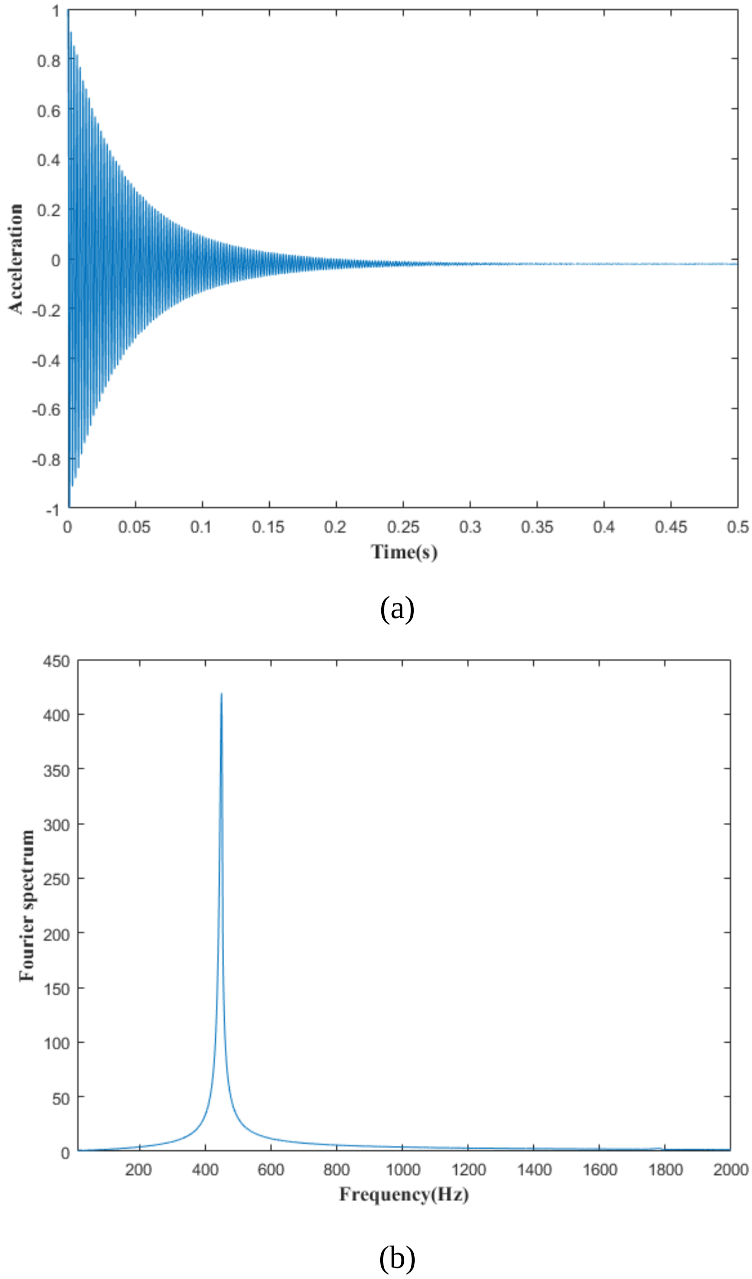

Figure 3.17 Typical acceleration response and analysis result on an FRG sample (a) Time-domain response; (b) FFT spectrum

Each GP and FRG design group had three samples and each sample is tested five times. Therefore, 15 time history records are used to obtain the average fundamental vibration frequency of each GP and FRG sample. DMOE is calculated from the obtained fundamental frequencies of the GP and FRG samples. The fundamental frequencies and DMOE of the GP and FRG samples are shown in Table 3.6 and Figure 3.18(a). The normalised DMOE ratios of the GP and FRG samples are also calculated and shown in Figure 3.18(b).

Table 3.6 Fundamental frequency and DMOE of each mix design

Specimens	Methylcellulose (%)	Fundamental frequency (Hz)	Dynamic modulus DMOE (GPa)
GP0	0	491	9.3
GP1	0.4	483	9.0
GP2	0.8	472	8.6
GP3	1.2	469	8.5
FRG0	0	451	7.8
FRG1	0.4	435	7.3
FRG2	0.8	431	7.2
FRG3	1.2	414	6.8

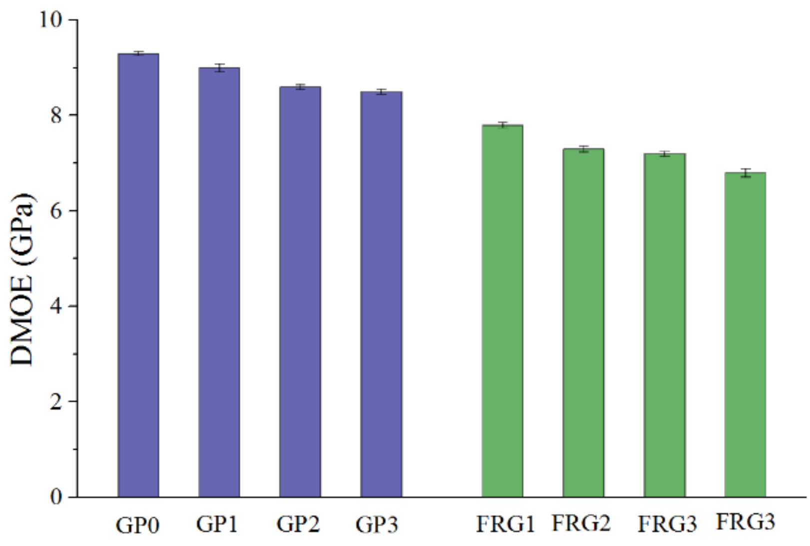

(a)

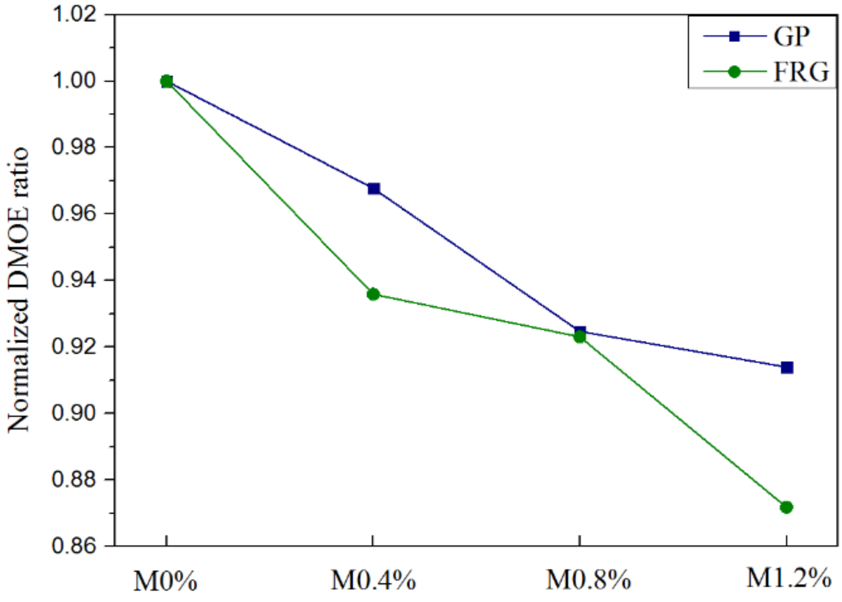

(b)

Figure 3.18 Influence of methylcellulose on the DMOE of GP and FRG: (a) DMOE of GP and FRG; (b) Normalised DMOE ratio of GP and FRG

As shown in Table 3.6 and Figure 3.18(b), when more methylcellulose is added to the mix, a smaller DMOE is observed for both GP and FRG. Furthermore, the DMOE of the GP and FRG decreases by nearly 9% and 13%, respectively, when the methylcellulose content increases from 0% to 1.2%. The higher the methylcellulose content, the larger the decrement of DMOE for GP and FRG. Similar to the influence of methylcellulose on SMOE, the reason for this reduction of DMOE when adding too high a methylcellulose content is because of the inherent low modulus of methylcellulose.

The DMOE of the FRG with CS and HSPE fibre reinforcement is lower than that of the GP without fibre reinforcement, as shown in Table 3.6 and Figure 3.18(a). The reason might also be because the influence of the HSPE fibres on the DMOE of the geopolymer composite (i.e. the decrement of DMOE) is more pronounced than that of the CS fibres (i.e. the increment of DMOE), which resulted in the overall decrement of DMOE for the FRG with micro CS fibre and HSPE fibre reinforcement.

3.3.2.2 The influence of methylcellulose on the damping ratio of GP and FRG

The influence of methylcellulose on the damping ratio of GP and FRG is also studied by the hammer impact vibration test. The damping mechanism of cementitious materials is very complex and it generally includes the following three components: (i) viscous damping; (ii) friction damping; and (iii) solid damping (16). Geopolymers consist of the solid phase, aqueous phase, and pores, which are very similar to cementitious materials. Therefore, the damping mechanisms might be similar to that of cementitious materials. There is no generalised theory to model all these complicated damping mechanisms; therefore, a commonly used method is to treat the complex system as a monophasic viscoelastic material and the damping ratio is adapted to indicate the damping mechanism (16, 78).

The damping ratios for the GP and FRG samples are identified to describe the energy dissipation capability of the samples as listed in Table 3.3. The identified damping ratio is structure-dependent. Considering that the same dimensions and boundary conditions are used for all samples, the conducted tests and identified damping ratios indirectly reflect the damping of materials. Figure 3.19 shows the typical time history of the acceleration response and damping ratio of a typical test sample (FRG3) using the exponential fitting method.

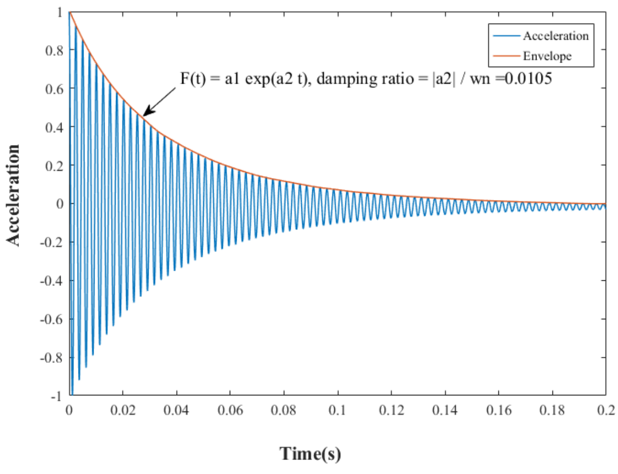

Figure 3.19 Typical acceleration time history to calculate the damping ratio of FRG3

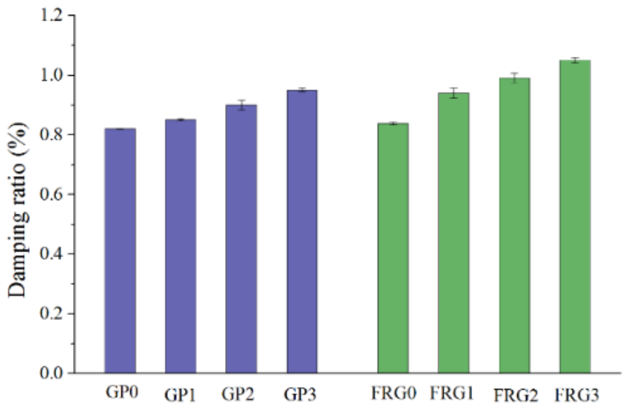

(a)

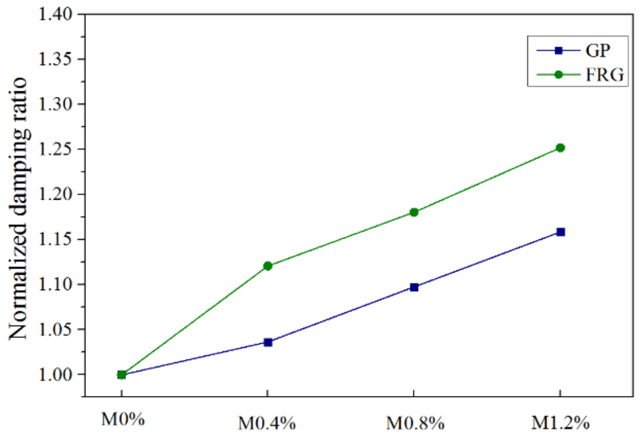

(b)

Figure 3.20 Influence of methylcellulose on the damping ratio of GP and FRG: (a) Average damping ratios of tested specimens: (b) Normalised damping ratio

A total of 15 time-domain records for each mix design of GP and FRG are used to identify the damping ratio for the fundamental vibration mode and the average values of the damping ratio for GP and FRG are shown in Figure 3.20(a). The normalised damping ratio is calculated to reflect the influence of methylcellulose on the damping ratio of GP and FRG more clearly, as shown in Figure 3.20(b). For the GP samples, the damping ratios of GP1, GP2, and GP3 are normalised by the damping ratio of GP0. For the FRG samples, the damping ratios of FRG1, FRG2, and FRG3 are normalised by the damping ratio of FRG0. The damping ratios of GP and FRG increase with increasing methylcellulose content. The higher the methylcellulose content, the higher the normalised damping ratio of the GP and FRG is. The GP3 sample with 1.2% of methylcellulose has a normalised damping ratio of 1.15; therefore, adding 1.2% of methylcellulose increases the damping ratio of GP0 by 15%. In addition, the damping ratio of FRG3 with the addition of 1.2% methylcellulose is 1.25; therefore, adding 1.2% of methylcellulose causes an increase of 25% in the damping ratio of FRG0. Thus, the damping ratio can be increased by adding methylcellulose to GP and FRG. In addition, adding more methylcellulose increases the damping ratio of GP and FRG more significantly. However, adding more methylcellulose does not necessarily yield the best mechanical properties. Therefore, when adding methylcellulose to improve the mechanical and vibration properties of GP and FRG, the methylcellulose content should be determined based on the application purpose. For example, a higher content of methylcellulose can be applied for GP and FRG when high material damping is required. Otherwise, 0.8% of methylcellulose can be added to GP or FRG to achieve better mechanical properties.

There has been limited research regarding the damping properties of geopolymer composites. It has been previously shown that fly ash-based geopolymer mortar has a damping ratio varying from 1.7% to 2.63%, which was obtained by comparing the numerical simulation results with the force vibration test results (16). The free vibration test was conducted on a cantilever beam with dimensions of 160 × 15 × 5 mm. This damping ratio was higher than the fly ash and slag-based GP and FRG developed in this study. This could be due to the different mix design of geopolymer and the different test setup including the dimensions and boundary conditions. The damping ratios of tested samples are structure-dependent. In the previous study and the present study, different boundary conditions and structural dimensions were used during the testing, leading to different damping ratio results. Another previous study (78) reported the influence of PVA fibre on the vibration characteristics of the FRC composite. The impact resonance test was conducted to determine the damping ratio of 400 × 100 × 75 mm prisms and a soft rubber support was used to permit the sample to vibrate freely in each mode of vibration. The obtained damping ratio for PVA fibre-reinforced FRC varied from 0.8% to 1.2% based on the different volume content of PVA fibres, which was similar to the damping ratios of FRG obtained in the present study. The available information regarding the damping properties of geopolymer-based composite is very limited. The present study indirectly evaluated the damping properties and energy dissipation capacity of GP and FRG, considering that the damping ratios were structure-dependent.

3.4 Summary

The present study investigates the mechanical properties and vibration characteristics of newly developed GP and FRG using methylcellulose as the organic admixture. The methylcellulose content is 0%, 0.4%, 0.8%, and 1.2% of the solid ingredients by weight for each mix design. The fly ash and slag-based GP with methylcellulose are prepared and then reinforced by hybrid short fibres. The short fibres include 1% copper CS fibres and 1% HSPE fibres in volume fraction. The following observations and conclusions are made:

1. The compressive strength of GP and FRG is 63–83 MPa. The inclusion of CS and HSPE fibres successfully changes the damage pattern from brittle to ductile. The addition of fibres effectively suppresses the development of multiple micro-cracks of GP under quasi-static compressive loads.
2. Adding methylcellulose is beneficial for increasing not only the loading bearing capacity for GP and FRG but also the ductility of FRG. FRG2 with 0.8% methylcellulose added (by mass of solid geopolymer ingredient) has the highest flexural strength of 22.6 MPa and its deflection at the peak load is approximately 10% of the span.
3. As indicated by the toughness and toughness indices, the FRG developed in the present study has a good energy absorption capacity. Adding methylcellulose to the FRG enhances its toughness and toughness indices.

The normalised toughness ratio of FRG2 is 1.8; therefore, adding 0.8% of methylcellulose increases the toughness ratio by 80%.

4. Adding methylcellulose slightly decreases the SMOE and DMOE of both GP and FRG. The higher the methylcellulose addition, the lower the SMOE and DMOE are observed in both GP and FRG.
5. Adding methylcellulose effectively increases the damping ratios of both GP and FRG. The damping of GP0 is improved by 15% when 1.2% of methylcellulose by weight is added. For FRG, the damping ratio is improved by 25% when 1.2% of methylcellulose is added to FRG0.

4 Failure mechanism of geopolymer composite lightweight sandwich panels under flexural and edgewise compressive loading

4.1 Introduction

In recent years, the sandwich structure has earned a reputation as an effective solution for building construction owing to its high strength-to-weight ratio and adequate levels of acoustic and thermal insulation. Therefore, sandwich panels have been applied in the field of civil infrastructures and building structures (23). The typically applied sandwich structure consists of thin skin layers that are stiff enough to sustain the tension force and with a relatively light core layer that is thick enough to sustain the shear strength. The skin layers and core layer are usually bonded with an adhesive. Typical skin layers are composed of different materials, such as steel or aluminium, FRP systems, and cement-based composites. The core layer is typically made from polymeric foams, mineral wool, and balsa wood. Extensive studies have been undertaken to develop new generation solutions for these structural elements and their mechanical behaviours under different loading conditions have been studied (23, 29-31). Unlike structures built with monolithic materials, the failure mechanisms of sandwich structures are very complex under different loading conditions. Bending moment and axial loading are two extreme loading conditions that sandwich panels might be subjected to when they are used as wall and floor panels in prefabricated buildings. When the sandwich panel is subjected to a bending load, the possible failure modes include face yield failure, face wrinkling, face indentation, and core shear failure (90-92). When the sandwich panel undergoes an edgewise compression load, the possible failure modes are Euler macro buckling, macro core shear buckling, and face wrinkling (93, 94). The complexity of the failure mechanism might come from the geometry, different mechanical properties of the skins and core, and the interaction between them. Therefore, the measurement and tracking of the failure progress of the entire sandwich panel are fundamental for analysing the failure mechanism of the sandwich panel subject to bending moment and edgewise compression load.

DIC is an optical deformation analysis that compares a series of pictures of the deformation process of targeted objects captured by cameras, with the reference picture taken as the initial picture before loading. The fundamental principle is based on the fact that the gradient of grayscale values of a specific area (facet) in the undeformed state corresponds to the gradient of grayscale values of the same area in the deformed states, as schematically shown in Figure 4.1 (95). As observed, the imposed red square is the subset (a set of pixels) for tracking the movement of its centre point *P(x,y)* from the reference image (before deformation) to deformed image *P'(x',y')*. The tracking of subset is conducted using selected correlation functions such as Cross-correlation (CC) or normalized cross-correlation (NCC) (96). Subsequently, the strain fields, including shear strain, can be derived by smoothing and differentiating the displacement fields. Thus, every single facet can be viewed as a tiny virtual strain gauge and the deformation information can be obtained. Massive facets can form a full surface with the full-field deformation information of the target object. Therefore, DIC is a suitable measuring and tracking method for obtaining the deformation information and failure mode of sandwich structures under different loading conditions because it can capture the full-field of deformation information of both the skins and the core. The accuracy and quality of the DIC strongly depend on the surface visual details and contrast. To obtain high-quality surface features, a random pattern of paintings is usually applied on the surface of the sample (97).

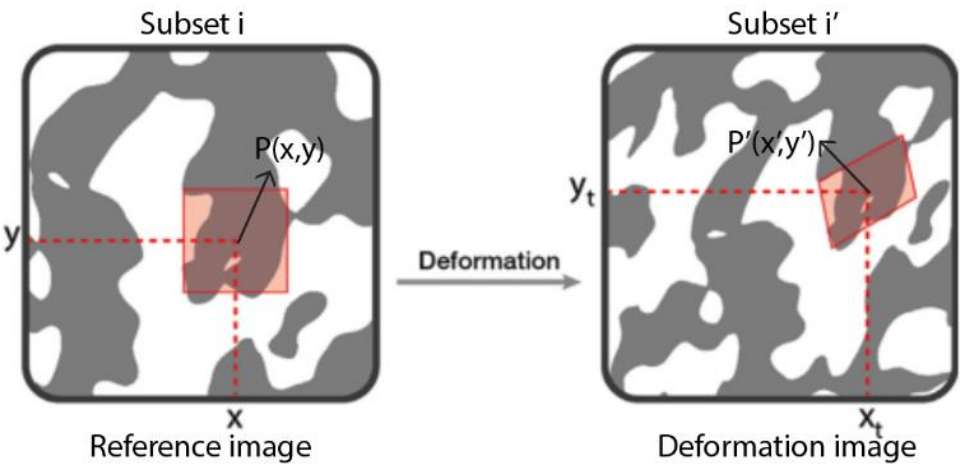

Figure 4.1 Schematic explanation of the grayscale distribution of a facet in the non-deformed (left) and the deformed (right) states (95)

In this chapter, the sandwich concept is applied to develop lightweight panels for prefabricated buildings. PUR foam is used as the core layer and FRG composite is used as the skin layer of the sandwich panel. The core shear and skin layer failure mechanisms of the developed sandwich panel under three-point bending are studied using the DIC method. The analytical solution for predicting the core shear and skin layer tension failures is based on the experimental study results. The failure mechanism of the developed sandwich panel undergoing the edgewise compression load is also studied using the DIC method. The analytical solution for predicting the critical buckling load is shown based on the experimental study results.

4.2 Preparation of samples

4.2.1 Application of developed lightweight sandwich panel

The lightweight sandwich panel developed in the present study is suitable for use in prefabricated buildings. The developed sandwich panels use FRG as the top and bottom skin layers. The applied microfibres to reinforce the geopolymer composite are a combination of micro CS and HSPE fibres. Utilising FRG as the skin layer provides sound flexural stiffness and impact resistance. PUR foam is used as the core of the sandwich panel. The foam core can provide adequate thermal insulation and reduce the total weight of the developed sandwich panel. PUR foam has the lowest thermal conductivity value among the conventional thermal insulation materials and it can improve the damping capacity of the sandwich panels (98). Two layers of FRG skins and PUR foam core are adhered using epoxy resin. The developed lightweight sandwich panels could be used for various structural components, such as wall panels, floor panels, roofs, and building façade, which can be used for not only traditional building systems but also prefabricated building systems such as modular buildings.

4.2.2 Manufacture process of the proposed structural lightweight sandwich panels

The manufacturing process of the proposed lightweight sandwich panel involves the following two phases, namely: (1) Casting the FRG to form the top and bottom skin layers for the developed sandwich panel; and (2) Assembling the bottom skin layer, core layer, and top skin layer to form the entire sandwich panel.

High-performance fibre-reinforced cement composite (HPFRC) has been well developed to possess strain hardening and multiple cracking behaviours under tension and bending loads (99). Engineered cementitious composite and ductile fibre-reinforced cementitious composite as components of HPFRC have drawn much attention in recent years. Short fibre-reinforced cement-based composites with a fibre volume content between 2% and 3% are used owing to their workability during mixing (74). They have a higher peak load and corresponding deflection capacity compared to regular cement-based composites. Similarly, FRG, as a sustainable material, also has an impressive load-bearing capacity with good deformation behaviour owing to the hybrid microfibre reinforcement (74, 84-86). Accordingly, the FRG applies CS and HSPE fibres as reinforcement. Fly ash and slag are the main geopolymer binder and they were supplied by Gladstone and Choice of Builders, respectively. The fly ash is classified as class F according to ASTM C618 (100). The chemical compositions of the fly ash and slag are given in Table 3.1 (37). The 12 M sodium hydroxide solution and D-grade sodium silicate solution were supplied by PQ Australia Ltd. and are used as the activator for the Geopolymerizaiton process.

The sodium hydroxide and sodium silicate were mixed and placed for 30 min, and then geopolymer binders including the fly ash and slag were poured into a 70 L mixer. After mixing for 3 min, the alkaline solution as the activator was poured into the mixer and mixed with the other ingredients for another 3 min. Then, the micro CS and HSPE fibres were slowly poured into the mixer, and all the ingredients were mixed until the fibres were well dispersed. The volume fraction of microfibers for reinforcing the geopolymer matrix is 2% in total, consisting of 1% of CS fiber and 1% of HSPE fiber. The geometric and material properties of the used CS and HSPE fibers are given by the supplier and listed in Table 3.2. The solid ingredients include 99.2 % of Geopolymer ingredients and 0.8% of methylcellulose. The Geopolymer ingredients include 80% of fly ash and 20% of slag. The weight ratio between the activator solution and the solid ingredient is 0.5. After that, the mixture was poured into a plywood mould. The FRG board was then placed and cured in an ambient environment for 24 h. The FRG board was placed in the ambient environment for curing for 28 days before assembling the sandwich panel. The FRG board was demolded from the plywood mould after 28 days curing and is then used as the skin of the sandwich panel.

During the second phase of preparing the studied sandwich panel, the FRG board was laid on a steel platform, which was used as the bottom skin layer of the sandwich panel. The surface of the FRG bottom skin layer was cleaned with surface cleaner to remove any retained dust and oil. The two surfaces of the PUR foam were also cleaned with a vacuum cleaner to remove the dust and any small retained particles on the surface. The properties of the applied PUR foam (P1 with lower density and P2 with higher density) provided by the supplier are listed in Table 4.1. The epoxy resin was spread on the surface of the bottom skin layer with a brush. Then, the foam core was placed on the top of the FRG bottom skin layer. The epoxy resin was also applied on the surface of the PUR foam core and the FRG top skin layer was placed on top of the foam core. The schematic manufacturing process is shown in Figure 4.2. The properties of the applied epoxy resin West System 105-206 are shown in Table 4.2 (101). After the sandwich panel is successfully manufactured, the side surface of the specimen is prepared for the DIC measurement. First, the side surface of the sandwich panel is cleaned with a vacuum cleaner. Then, it is painted white with a brush. Finally, random black spots with different size are made by a spray paint to get a high-contrast surface future. The accuracy of the DIC technique is verified by matching the reading from strain gauges and LVDTs before the testing.

Table 4.1 Properties of the PUR foam

	Density (kg/m3)	Compressive strength (MPa)	Elastic modulus (MPa)	Shear strength (MPa)	Shear modulus (MPa)
PUR foam1	35	0.23	5.5	0.13	1.2-1.6
PUR foam2	96	0.99	25	0.8	/

Note: Specified by the manufacturer

Table 4.2 Properties of epoxy resin (101)

Properties	West System 105-206
Tensile strength (MPa)	50.3
Tensile modulus (MPa)	3171.6
Tensile elongation (%)	4.5
Resin/Hardener Mix Ratio	5:1 by Volume
Shear Strength (MPa)	8.6

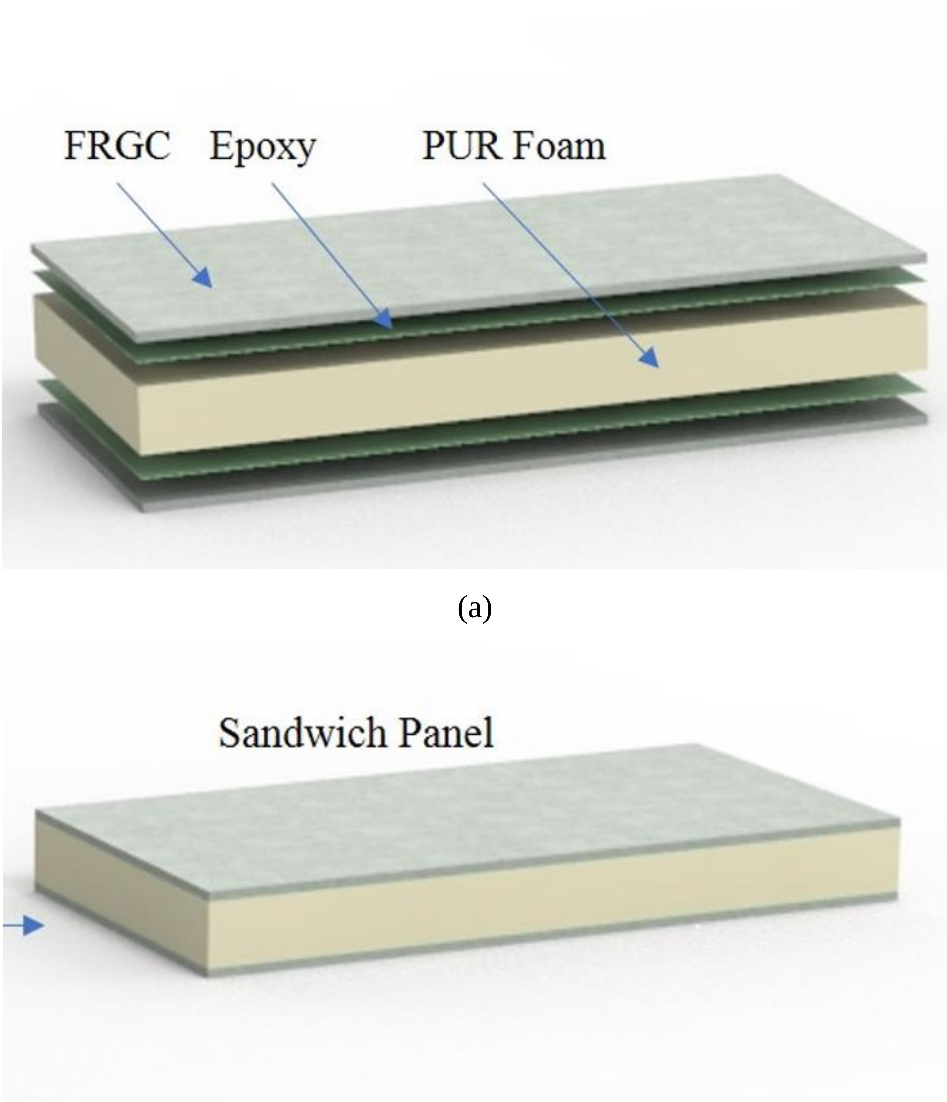

(a)

(b)

Figure 4.2 Manufacturing method of the proposed sandwich panel

4.3 Experimental program and test setup

4.3.1 Material properties of FRG and test setup

An experimental program is designed to verify and assess the material properties of the FRG. A compressive test is performed to examine the compressive strength and elastic modulus of the FRG. Direct tensile tests on an un-notched dog-bone type sample and bending tests on un-notched samples are conducted to obtain the mechanical properties of FRG under tension and flexural loadings, respectively.

Based on the ASTM C39 (102), the compressive test on the developed FRG is conducted to obtain the compressive strength. The elastic modulus is tested based on ASTM C469 (103). The dimensions of the test samples are a 200 mm high cylinder with a diameter of 100 mm, and the loading rate is set at 0.05 MPa/s. The applied load and corresponding strain of the test samples are recorded. The detailed compressive test setup is shown in Figure 4.3.

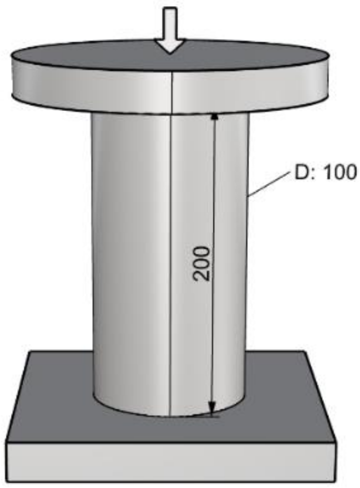

(a)

(b)

Figure 4.3 Compressive test setup for FRG material: (a) Dimensions of the sample (Unit: mm); (b) Experimental setup

Dumbbell shape (similar to a dog-bone) specimens and the corresponding test method is applied based on the recommendations from a previous study (104). The geometry of the designed dumbbell shape sample is shown in Figure 4.4. The advantages of the designed dumbbell shape include: (a) a central part with a constant or nearly constant section area to develop diffuse multiple cracks, (b) a large support section area to avoid the support failure, and (c) smooth transition from the support to the middle part to avoid the influence of stress concentration. The detailed test setup is shown in Figure 4.5. The loading rate is set at 0.01 mm/s according to a previous study (104).

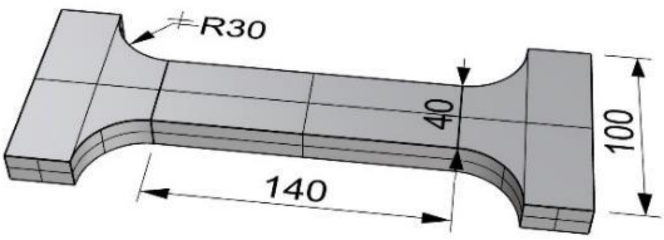

(a)

(b)

Figure 4.4 Dumbbell shape test sample used for the direct tensile test: (a) Detailed dimensions of the dumbbell shape sample (Unit: mm); (b) Samples used in the test.

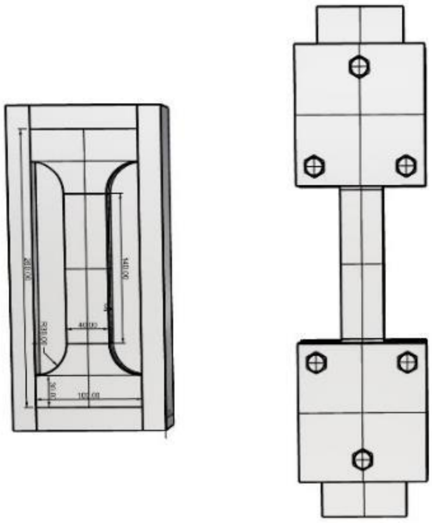

(a)

(b)

Figure 4.5 Direct tensile test setup for FRG material: (a) Schematic diagram; (b) Experimental setup

Four-point bending tests are performed to capture the deflection hardening behaviour of FRG under bending moment, according to the setup used in a previous study (74). The specimens are un-notched with dimensions of 300 × 75 × 15 mm (length × width × height). The span of the test specimen is kept as 280 mm. The loading rate is set at 0.01 mm/s, which is the same as that used for the tensile tests. The detailed experimental setup is shown in Figure 4.6. During the test, the applied load and corresponding deflection at the mid-span are recorded. The flexural strength is estimated using the following equation from the ASTM C 1609 (105)

$$f = \frac{P \cdot L}{b \cdot d^2} \quad (4.1)$$

where, f is the strength (MPa), P is the load (N), L is the span length (mm), b is the average width of the specimen (mm), and d is the average depth of the specimen (mm). The summary of specimen designs for direct tensile and flexural test is shown in Table 4.3.

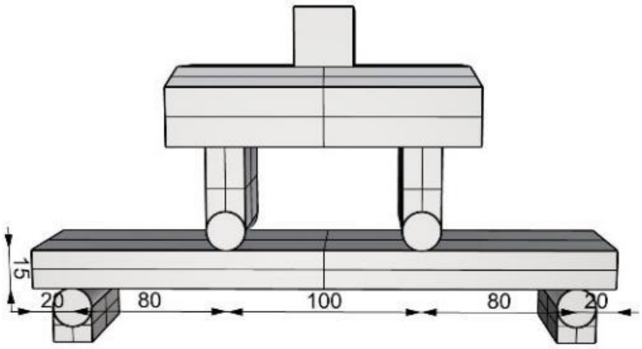

(a)

(b)

Figure 4.6 Four-point bending test setup for FRG material: (a) Schematic diagram; (b) Experimental setup

Table 4.3 Details of samples for the material properties test of FRG

Test purpose	Test group	Thickness (mm)	Width (mm)	Length/span (mm)
Direct tension	DT	15	40	140
Flexural test	GF	15	75	280

4.3.2 Bending test setup

A quasi-static bending test is designed to study the failure mechanism of the developed sandwich structures under bending. The one-way sandwich panel samples in the present study are used to study the failure mechanism of the developed sandwich structures. Two different failure mechanisms are considered: core shear failure and skin tensile failure. The shear behaviour and global stability of one-way sandwich panels with foam cores under three-point loading are strongly affected by the shear response of the core material. To investigate the shear failure of PUR foam core, PUR foam P1, which has a lower strength, is used to make the core of the sandwich panels in this set of bending tests. Sandwich panels with PUR foam P1 core and different core thickness-to-span ratios are prepared and tested to study the core shear behaviours of sandwich panels. To induce the tensile failure of the skin layer of the developed sandwich panels under bending, another set of panels are made by using PUR foam P2, which has a higher strength as indicated in Table 4.1, as core. The sandwich panels with different skin thickness-to-span ratios are made and tested to investigate the performance of panels under bending when the skin of the panel is vulnerable to the tensile failure.

The static flexural test setup of small scale specimens of the developed lightweight one-way sandwich panel is the same for studying both the core shear failure and skin tensile failure, and is performed following ASTM D393 (106). The detailed setup is shown in Figure 4.7. The displacement control loading method is applied during the three-point bending tests with a constant loading rate of 1 mm/min. The applied load and deflection are recorded and the full-field deformation is measured and tracked using DIC.

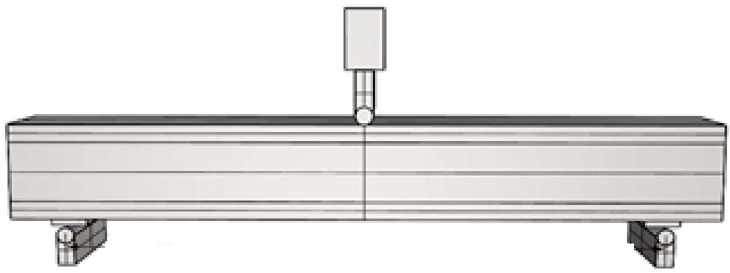

(a)

(b)

Figure 4.7 Setup for three-point bending test: (a) Dimensions of the sample (Unit: mm); (b) Experimental setup

Two groups of samples are prepared to study the core failure mechanism (C group) and the skin tensile failure mechanism (T group). The same FRG material is applied in both groups as that of the skin layer for the sandwich structure. However, the foam core for the C group use the PUR foam P1 and the T group used the PUR foam P2 as the core layer. The span for the C group bending test is set at 500 mm with simple roller supports. Three different core thickness-to-span ratios are considered during the C group tests, which corresponded to thicknesses of 80 mm, 130 mm. and 180 mm. The skin thickness for the T group is kept at 15 mm, with the span ranging from 600 mm, 800 mm, and 1000 mm. The width of the specimens for both the C and T groups is set at 75 mm. The details of specimens in C and T groups for bending test are given in Table 4.4.

Table 4.4 Details of the samples for the bending test

Test Purpose	Test group	PUR foam density (kg/m^3)	Thickness of FRG skin t (mm)	Thickness of PUR core c (mm)	Section thickness (mm)	Span L (mm)	Core or skin thickness/span (c/L or t/L) *
Core shear failure (C group)	C1	35	15	50	80	500	0.1
	C2		15	100	130	500	0.2
	C3		15	150	180	500	0.3
Skin tensile failure (T group)	T1	96	15	50	80	600	0.025
	T2		15	50	80	800	0.018
	T3		15	50	80	1000	0.015

Note: * For C group, the last column is core thickness/span (c/L); For T group, the last column is skin thickness/span (t/L).

4.3.3 Testing setup for edgewise compression test

The compressive properties of the developed lightweight sandwich panel are experimentally investigated by applying the in-plane load along the edgewise direction as specified in the standard ASTM C364 (107). The loading is applied along the length of the panel in the quasi-static conditions and the displacement control loading method is used in the compressive tests with a constant displacement loading rate of 1 mm/min. The detailed test setup is shown in Figure 4.8. The top and bottom sides of the test samples are clamped laterally to avoid slippage and any eccentric load on the test samples. The width and thickness of the test samples are kept at 200 mm and 180 mm, respectively. Three test groups (G1, G2 and G3) with different lengths are measured that are 200 mm, 400 mm, and 600 mm. The applied load and deformation of the test samples are recorded and the DIC method is applied to record the full-field deformation. The designs of test specimens are given in Table 4.5.

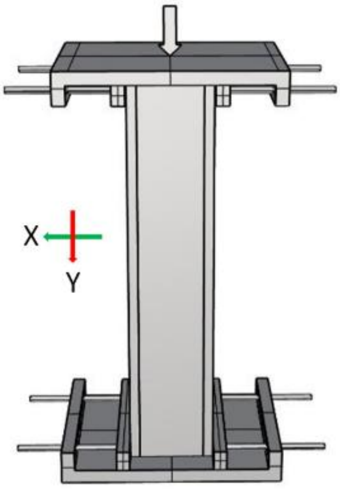

(a)

(b)

Figure 4.8 Test setup: (a) Designed test setup; (b) Test setup

Table 4.5 Designed test samples for the edgewise compressive test (G1-G3)

Test group	PUR foam density (kg/m3)	Thickness of FRG skin (mm)	Thickness of PUR core (mm)	Length of sandwich panel (mm)	Thickness-to-length ratio
G1		15	150	200	0.90
G2	35	15	150	400	0.45
G3		15	150	600	0.30

4.4 Results and discussions of sandwich panel under flexural loading

4.4.1 Material test results of FRG material

Compressive tests, direct tensile tests, and four-point bending tests are performed to determine the mechanical properties of the developed FRG material. The DIC method was applied to record the deflection and strain data. Direct tensile test results for FRG as the skin of the developed sandwich panel are shown in Figure 4.9. Four-point bending test results for FRG are shown in Figure 4.10. The density and mechanical properties obtained from the tests are provided in Table 4.6.

Table 4.6 Material properties of FRG

Material	Density (kg/m^3)	Modulus of elasticity (GPa)	Compressive strength (MPa)	Flexural strength (MPa)	Tension strength (MPa)
FRG (Standard deviation)	2025.20 (5.6)	13.33 (0.65)	57.32 (0.81)	18.50 (1.01)	7.13 (0.66)

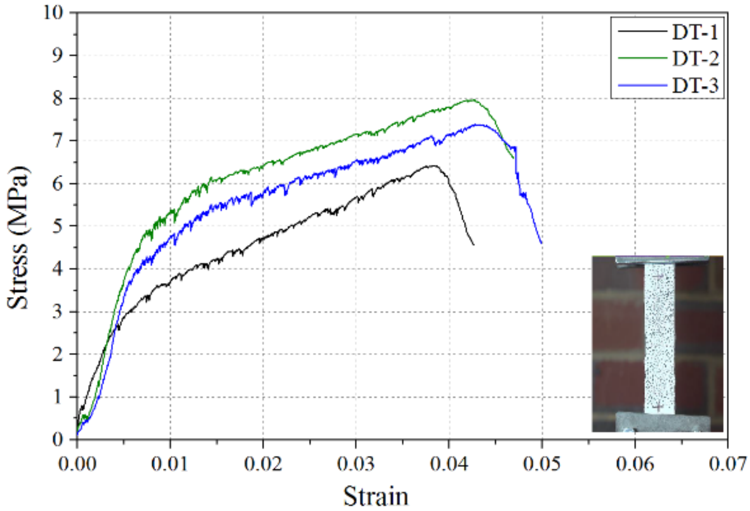

Figure 4.9 Direct tensile test results

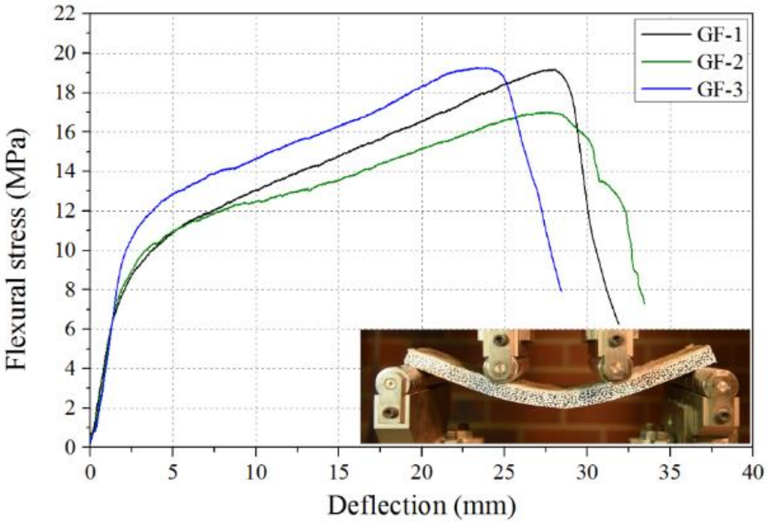

Figure 4.10 Four-point bending test results

FRG exhibits excellent deflection hardening and multiple crack behaviour, as shown in Figure 4.9 and Figure 4.10. The diffuse multiple crack pattern appears during the deflection hardening phase until the macro-failure cracks appeared in the final failure state. The formation of multiple micro-cracks means that the short fibres could effectively bridge the opening of cracks. Therefore, new cracks form in close vicinity, which is not only beneficial for the strength but also for the durability resistance under aggressive environments (23).

4.4.2 Failure mechanism of the PUR foam core

The structural shear behaviour of the one-way sandwich panels under flexural loading is studied using the three-point bending test. One-way sandwich panels with three thickness are tested. The typical load vs deflection curves of C1-1, C2-1, and C3-1 are shown in Figure 4.11. The initial stage of the load vs deflection curves is all linear initially and then the curves enter a nonlinear stage followed by a sudden drop at the failure stage for all test samples. The load vs deflection curves exhibit an obvious yielding point before the peak load. This is due to the large shear deformation of the foam core. Initially, the core is in the elastic stage, but then it enters the plastic stage when the deformation becomes sufficiently large. This leads to the entire sandwich panel having an apparent yielding point in the load vs deflection curves. The average failure loads for C1, C2, and C3 are shown in Figure 4.11(b), with C3 having the highest failure load. The critical failure loads of all test samples are listed in Table 4.7.

Table 4.7 Critical failure load of the samples

Sample ID	Core thickness (mm)	Failure load (N)
C1-1	50	2096
C1-2	50	2013
C1-3	50	2006
C2-1	100	2596
C2-2	100	2545
C2-3	100	2502
C3-1	150	3121
C3-2	150	3115
C3-3	150	2982

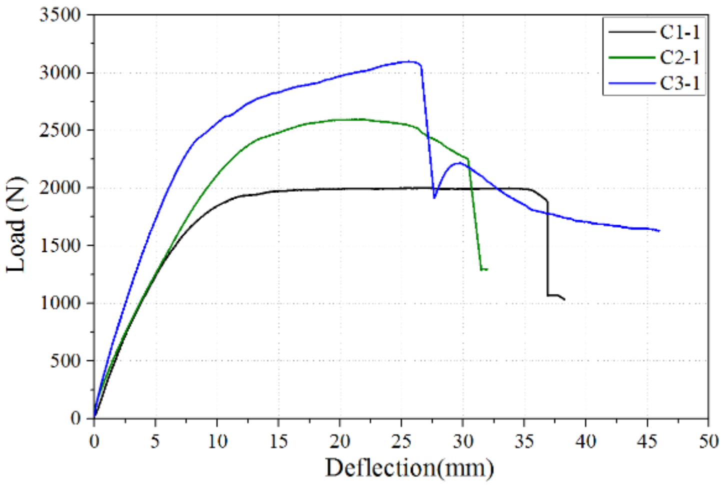

(a)

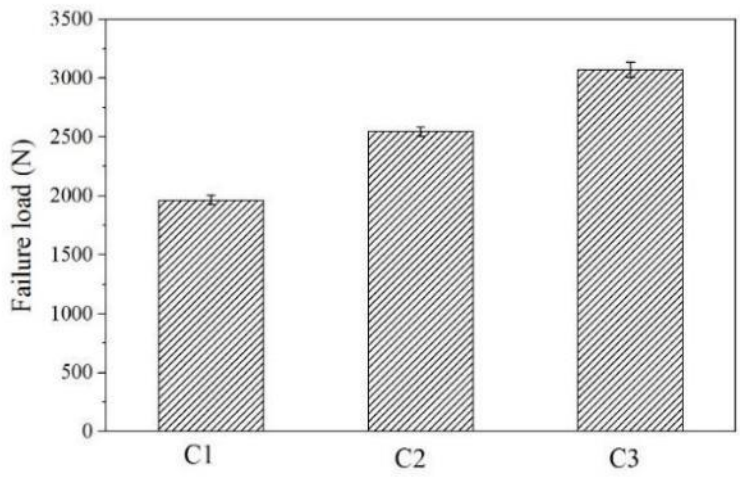

(b)

Figure 4.11 Three-point bending test results: (a) Typical load vs deflection curves of the one-way sandwich panels; (b) Average failure load of the one-way sandwich panels

The failure mode also changes with the increase of the ratio *c/L*. The damage modes of the foam core for C1, C2 and C3 are shown in Figure 4.12. C1 suffers diagonal shear failure of the PUR foam core. However, the diagonal shear crack moves towards the end of the beam and delamination appears when the height of the one-way sandwich panel increases to C2 (c=100 mm). Further increasing the core thickness, the diagonal shear crack disappears and the failure mode changes to the delamination on the top of the beam for C3 (c=150 mm), as shown in Figure 4.12. As given in Table 4.1 and Table 4.2, the shear strength of epoxy is higher than that of PUR foam, therefore delamination damage is not supposed to occur. The observed delamination damage in the test is probably caused because of poor manufacturing quality in gluing the PUR foam core and FRG skin. Significant variation of epoxy bonding strength is also reported in previous tests [29] that debonding between CFRP sheet and concrete is observed at stress significantly smaller than the specified epoxy strength. Therefore, manufacturing quality control is critical to achieve the desired strength and expected failure modes. Another possible solution is to provide some anchorages between FRGC skin and PUR foam, this could be a research topic in the future but is beyond the scope of the present study.

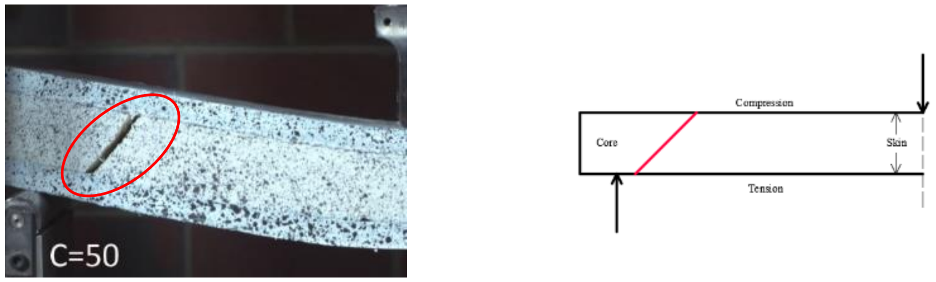

(a)

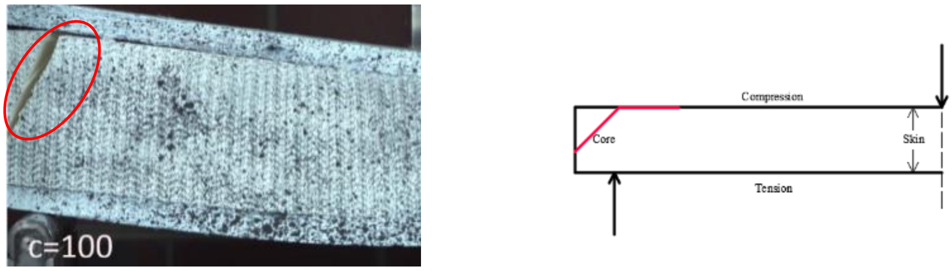

(b)

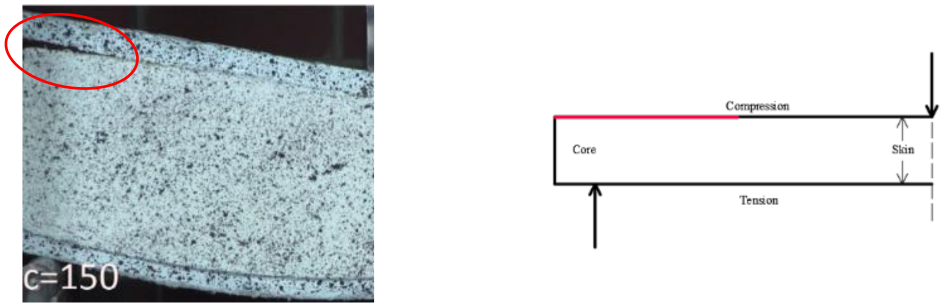

(c)

Figure 4.12 Initiation of shear cracks in the core of one-way sandwich panels with different core heights (unit: mm): (a) C1-1; (b) C2-1; and (c) C3-1

Owing to symmetric characteristics of the system, optical analyses are performed on the left half of the one-way sandwich panel to capture more details about the local strain information. Figure 4.13 shows the full-field shear strain distribution of the panels with different core thicknesses at different levels of loading. The distribution of shear strain for C1-1, C2-1 and C3-1 before delamination is similar. The maximum shear strain appears in the middle part of the PUR foam core layer and the shear strain near the FRGC skin layer is very small. Therefore, the typical distribution of the shear strain for C1-1 and C2-1 shows the occurrence of the diagonal shear crack failure mode. The distribution of the shear strain for C3-1 before delamination is also similar to those in C1-1 and C2-1 as expected. However, when delamination occurred as shown in Figure 4.13 (d), the large shear strain appears on the top part of the PUR foam, which is very close to the top FRG skin layer. This indicates the delamination damage relives the shear stress in the PUR foam core but increases the shear stress along the interface between core and skin owing to stress concentration. The lower shear resistance at the interface might be due to the defect between the PUR foam core and the epoxy resin caused by imperfect manufacture process as discussed above. The large shear stress along the interface is also caused due to the different elastic modulus of the skin layer and the core layer (108). This happens before the shear failure of the PUR foam core for C3 since the thicker core of C3 provided enough resistance for shear failure.

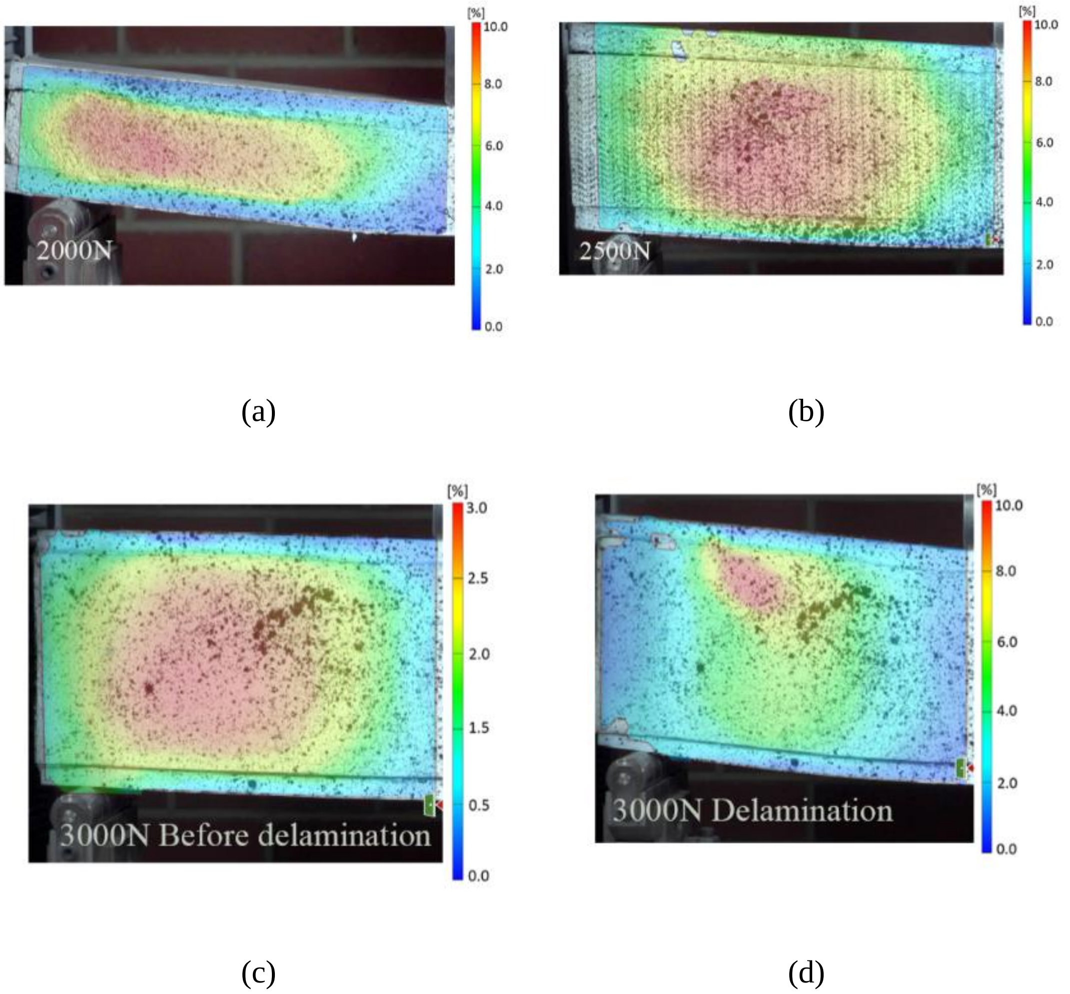

Figure 4.13 Distribution of shear strains on the surface of the PUR: (a) C1-1; (b) C2-1; (c) C3-1 before delamination; (d) C3-1 when delamination occurred

4.4.3 Failure mechanism of the FRG skin

The behaviour of the specially designed one-way sandwich panel is studied using the quasi-static three-point bending test to investigate the tensile failure mechanism of the FRG skin. Samples with three different *t/L* values are studied. The typical flexural failure load vs deflection curves are shown in Figure 4.14(a) and the average failure load is shown in Figure 4.14(b). The critical failure loads of all test samples are listed in Table 4.8. The load vs deflection curves of T1-1, T2-1, and T3-1 show nonlinear behaviour (Figure 4.14(a)). The critical failure loads decrease from T1 to T3 when the span increases from 600 mm to 1000 mm (Figure 4.14(b)). As expected, the deflection for T1-1, T2-1, and T3-1 increases when the span increases from 600 mm to 1000 mm.

Table 4.8 Critical failure load of test samples

Specimen ID	Span (mm)	Failure load (N)
T1-1	600	3200
T1-2	600	3130
T1-3	600	3260
T2-1	800	2400
T2-2	800	2450
T2-3	800	2340
T3-1	1000	1800
T3-2	1000	1870
T3-3	1000	1750

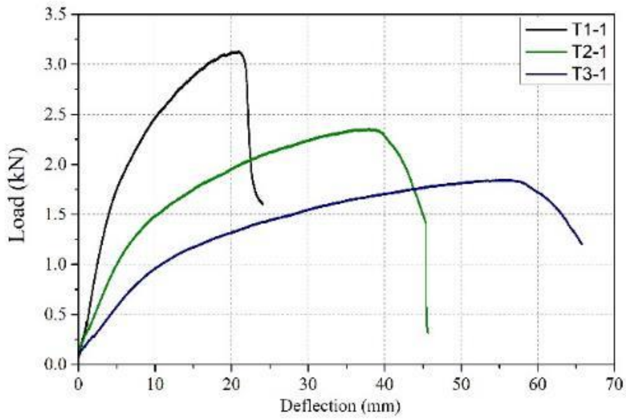

(a)

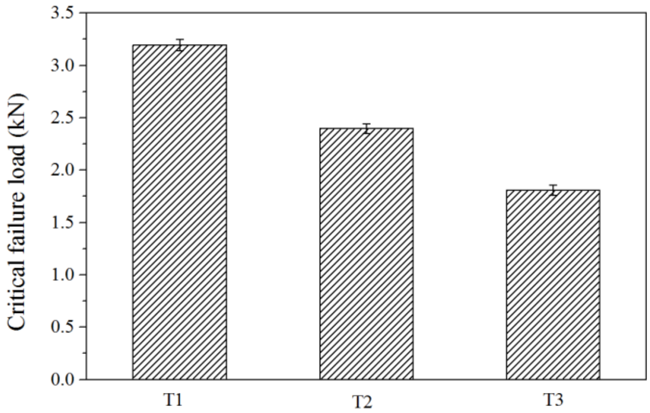

(b)

Figure 4.14 Results of the one-way sandwich panel under three-point bending test: (a) Load vs deflection curves; (b) Average failure load

The failure modes of the T1, T2, and T3 samples are shown in Figure 4.15. It is observed that cracks occurred in the middle part of bottom FRG skin layers. This means that the failure of the whole one-way sandwich panel is because of the tensile failure of the FRG skin. The typical failure state of the bottom FRG skin layer is shown in Figure 4.16. The bottom FRG skin layer has many fine cracks with one major crack located in the middle part. The multiple fine cracks indicate the strain hardening process of the FRG material, which corresponds to the plastic deformation of the developed one-way sandwich panel. The strain fields of the bottom FRG skin layer under the failure state for T1, T2 and T3 are shown in Figure 4.17. The maximum axial strain of the bottom skin layer for T1, T2, and T3 are 4.1%, 3.8%, and 3.5%, respectively, which are similar to the critical failure strain for FRG under the direct tensile test as shown in Figure 4.9. Thus, the failure mode of the T1, T2, and T3 is the skin layer tensile failure because the axial strain in the bottom skin layer exceeds the maximum strain of FRG under tension.

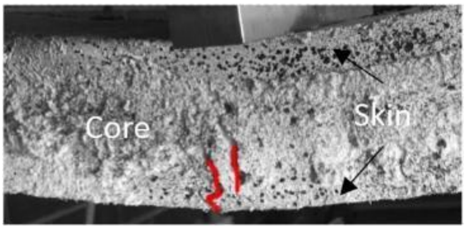

(a)

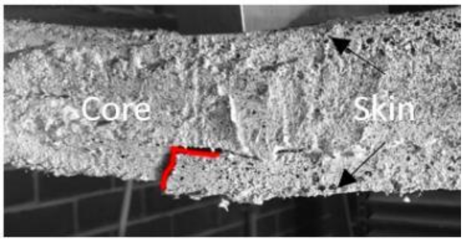

(b)

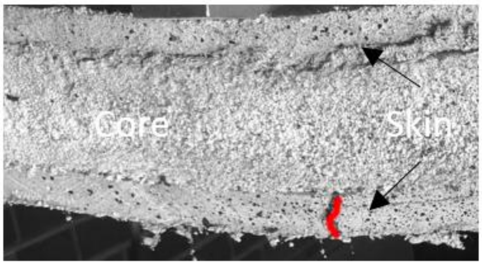

(c)

Figure 4.15 Failure modes under the three-point bending test: (a) T1-1; (b) T2-1; (c) T3-1

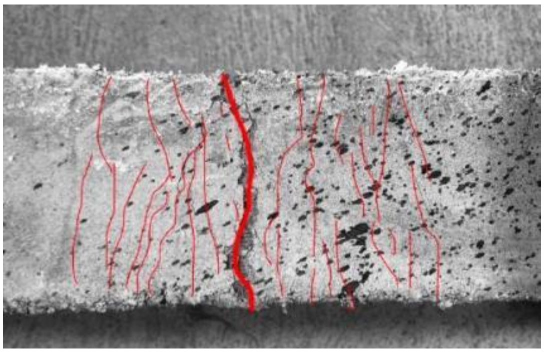

Figure 4.16 Multiple cracks of the bottom FRG skin

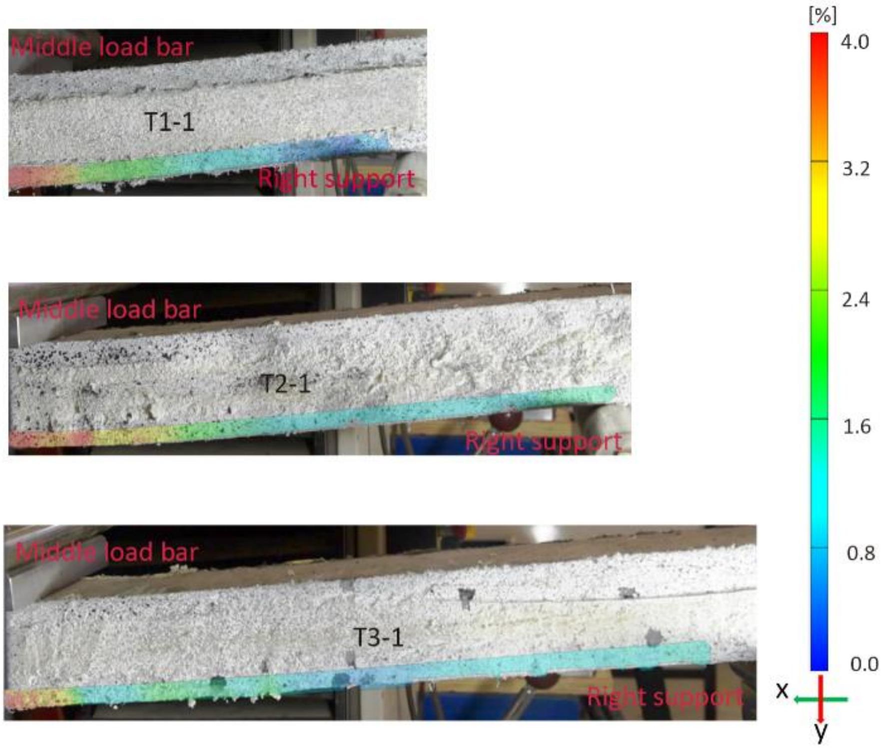

Figure 4.17 Axial strain fields along the *x*-direction of the bottom FRG skin layers for T1-1, T2-1, and T3-1

4.4.4 Theoretical analysis of sandwich panel under flexural loading

The developed one-way sandwich panel with FRG skin and PUR foam core is a simple supported one-way sandwich panel with the total span L and uniform width b under three-point bending (Figure 4.18). The thickness of the two FRG skin layers is set as t, separated by a PUR foam core with the thickness of c. The overall depth of the one-way sandwich panel is h and the width is b. The distance between the midplanes of the top skin layer and bottom skin layer is *d*. Several failure modes could occur in the sandwich panel because of the complex combination of the behaviour of the skin and foam core based on previous studies (90-92), as shown in Figure 4.19. Failure could occur under flexural loads, which include one of the following failure modes: (a) skin failure, (b) skin indentation, and (c) shear failure of the core.

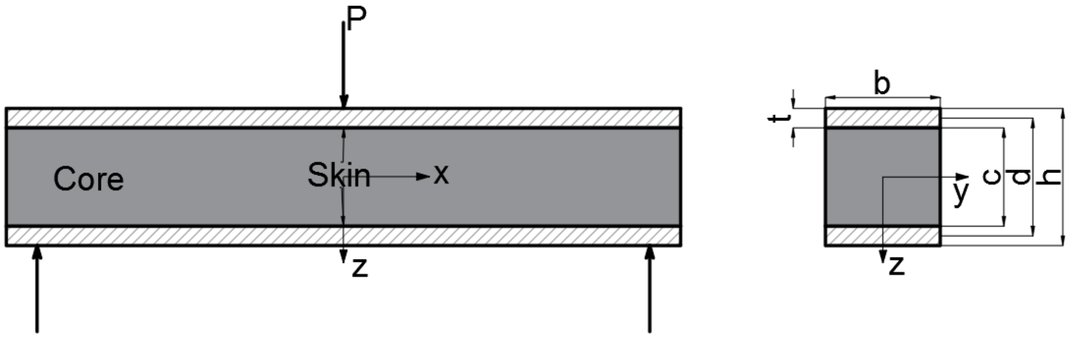

Figure 4.18 Dimension notations of the one-way sandwich panel

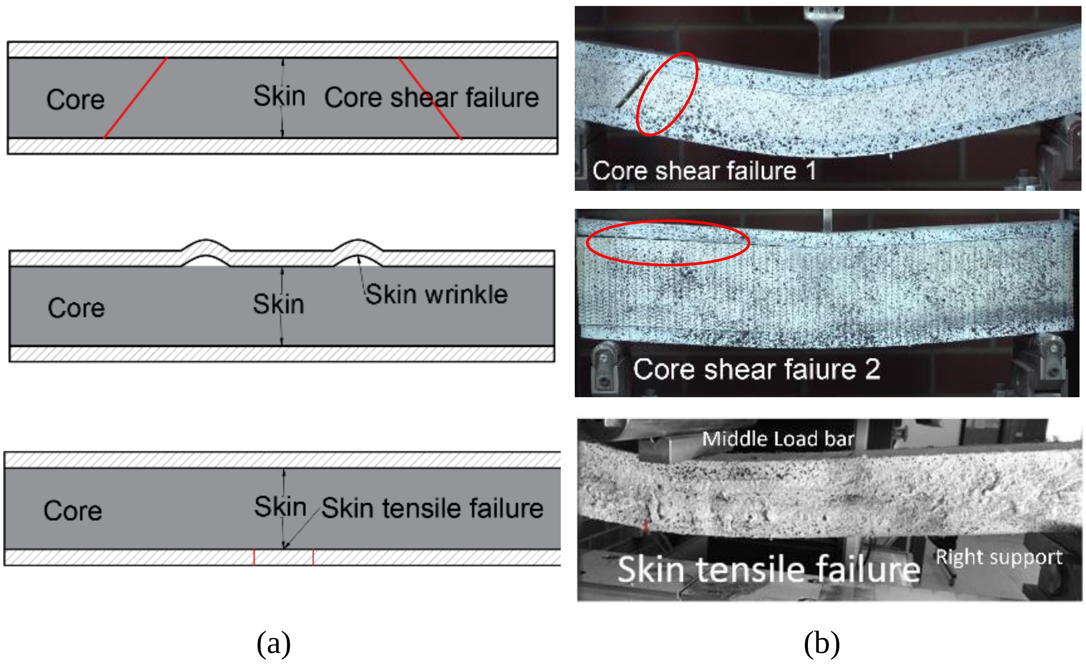

Figure 4.19 Failure modes for the one-way sandwich panel under flexural loading test: (a) Possible failure mode; (b) Real failure mode during the test

Since the developed one-way sandwich panels use relatively thick FRG skin layers, no skin winkle is observed in the tests because the skins had adequate out-of-plane stiffness, instead, skin delamination is observed. Therefore, the failure modes of the developed one-way sandwich panel under flexural loading, as observed above, include the shear failure of the core, the tensile failure of the skin layer, and the skin delamination from the core. Both the diagonal shear failure of PUR foam core and the delamination failure of the skin can be categorized as shear failure. Considering these three possible failure modes, the critical failure load P_{cr} of the beam can be expressed as

$$P_{cr} = min(P_{c1}, P_{c2}, P_{c3}) \tag{4.2}$$

where P_{c1} is the critical failure load for diagonal shear failure, P_{c2} is the critical failure load for delamination shear failure, and P_{c3} is the critical failure load for skin tensile failure. Thus, analytical models to calculate P_{c1}, P_{c2}, and P_{c3} are derived to predict the critical failure load of these two failure modes for the developed sandwich panel. As discussed above since the bonding strength at the interface between FRG skin and PUR foam core, i.e., the epoxy strength provided by the supplier, is larger than the shear strength of PUR foam core, delamination is not expected to occur. The observed delamination damage is caused most probably because of the inadequate bonding owing to poor manufacturing quality, which unfortunately cannot be predicted because the quantitative bonding strength is not available. For completeness, P_{c2} is also derived as a critical failure load in the study.

4.4.4.1 Diagonal shear failure (P_{c1})

The one-way sandwich panel is assumed to be bonded perfectly and there is no relative movement between the different layers. The transverse shear stress of the section in the one-way sandwich panel is shown in Figure 4.20.

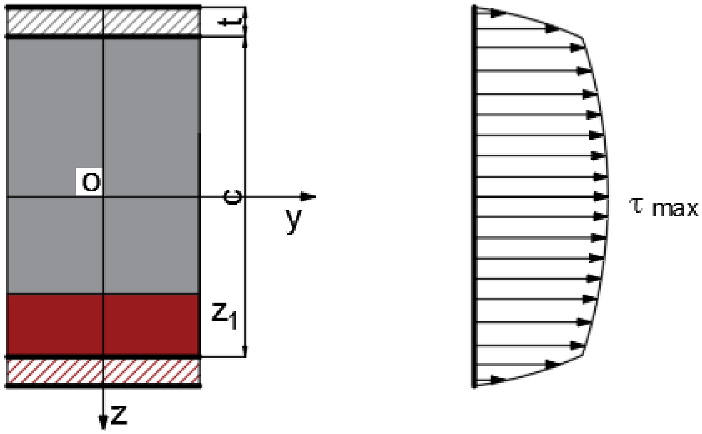

Figure 4.20 The transverse shear stress in the foam core of the one-way sandwich panels

According to Timoshenko Beam theory, the sections remain plane and perpendicular to the longitudinal axis and the shear stress of the cross-section of the beam can be expressed as:

$$\tau = \frac{V \cdot Q}{I \cdot b} = \frac{P \cdot Q}{2 \cdot I \cdot b} \tag{4.3}$$

where V is the shear force, Q is the first moment of the area, I is the second moment of area of the entire section about the centroid, b is the width of the section and P is the applied force for three point bending test. The neutral axis is located at the middle of the section, and the Eq. (4.3) is modified to consider different materials as the follows:

$$\tau = \frac{P \cdot \sum(QE)}{2 \cdot D \cdot b} \tag{4.4}$$

where D is the flexural rigidity of the entire section. $\sum(QE)$ represents the sum of Q and E of all the parts of the section. The flexural rigidity can be calculated considering the different parts of the section:

$$D = \frac{E_f \cdot b \cdot t^3}{6} + \frac{E_f \cdot b \cdot t \cdot (c+t)^2}{2} + \frac{E_c \cdot b \cdot c^3}{12} \tag{4.5}$$

where E_f is the elastic modulus of FRGC skin layer, and E_c is the elastic modulus of PUR foam core. The (QE) can be determined according to the position of z:

$$\begin{cases}(QE) = E_f \cdot b \cdot \frac{(c \cdot t + t^2)}{2} + \frac{E_c \cdot b}{2} \cdot \left(\frac{c^2}{4} - z^2\right) & (0 < z \leq \frac{c}{2}) \\ (QE) = \frac{E_f \cdot b}{2} \cdot \left(\frac{(c+2t)^2}{4} - z^2\right) & (\frac{c}{2} < z \leq \frac{c+t}{2})\end{cases} \tag{4.6}$$

Therefore, the traverse shear stress in the sandwich beam can be driven as:

$$\begin{cases}\tau = m \cdot P \cdot \left[4 \cdot E_f \cdot (c \cdot t + t^2) + E_c \cdot (c^2 - 4 \cdot z^2) \quad (0 \leq z \leq \frac{c}{2})\right] \\ \tau = m \cdot P \cdot E_f[(c + 2 \cdot t)^2 - 4 \cdot z^2] \quad (\frac{c}{2} < z \leq \frac{c+t}{2})\end{cases} \tag{4.7}$$

where m can be expressed as:

$$m = \frac{3}{8 \cdot E_f \cdot [t^3 + 3 \cdot t \cdot (c+t)^2] + 4 \cdot E_c \cdot c^3} \tag{4.8}$$

The shear stress distribution is shown in Figure 4.20. The maximum shear stress happens at the centre of the cross-section ($z=0$), and therefore the critical failure load (P_{c1}) with the shear failure of PUR foam can be estimated as

$$P_{c1} = \frac{4E' \cdot c^3 + 8 \cdot (3c^2 \cdot t + 4 \cdot t^3 + 6 \cdot c \cdot t^2)}{3E' \cdot c^2 + 12(c \cdot t + t^2)} \tau_c b \tag{4.9}$$

where τ_c is the shear strength of the PUR foam core; and $E' = E_c/E_f$.

4.4.4.2 Delamination failure (P_{c2})

The delamination happens when shear stress in the longitudinal direction along the interface of the skin layer and the core layer is larger than the material shear strength. The shear stress in the longitudinal direction can be analysed as shown in Figure 4.21.

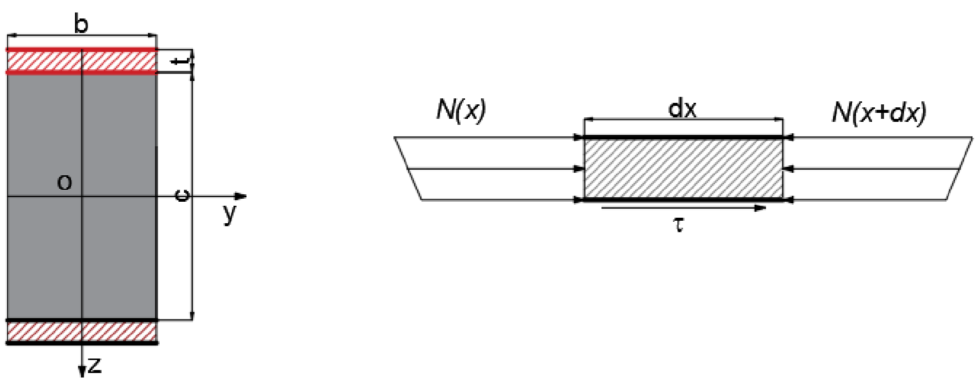

Figure 4.21 Section analysis of the delamination shear failure

The force equilibrium on selected segment can be expressed as follows:

$$\int N(x)dA + \tau b dx = \int N(x + dx)dA \tag{4.10}$$

where τ is the shear stress, *N(x)* and *N(x+dx)* are the axial force in the longitudinal direction. Thus, the shear stress can be calculated by the following equation:

$$\tau = \frac{V \cdot Q_1}{I \cdot b} = \frac{P \cdot Q_1 E_f}{2 \cdot D \cdot b} \tag{4.11}$$

where Q_1 is the first moment of the selected area, and it can be expressed as the following equation:

$$Q_1 = \frac{1}{2} \cdot b \cdot t \cdot (c + t) \tag{4.12}$$

Thus, the critical failure load can be given based on Eq. (4.5), (4.11) and (4.12), which is given below:

$$P_{c2} = \frac{2 \cdot (4 \cdot t^3 + 6 \cdot c \cdot t^2 + 3 \cdot c^2 \cdot t) + E_c \cdot c^3}{3 \cdot t(c+t)} \cdot \tau_c \cdot b \tag{4.13}$$

where τ_e is the shear strength of epoxy. Since τ_e is much larger than t_c for the materials used in this study, P_{c2} (21kN) predicted by Eq. (4.13) is much larger than the experimental study result (3.0 kN), it is not used in the study for failure load prediction. The results from Allen's model (109), the presented model (P_{c1} and P_{c2}) and experimental tests are shown in Figure 4.22 for comparison. It can be observed that the presented model is accurate to predict the critical failure load for C1 and C2. However, the test results for C3 is much smaller than predicted critical load P_{c1}. Some defects might exist when bonding PUR foam core and FRG skin layer with epoxy as discussed above.

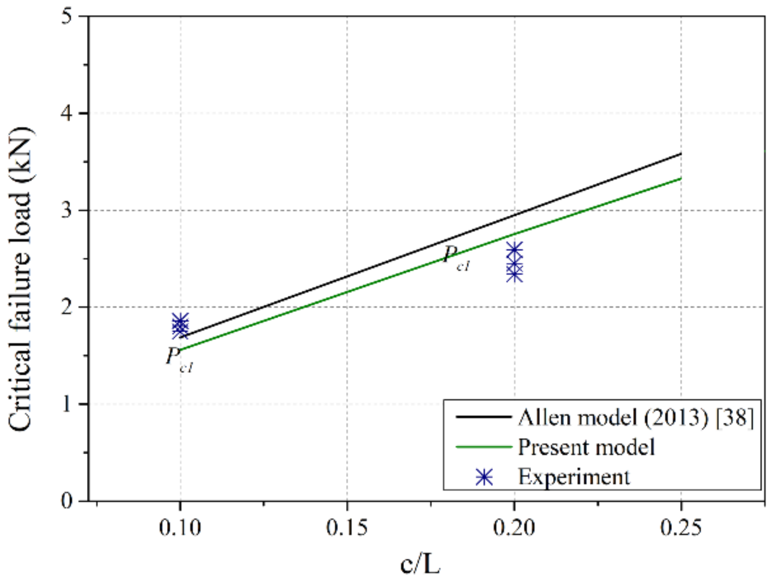

Figure 4.22 Comparison of critical failure load for experimental and theoretical predictions

4.4.4.2 Tensile failure of the skin (P_{c3})

The skin layer fails when the maximum external force exceeds the internal axial strength in the skin layer. The axial stress can be calculated as

$$\sigma_f^t = \frac{M \cdot E_f}{D} \cdot z \tag{4.14}$$

where σ_f^t is the stress in the skin layer, D is the stiffness of the sandwich panel and E_f is the elastic modulus of skin layer. Since the neutral axis is at the middle of the section, the maximum stress is obtained at the distance $h/2$ from the neutral axis, and the critical failure load for the skin layer tensile failure can be given by

$$P_{c3} = \frac{8 \cdot D}{E_f \cdot L \cdot (\mathrm{c}+2 \cdot \mathrm{t})} \cdot \sigma_{yt} \tag{4.15}$$

where σ_{yt} is the tensile strength in the skin layer. The strain and stress distribution of the cross section of the developed sandwich panel can be assumed as shown in Figure 4.23. The critical failure load for the skin tensile failure mode can be expressed as

$$P_{c3} = [4 \cdot t^3 + 12 \cdot t \cdot (c+t)^2 + 2 \cdot E' \cdot c^3] \cdot \frac{\sigma_{yt} \cdot b}{3 \cdot (c+2 \cdot t) \cdot L} \tag{4.16}$$

where $E' = E_c/E_f$. Based on the selected material for skin and core, the modulus of the skin layer can be assumed to be much lager than that of core, that is $E' = E_c/E_f \approx 0$. Therefore, Eq. (4.16) leads to:

$$P_{c3} = \frac{[4 \cdot t^3 + 12 \cdot t \cdot (c+t)^2]}{3 \cdot (c+2 \cdot t) \cdot L} \cdot b \cdot \sigma_{yt} \tag{4.17}$$

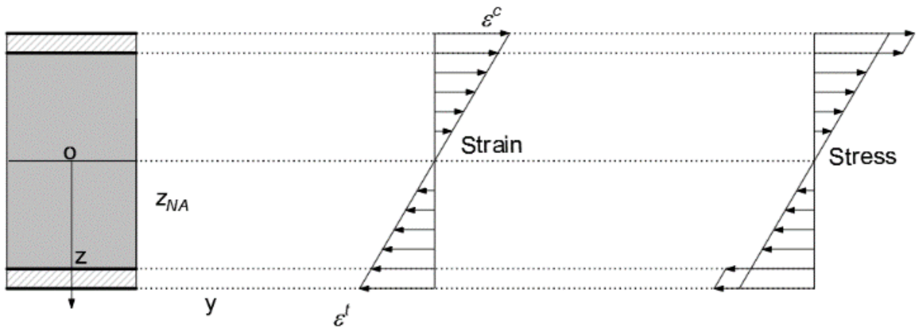

Figure 4.23 Schematic sectional diagram of internal force distribution of one-way sandwich panel (for the tensile failure mode of skin layer)

The calculation in Eq. (4.16), the results from the modified Gibson's model (110) and experimental tests are shown in Figure 4.24. Good match between the results from experimental tests and the presented model is observed. It can be seen that the prediction of the present model can predict the experimental result well with a little overestimation. This is because the present derivation is based on linear elastic response assumption, while certain level of nonlinear response occurred in the test as shown in Figure 4.14 (a). The modified Gibson's model might under-predict results as compared to the experimental results.

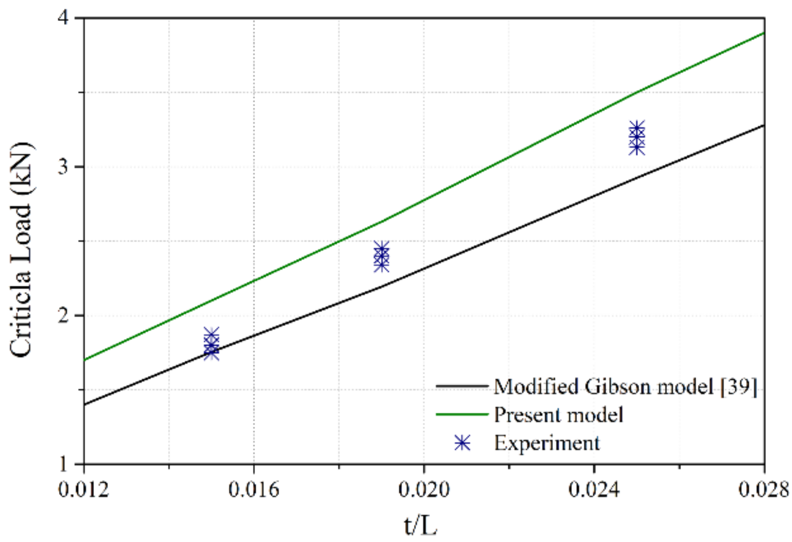

Figure 4.24 Comparison of critical failure loads for experimental and theoretical predictions

4.5 Results and discussions of the edgewise compressive loading

4.5.1 Edgewise compressive test of sandwich panels

The typical load and axial displacement responses along the *Y* direction (shown in Figure 4.8) of the developed sandwich panel under quasi-static edgewise compressive loading are shown in Figure 4.25. Three repeated tests are conducted for each test group listed in Table 4.5. The average critical failure load for the tested sandwich panel is also shown in Figure 4.25 (b) and the critical failure load for all specimens are listed in Table 4.9. The width of the sandwich panel is kept at 200 mm and the thickness of the sandwich panel is kept at 180 mm. The failure load for the critical collapse decreased from 210 kN to 145 kN when the height increases from 200 mm to 600 mm. Therefore, the load capacity of the sandwich panel degrades when the height increases. The stiffness of G3 is smaller than that of G1 and G2, and the maximum deflection for G3 is the highest. The collapse process for G3 is much slower than that of G1 and G2. In addition, G3 has a softening stage, but the load vs deflection curves of G1 and G2 directly drops. The reason for this could be because the failure mode for G3 is from the global buckling of the sandwich panels when the height of the sandwich panel increases; however, the failure modes for G1 and G2 are only the FRG material failure. The failure load of G2 is slightly smaller than that of G1 because of some structural and specimen size effect. As will be discussed, the tested G2 specimen also shows a slight lateral displacement, indicating some bending deformation under axial load. The secondary bending deformation of the G2 specimen is, however, small, therefore the damage is still governed by the failure of the skin material.

Table 4.9 Critical failure load for all specimens

Specimen ID	length (mm)	Failure load (kN)
G1-1	200	210.5
G1-2	200	205.4
G1-3	200	214.6
G2-1	400	200.3
G2-2	400	194.5
G2-3	400	198.6
G3-1	600	144.6
G3-2	600	142.5
G3-3	600	149.0

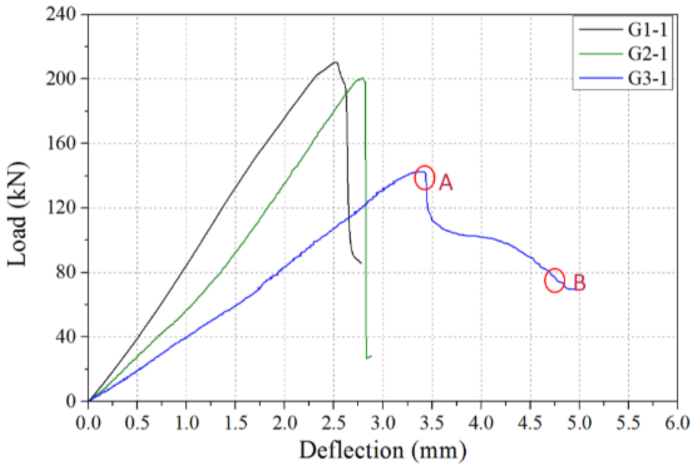

(a)

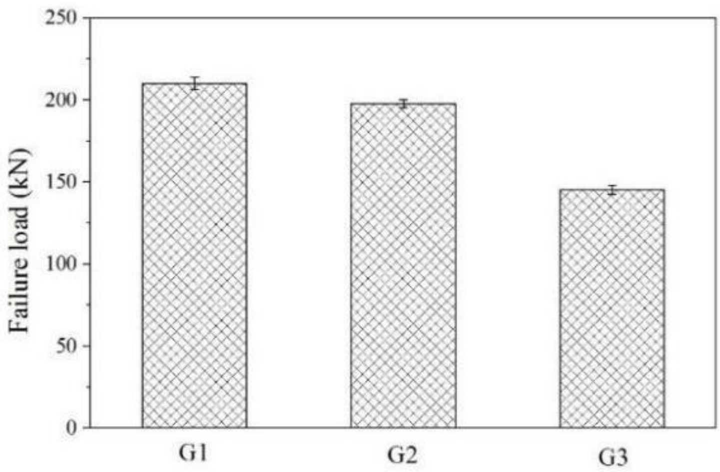

(b)

Figure 4.25 Edgewise compressive test results: (a) Typical load vs deflection curve; (b) Average critical failure load

For the sandwich panels under the edgewise compressive load, the failure modes were quite complex. Several failure modes have been reported and verified by experimental studies (93, 111-113). Various failure modes were observed because of the influence of different skins, core materials, and geometry sizes (93). Cote et al. (94) summarised several failure modes of sandwich panels under the edgewise direction compressive load, which included Euler elastic macro buckling, Euler type macro plastic buckling, macro elastic core shear buckling, elastic face wrinkling, and plastic face wrinkling. The possible failure mode of the developed sandwich panel is affected by the geometries of the sandwich panels. The failure modes of the sandwich panel under the compressive load are shown in Figure 4.26. The width and thickness of G1, G2, and G3 are kept at 200 mm and 180 mm, respectively. As shown in Figure 4.26, a crack is observed on one side of the skin when the load reached the critical failure load for the specimen G1-1. A similar failure mode is found for the G2-1 sample with a crack also appearing on one side of the skin, the damage occurred on the skin only. This is because the stiffness of the skin is substantially larger than that of the PUR foam core, in an order of 1000 times, the axial load is therefore primarily resisted by the skin and the contribution from the core to resisting the axial load is minimum. The function of foam core here is mainly providing some lateral constraint to resist buckling of the skin. However, increasing the height of the specimen, buckling of the specimen occurs, as shown in the figure of the failure mode of G3-1 (Figure 4.26). The

G3-1 sample buckles when the load reaches the critical failure load and then the delamination between the geopolymer skin and foam core is observed. Finally, the foam core is fractured and a big crack is observed in the middle of the foam core as shown in Figure 4.26. This phenomenon indicates that the failure mode of the sandwich panel is the local fracture of the FRG skin when the height of the sandwich panel is small, for example, G1 and G2. However, the failure mode changes to global buckling when the height becomes sufficiently larger, e.g. G3.

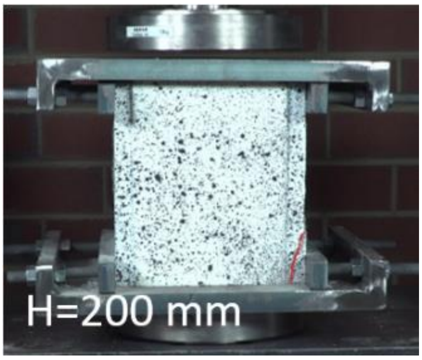

(a)

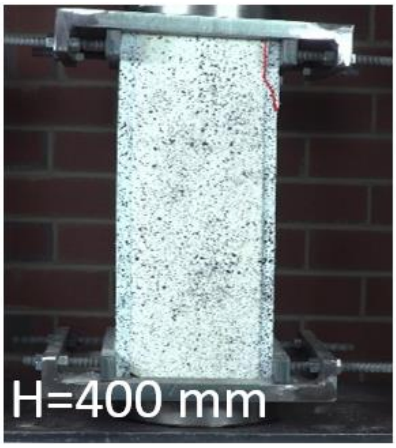

(b)

(c)

Figure 4.26 Failure modes for the edgewise compressive test: (a) G1; (b) G2: (c) G3

Global buckling also induces out-of-plane displacement, and the out-of-plane displacement in turn could exacerbate the buckling effect. The out-of-plane displacements along *X* direction (shown in Figure 4.8) of G1-1, G2-1 and G3-1 are examined by using the DIC method, as shown in Figure 4.27. As can be seen in Figure 4.27, the out-of-plane displacements along *X* direction for G1-1 and G2-1 are very small. The maximum out-of-plane displacements for G1-1 and G2-1 are around 0.4 mm and 1 mm under the critical failure load of 210 kN and 200 kN, respectively. However, the maximum out-of-plane displacement for G3 is 25 mm under the load of 78 kN (shown in Figure 4.27 (a)), which is the load before the final failure of the sandwich panel. Besides, the distribution of out-of-plane displacement for G1-1 is relatively uniform along with the height of the specimen, which means buckling effect barely appears, and the behaviour of the specimen is governed by the material properties under the axial loading. However, the out-of-plane displacement of G2-1 in the middle part is larger than these near the top and bottom part, even if the overall out-of-plane displacement is relatively small, and the damage is due to the material failure of FRGC. This secondary lateral deformation of the specimen results in the slightly smaller axial loading capacity of G2-1 as compared to G1-1. For the case of G3-1, the middle part of the specimen has substantial out-of-plane displacements under the loads of 146 kN and 78 kN (points A and B in Figure 4.25 (a)), while the top and bottom ends have smaller out-of-plane displacement. This indicates when the height increases to a certain extent to the thickness of the specimen, the global buckling becomes obvious for the developed sandwich panel.

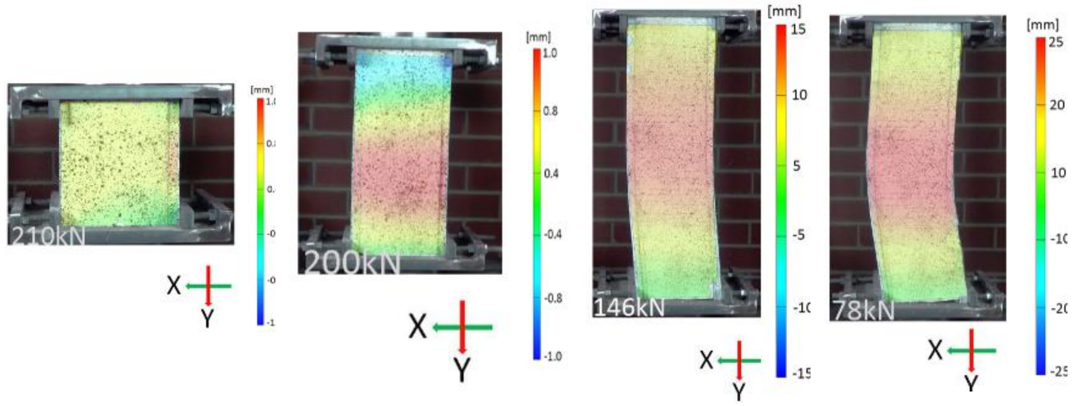

(a) (b) (c) (d)

Figure 4.27 *X*-direciton displacement distribution: (a) G1-1; (b) G2-1; (c) G3-1 (Point A in Figure 4.25 (a)); (d) G3-1 (Point B in Figure 4.25 (a))

4.5.2 Theoretical analysis under edgewise compressive loading

For the sandwich panel developed in the present study under edgewise compressive loading, the failure modes might be the compressive failure of material (P'_{c1}), the shear failure of material under compressive load (P'_{c2}), and global buckling (P'_{c3}). Figure 4.28 shows the schematic diagram of the developed sandwich panel undergoing a uniform compressive load. *H* is the length of the developed sandwich panel between the top and bottom clamps. Other parameters are the same as shown in Figure 4.18. The critical failure load for the developed sandwich panel under edgewise compressive loading can be calculated by the following equation:

$$P'_{cr} = min(P'_{c1}, P'_{c2}, P'_{c3}) \tag{4.18}$$

where P'_{cr} is the critical failure load for sandwich panel under edgewise compressive load. P'_{c1}, P'_{c2}, and P'_{c3} are the critical load under different failure mode mentioned above.

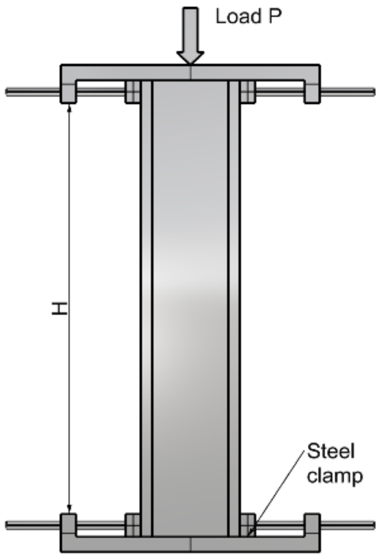

Figure 4.28 Schematic diagram of the sandwich panel under edgewise compressive load

The compressive failure of material might happen if the compressive load is larger than the resistance material can provide. The force equilibrium is shown in Figure 4.29 by the following equation:

$$2P_s + P_c = P \tag{4.19}$$

where P is the compressive load, P_s is the resistance of FRGC skin layer, and P_c is the resistance of PUR foam layer.

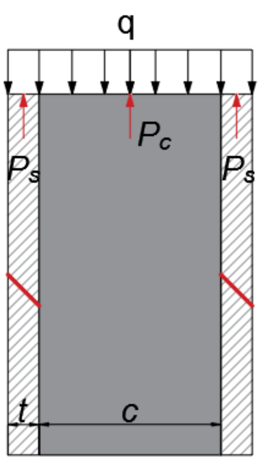

Figure 4.29 The Schematic sectional diagram

The materials are assumed to be elastic, so the following equation can be derived:

$$\frac{P_s \cdot H}{E_f \cdot A_f} = \frac{P_c \cdot H}{E_c \cdot A_c} \tag{4.20}$$

where E_f and E_c are the elastic modulus of FRG skin and PUR foam, A_f and A_c are area of skin layer and core layer, shown in Figure 4.29. Thus, the critical failure load for compressive failure of material can be driven as the following equation:

$$P'_{c1} = (2 \cdot t + E' \cdot c) \cdot \sigma_f^c \cdot b \tag{4.21}$$

where $E' = E_c/E_f$, and σ_f^c is the compressive strength of FRG.

Another possible failure mode for the developed sandwich panel under compressive load is the FRG skin shear failure, as shown in Figure 4.29. The largest shear stress for component under axial loading can be expressed as:

$$\tau_{max} = \frac{\sigma}{2} \tag{4.22}$$

where τ_{max} is the largest shear stress. Thus, the critical failure load P'_{c2} can be calculated by the following equation:

$$P'_{c2} = (4 \cdot t + 2 \cdot E' \cdot c) \cdot \tau_{max} \cdot b = (4 \cdot t + 2 \cdot E' \cdot c) \cdot \tau_f \cdot b \tag{4.23}$$

where τ_f is the shear strength of the FRG skin layer. According to Ref (114), the value of τ_f can be estimated by the compressive strength of fibre reinforced concrete:

$$\tau_f = 0.72 \cdot f_c^{0.8} + 0.08 \cdot V_f \cdot (L/d) \tag{4.24}$$

where f_c is the compressive strength of fiber reinforced concrete, V_f is the volume fraction of fiber content, and (*L/d*) is the aspect ratio.

The last possible failure mode is the global buckling of the developed sandwich panel. According to Euler buckling formula, the critical failure load P_E can be calculated by the following equation (93):

$$P'_E = \frac{k^2 \cdot \pi^2 \cdot (EI)_{eq}}{H^2} \tag{4.25}$$

where *E* and *I* are the equivalent elastic modulus and the moment of inertia, respectively. *k* is a dimensional factor, which depends on the rotational stiffness of the end node. The value of *k* can be taken as 2 when the end nodes are clamped based on previous studies (93, 115).

The buckling of the sandwich panel includes two different modes. One was Euler buckling and the other was core shear buckling. The critical failure load P_c for the core shear buckling can be calculated by the following equation (109):

$$P_c' = G_c \frac{b \cdot (c+t)^2}{c} \tag{4.26}$$

where G_c is the shear modulus of the PUR foam core. b, c and t are shown in Figure 4.18.

For the developed sandwich structure with FRG as skin layer, the out-of-plane stiffness of two skins bending about their separate centroid axis might restrict the extent of the secondary displacement. The effect of the out-of-plane stiffness of the skins must be considered, so according to the previous study (109), the Euler buckling load P_f' for two skins can be expressed as:

$$P_f' = \frac{k^2 \cdot (EI)_s}{H^2} \tag{4.27}$$

where the subscript s represents the flexural stiffness of skins. Then, the critical failure load can be calculated by the following equation (109):

$$P_{c3}' = P_E' \cdot \left(\frac{1 + P_f'/P_c' - (P_f'/P_c') \cdot (P_f'/P_E')}{1 + P_E'/P_c' - P_E'/P_c'} \right) \tag{4.28}$$

where P_{c3}' is the critical failure load; P_E', P_c' and P_f' are calculated by Eq. (4.25), (4.27) and (4.28), respectively.

The predicted critical failure loads and experimental results are shown in Figure 4.30. The predicted value of P_{c2}' is very close to the failure load for G1 and G2. It also reflects the failure mode for the test samples G1 and G2 is the material shear failure under the edgewise compressive loading. The prediction of P_{c3} is similar to that of the experimental results of C3, with the discrepancy of 13%. It also confirms G3 has a global buckling failure mode.

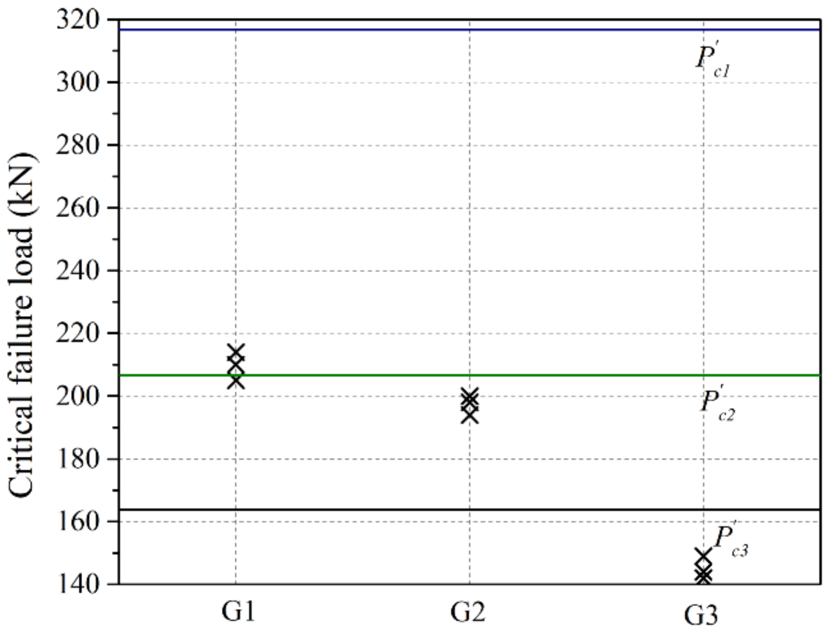

Figure 4.30 Critical failure load for G1, G2, and G3

4.6 Summary

In the present study, a new type of lightweight sandwich panel for prefabricated buildings is developed. This panel is made of FRG composite skin layers and a PUR foam core. The behaviours of the developed lightweight sandwich panel under flexural loading and edgewise compressive loading are studied. The DIC technique is used in the test for full-field measurement of displacements and strains. The failure mechanisms of the developed sandwich panels, including core shear failure and skin layer tensile failure, are studied by conducting quasi-static three-point bending test. Analytical models are also derived to predict the critical failure loads of the developed one-way sandwich panel under flexural loading. In addition, the failure mechanism of the developed sandwich panel under edgewise compressive load is studied, followed by analytical studies. The main conclusions are given below:

1. FRG material exhibits good deflection hardening behaviour, which is beneficial for the load-bearing capacity and energy absorption capacity.
2. The failure mode of the developed sandwich panel with PUR foam core P1 (35 kg/m^3) under flexural loading transforms from the shear failure of PUR foam

core to the delamination between the FRG skin and PUR foam core, when the thickness-to-span ratio increases from 0.1 (C1) to 0.3 (C3).

3. The developed sandwich panel with PUR foam core P2 (96 kg/m3) under flexural loading experiences the tensile failure of the FRG skin layer when the ratio t/L is 0.015, 0.018 and 0.025.
4. The analytical models for predicting the critical failure load for the shear failure of PUR foam core and the tensile failure of the FRG skin layer are proposed and give accurate predictions of the experimental results.
5. The failure mechanisms for the developed sandwich structures with different thickness-to-length ratios under edgewise compressive loading are different. The failure mode changes from material failure of the FRGC skin to global buckling when the thickness-to-length ratio reduces from 0.90 (G1) to 0.30 (G3). The analytical models for predicting the critical failure load under edgewise compressive load are proposed and give reasonable predictions of the experimental results.

5 Structural performance and vibration characteristics of the full-size structural sandwich panel

5.1 Introduction

Typical sandwich panels are composed of three layers that include two thin stiff skin layers and a layer of low-density material as core that is usually made of lightweight materials, such as EPS foam or PUR foam. The sandwich panel developed in the present study used FRG as the skin layer and PUR foam as the core layer. The structural performance and vibration characteristics of the full-size sandwich panel were studied in this chapter. Firstly, the structural performance of two types of structural sandwich panels were investigated and discussed through laboratory tests on full scale specimens. The first type (S1) is a sandwich panel applying FRG as the skin and PUR foam as the core. The second type (S2) is originated from the first type (S1) and strengthened by a BFRP sheet on the back FRG skin. Structural behaviours of the two types of sandwich panels (S1 and S2) are studied by conducting quasi-static four-point bending tests and axial compressive tests.

Vibration characteristics of two sandwich panel (S1 and S2) are studied. Modal vibration response measurements under hammer impact excitations can be used to obtain the dynamic characteristics of the structural system, including natural frequencies, mode shapes and damping ratios. The hammer impact vibration test is one of the most widely adopted excitation methods for modal tests. With vibration testing measurements, many system identification methods have been developed for extracting vibration characteristics, such as natural frequencies, mode shapes and damping ratios, based on either input/output identification methods or the output only identification methods. The output only frequency-domain decomposition (FDD) method is an effective and efficient way for identifying modal parameters of the structural system. In engineering practices, accurate mathematical models representing true dynamic vibration characteristics of structural systems are required for modern structural design, analysis, and assessment. Finite element analysis is an effective and efficient mathematical analysis method. In this chapter, finite element models are built to represent these two types of developed sandwich panels and the obtained numerical dynamic vibration properties of these two panels are compared with the testing results.

5.2 Experimental program

5.2.1 Material and manufacture process for sandwich panels

The same mixture design of FRG is used as that in Chapter 4 and PUR foam with a density of 35 kg/m^3, which is commonly applied as insulation material and is commercially available, is used to prepare the sandwich panel. The properties of the FRG and PUR foam can be found in Table 4.6 and Table 4.1, respectively. The properties of the applied epoxy resin are given in Table 4.2. The manufacturing process of the developed structural lightweight sandwich panel involves two phases: (1) casting the FRG to form the top and bottom skin layer for the developed sandwich panel; and (2) assembling the bottom skin layer, core layer, and top skin layer to form the entire sandwich panel. The dimensions of the developed sandwich panel are 2400 × 600 × 180 mm (length × width × height) and the thicknesses of the skin layer and core layer are 15 mm and 150 mm, respectively. The detailed manufacture process for S1 is presented in Chapter 4, which is also shown in Figure 5.1. The only difference between S2 and S1 is that basalt fibre sheet was attached to the surface of the bottom FRG skin of S2 to enhance the load-carrying capacity and prevent the flexural failure of bottom FRG skin. The manufacture process for the C1 specimens for axial compressive test is the same as that for S1.

(a)

(b)

(c)

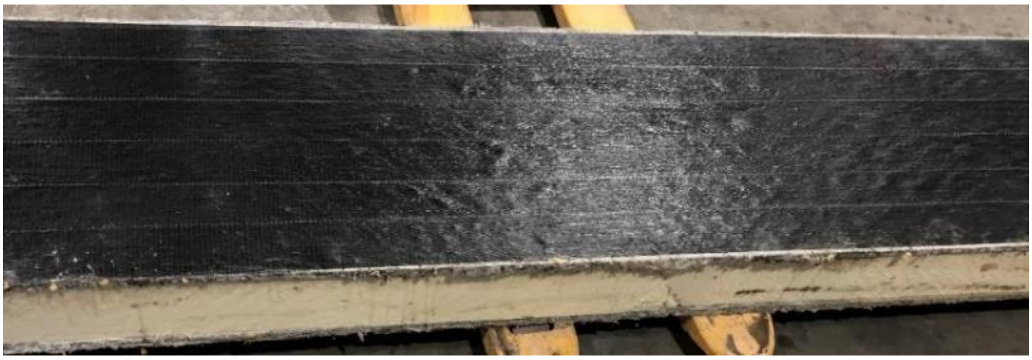

(d)

Figure 5.1 Production process of the developed sandwich panel: (a) Mould; (b) FGR skin; (c) S1; (d) S2

BFRP sheets have been applied to strengthen reinforced concrete beams owing to its high tensile strength (101). In this study, unidirectional basalt fibre sheet with a width of 100 mm and a density of 300 g/m^2 is used as the external reinforcement to the skin layer of the sandwich panel. The properties of the applied BFRP sheet are given in Table 5.1. The dust was removed with a pressurised air hose and the surface of the FRG bottom skin was cleaned with acetone followed by the application of primer to the surface of the FRG skin. The wet layup method was used to bond the BFRP sheet onto the FRG layer. The width of the entire sandwich panel is 600 mm, with six BFRP strips (100 mm width per strip) used for one layer. A total of two layers of BFRP sheets are applied to reinforce the back FRG skin. The details of S1 and S2 are shown Figure 5.2.

Table 5.1 Properties of BFRP sheet

Parameter	300 *g/m^2* BFRP sheet
Width (mm)	100
Nominal thickness (mm)	0.12
Tensile strength (MPa)	1684
Tensile modulus (GPa)	77

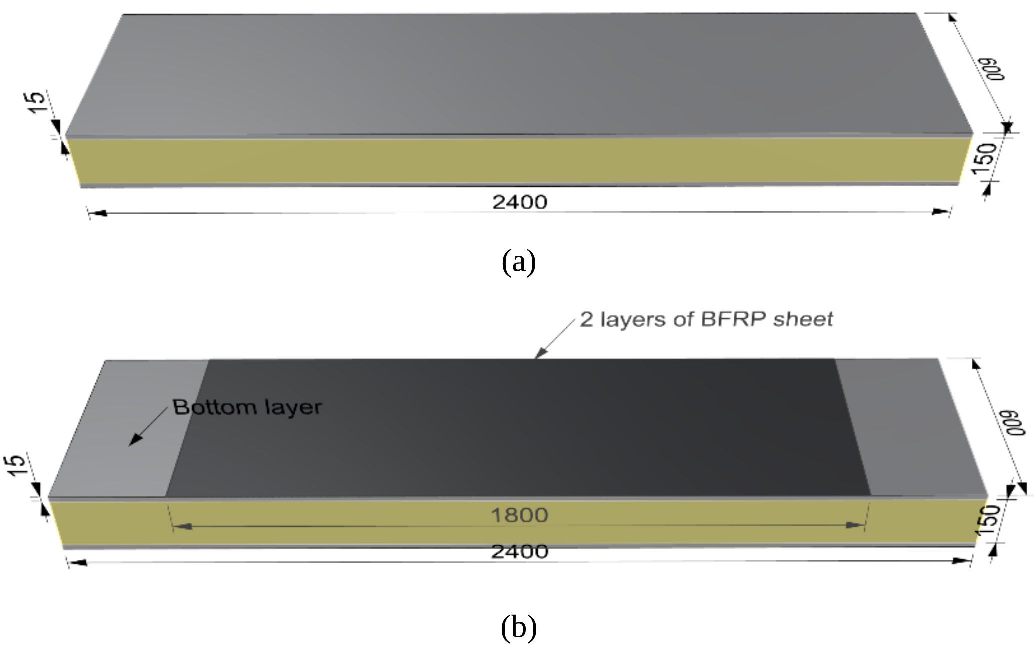

Figure 5.2 Dimension of S1 and S2 (unit: mm): (a) S1; (b) S2.

5.2.2 Setup for quasi-static four-point bending test

The designed setup and the actual setup for the four-point bending test are shown in Figure 5.3 and Figure 5.4, respectively. The test setup includes a testing frame, A-frame supporting system, load cell, connecting hinges, hydraulic jacket, loading strut, measuring cameras and data acquisition system. The rotation hinge is connected to the loading frame and load cell (50 kN). The hydraulic loading jack is connected to the load cell and the loading strut to provide the loading with an oil pump system. A specially designed loading head is manufactured to provide the four-point bending loading system (Figure 5.3). The roller and pin system are applied to provide the simple supported boundary conditions. The effective span of the tested sandwich panel was 2100 mm. The distance between the loading roller and the support and the distance between the two loading rollers are 700 mm, which is 1/3 of the effective span of the tested samples. The sandwich panel is loaded with a hydraulic jack with a loading rate of 1 mm/min. The DIC method is used to track the full-field deformations as shown in Figure 5.4. Due to the capturing limit, two cameras are set up and each covered half of the beam with an overlap in the middle, as shown in Figure 5.5. The image processing is performed by using the GOM Correlate software program, and the test results are synchronised manually.

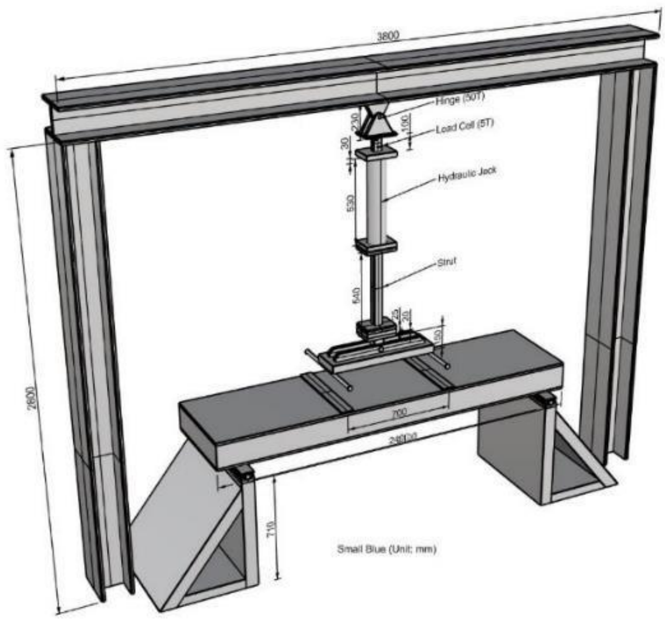

Figure 5.3 Designed setup of four-point bending test

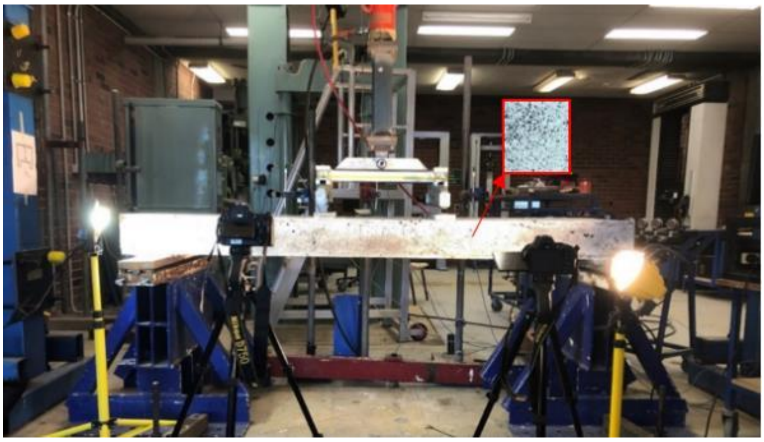

Figure 5.4 Photograph of four-point bending test setup

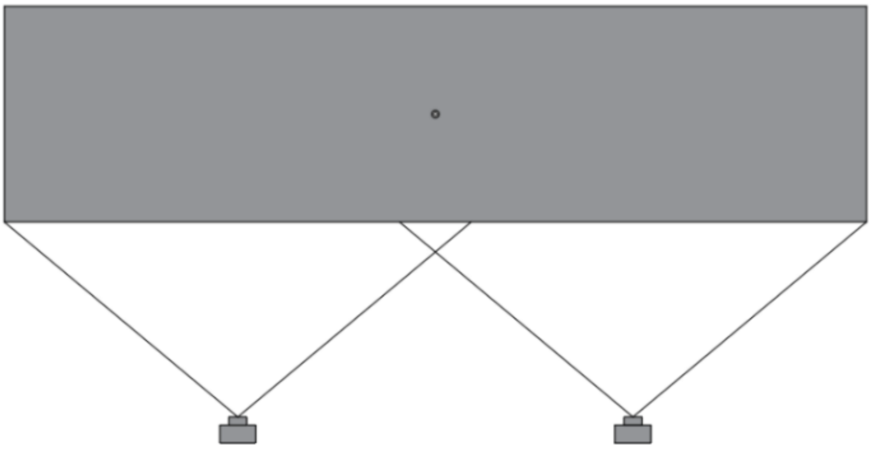

Figure 5.5 Cameras arrangement

5.2.3 Setup for quasi-static axial compressive test

The behaviour of the developed structural lightweight panel is also assessed by conducting quasi-static axial compressive test. The test setup is performed according to ASTM E-72. The detailed setup is shown in Figure 5.6. The axial compression test is conducted under a large loading frame with a capacity of 4000 KN and the clear height of the large loading frame is 3400 mm. The sandwich panel is placed vertically under the large loading frame. As shown in Figure 5.6, the load is applied to the clamping system and the hinge supports are connected to the clamping system using the load spreader and pressure transducer. The designed clamping system and load spreader are shown in Figure 5.7 and Figure 5.8, respectively. Two hinges at the bottom and one hinge at the top are used to simulate the pin support boundary conditions. The hydraulic jacks are managed using a hydraulic control unit equipped with a pressure transducer to measure the applied load. The test setup and the top-loading and bottom support systems are shown in Figure 5.9 and Figure 5.10, respectively.

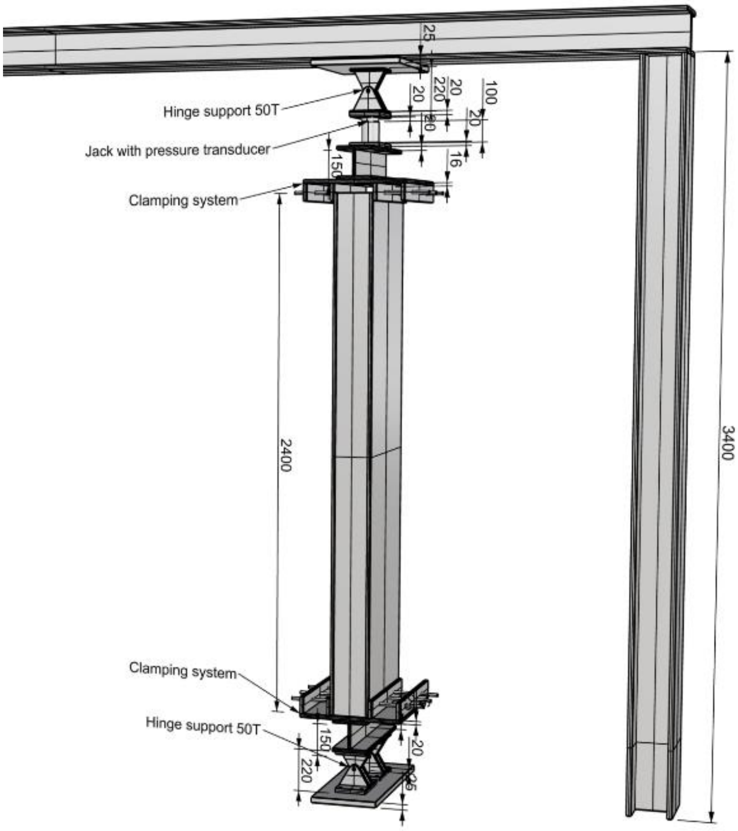

Figure 5.6 Designed setup of axial compressive test (Unit: mm)

The DIC method is used to measure the displacement and strain fields of the developed sandwich panel during the test. Instead of measuring the entire section of the panel with 2400 mm high, the middle part of 1200 mm is measured using the DIC method. One Sony camera and spotlights are used to record the images during the test, as shown in Figure 5.11.

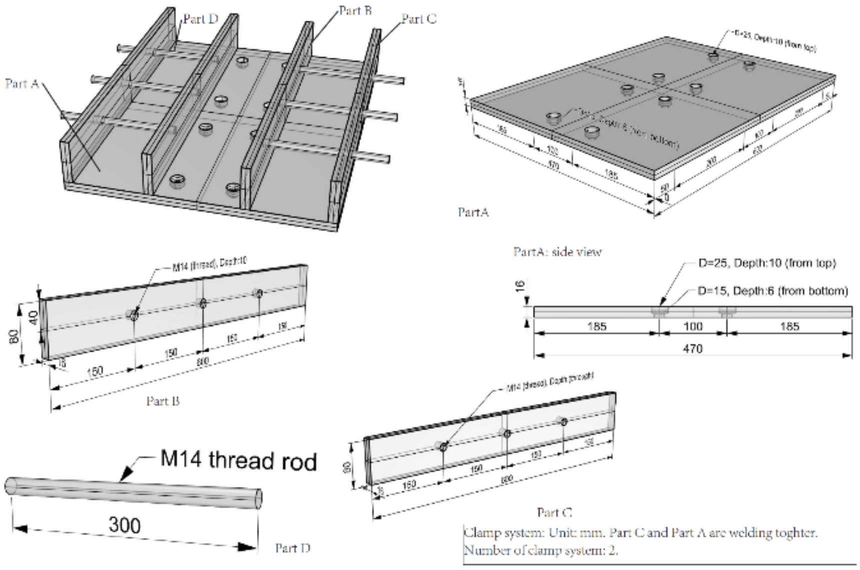

Figure 5.7 Clamping system for axial compressive test

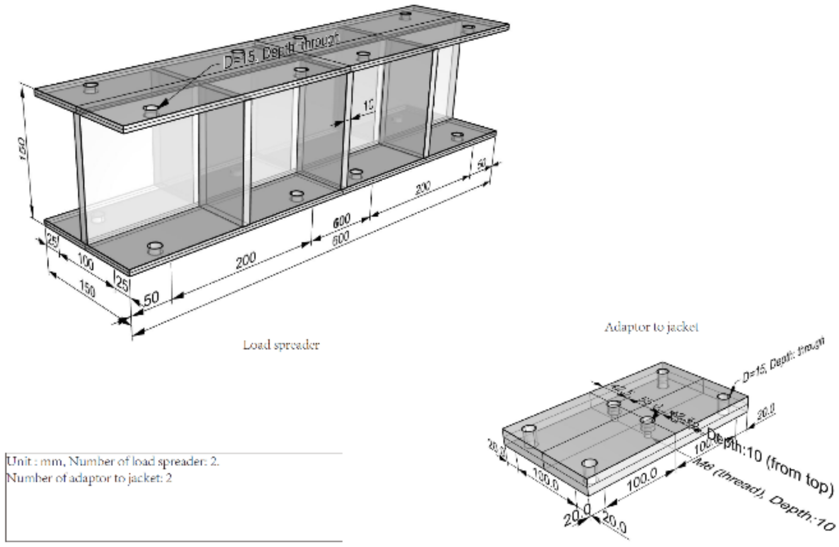

Figure 5.8 Load spreader for axial compressive test

Figure 5.9 Axial compressive test setup

Figure 5.10 Loading and clamping systems

Figure 5.11 Setup for the DIC measuring system

5.2.4 Vibration test setup

Force hammer impact vibration tests are conducted to obtain vibration characteristics of the sandwich panels S1 and S2. Ten PCB accelerometers are attached on the top surfaces of the specimens S1 and S2. The arrangement of the placed accelerometers is shown in Figure 5.12. The span between two supports at the ends of S1 and S2 is kept at 2100 mm. The distance between two accelerometers in the longitudinal direction is 350 mm. The distance between the sensors in the width direction is 500 mm. The mass of the installed accelerometers is minimum compared to the slab and is assumed to have a negligible effect on the vibration properties of the tested samples. The steel roller and pin system are adopted to simulate the simply-supported boundary conditions. National Instruments (NI9234) data acquisition system and commercial software 'Signal Express' are used to record the acceleration responses from the vibration test. The entire test setup is shown in Figure 5.13. For the hammer impact vibration tests, an instrumented hammer is used to apply an excitation force at the 1/4 and 1/2 span of the specimens from the left support. Five impact tests are recoded for each excitation group. The sampling rate is set as 100 Hz. The experimental setup of the hammer impact vibration test is shown in Figure 5.13.

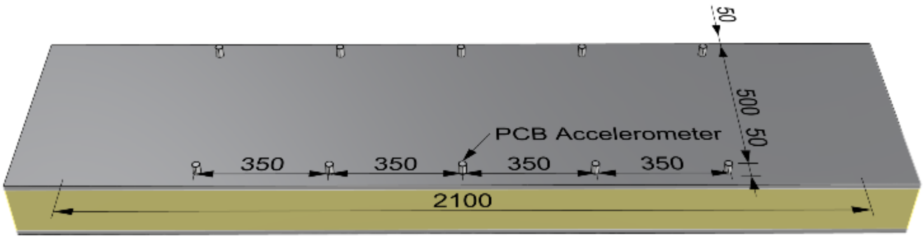

Figure 5.12 Arrangement of the accelerometer

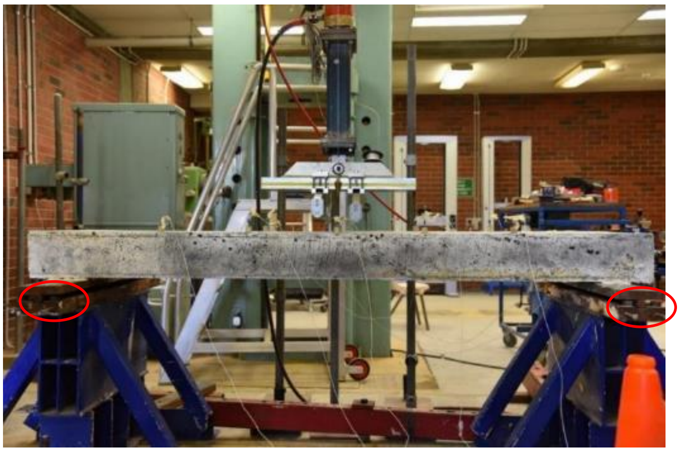

Figure 5.13 Test setup for the vibration test

5.3 Experimental results of the quasi-static four-point bending test

Two samples (S1 and S2) are tested, and the typical bending behaviours of S1 and S2 under the quasi-static four-point bending are shown in Figure 5.14 in terms of load vs mid-span displacement. The load vs mid-span displacement curves exhibit linear behaviours at the beginning stage, where S2 experiences higher flexural stiffness than S1. Then, the load vs mid-span displacement curves show a nonlinear trend until a sudden drop. This sudden drop means that the S1 and S2 samples collapsed and the critical failure load was reached. The critical failure loads for S1 and S2 are19 kN and 25 kN, which are 15 kPa/m^2 and 19 kPa/m^2, respectively, with the difference of 26%. The deflections of the panel samples of S1 and S2 corresponding to live load 5 kPa (which is for office or work areas according to AS 11701-2002) are 5 mm and 4 mm, respectively, which are smaller than the deflection limit of 9.6 mm (*L/250*) according to AS 3600-2001. Although both S1and S2 samples experience sudden drop, they have different failure modes. The failure modes of S1 and S2 are shown in Figure 5.15. S1 has an obvious crack around the mid-span of the test sample and the crack occurred in the bottom FRG skin layer and the PUR foam core. For S2, a 45° shear crack appears on the left side of the sandwich panel near the support and developed through the entire section. The failure mode changes from flexural failure of S1 to shear failure of S2. It is due to the increased flexural strength of the panel strengthened with BFRP sheet. In addition, S2 experienced the delamination between the top FRG skin layer and the PUR foam core after the appearance of the 45° crack.

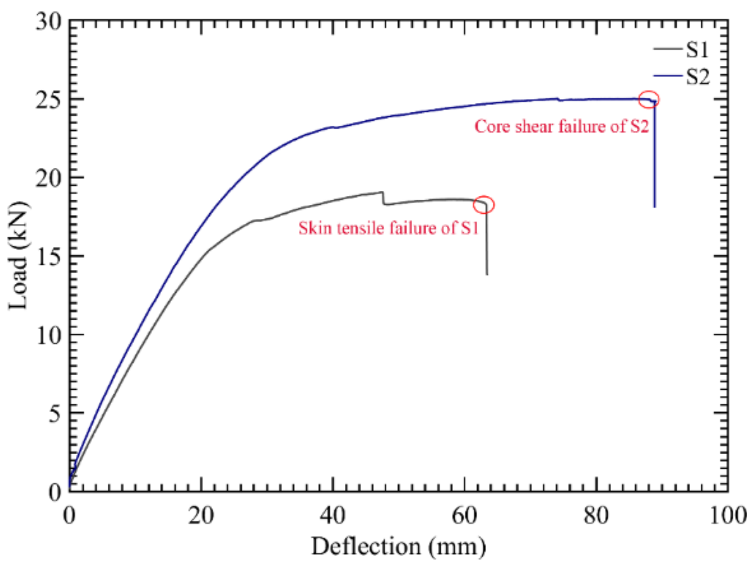

Figure 5.14 Load vs mid-span deflection curves for the samples S1 and S2

(a)

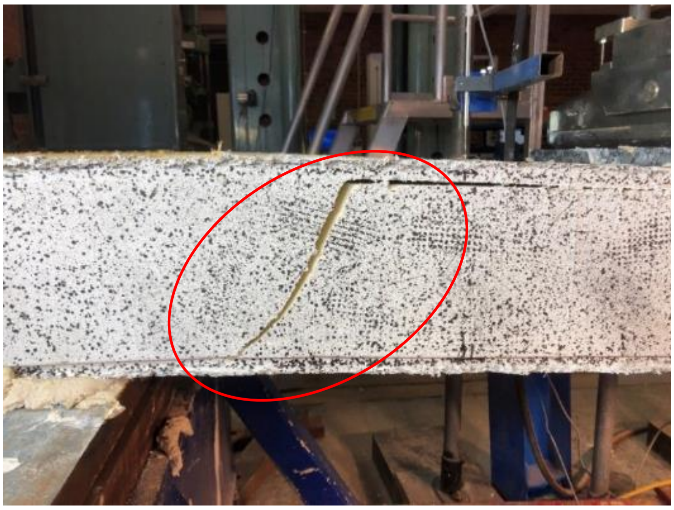

(b)

Figure 5.15 Failure modes of S1 and S2: (a) S1; (b) S2

Figure 5.16 and Figure 5.17 show the strain fields of FRG skin layer for S1 and the PUR foam core for S1 and S2 by DIC, respectively. The max strain of the FRG skin layer for S1 is about 3% as shown in

Figure 5.16, which causes the tensile failure of the bottom FRG skin layer. The shear strain field of the PUR foam core for S2 is shown in Figure 5.17 and the max shear strain of the PUR foam for S2 is much higher than that of S1, which leads to the core shear failure of the S2 sample. The reason for this shift in the failure mode for S1 and S2 is due to the BFRP sheet reinforcement. With the BFRP sheet reinforcement, S2 has higher tensile strength at the back FRG skin under bending load. However, the shear strength of the PUR foam is not high enough to prevent S2 from the shear failure of the PUR foam core.

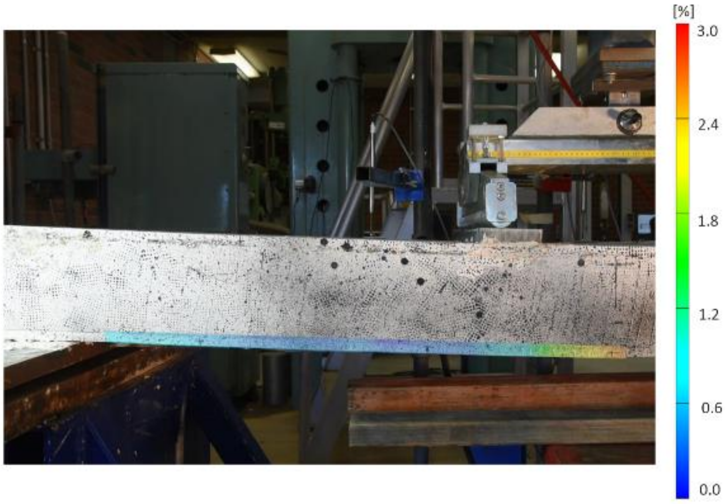

Figure 5.16 Strain field of the bottom FRG skin layer for S1

(a)

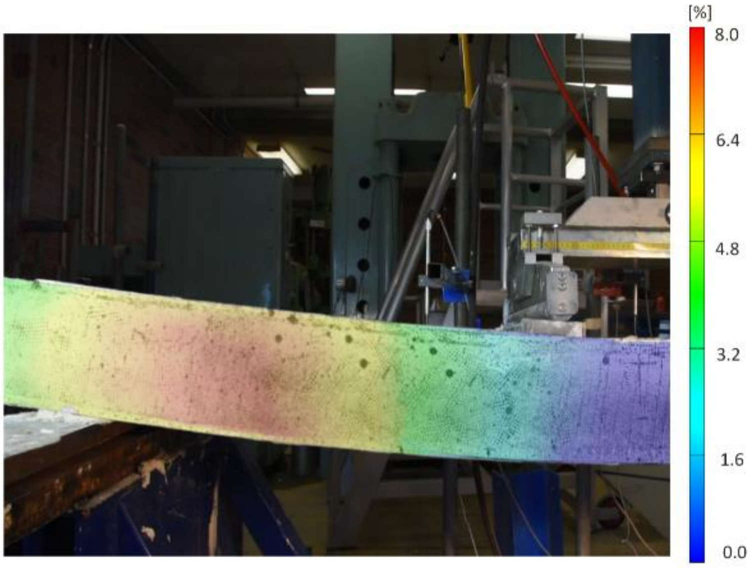

(b)

Figure 5.17 Shear strain field of the PUR foam: (a) S1; (b) S2

As mentioned in Chapter 4, an analytical solution is given to predict the critical failure load of the sandwich panel under flexural loading. The failure mode of S1 predicted from the failure map is skin tension failure, with the experimental results in this study confirming this prediction. Furthermore, the critical failure load predicted by Eq. (4.2) is 24 kN and the actual failure load from the test is 19 kN. For S2, the failure mode is the PUR foam core failure based on the experimental results. The critical failure load predicted by Eq. (4.2) is 30 kN and the actual failure load is 25 kN from the test. The actual critical failure load is lower than that predicted by Eq. (4.2), which might be owning to the workmanship of sample preparation and possible minor defects during manufacturing.

5.4 Experimental results of the axial compression test

One sample (C1) was tested under quasi-static axial compressive loading, and the typical load and displacement response of the panel C1 is shown in Figure 5.18. The dimension of the panel is 2400 mm × 600 mm × 180 mm. The critical collapse load was about 145 kN. The failure mode of the panel under the axial compression load is shown in Figure 5.19. As shown the panel failed by global buckling and delamination in the middle area between the FRG skin layer and the PUR foam core layer. The sandwich panel lost its capability of sustaining load and failed suddenly. The out-of-plane deflection field of the middle part of the tested panel was obtained using the DIC method and the results are shown in Figure 5.20. Figure 5.20 shows the deflection field along the X direction right before the failure state. The deflection field also indicates that the developed sandwich panel is prone to experience global buckling under axial compressive loads.

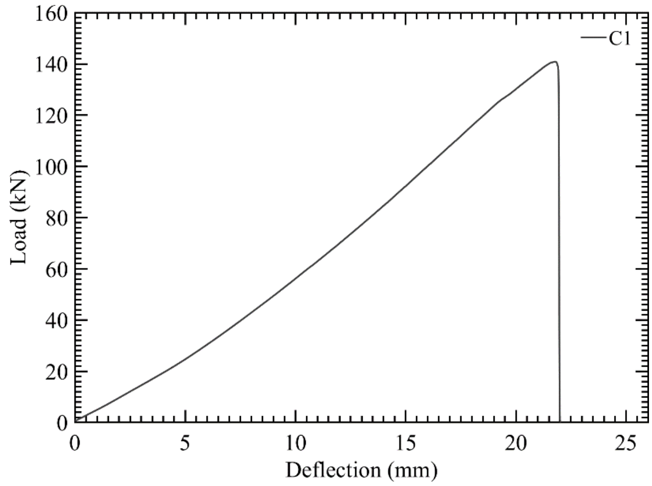

Figure 5.18 Load vs mid-span lateral deflection curve

Figure 5.19 Failure mode of the panel under axial compressive loading (unit: m)

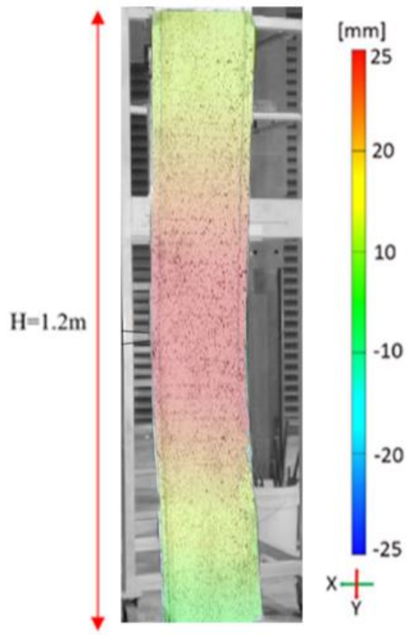

Figure 5.20 Out-of-plane deflection field of the developed sandwich panel (at the middle part)

In Chapter 4, the critical failure load for the sandwich panel can be predicted by Eq. (4.18). The predicted critical load is 158 kN and the actual critical failure load was about 145 kN from the test. This is slightly lower than the predicted critical failure load, which might be due to the eccentricity induced by possible defects of the specimen and the experiment setup.

5.5 Experimental results of the force hammer impact vibration test

FDD method developed by Brinker et al. (116) is applied in this study to identify vibration characteristics, such as natural frequencies, damping ratios, and modal shapes. FDD is an extension of the classical frequency-domain method, which is also referred to as the basic frequency-domain technique or the peak picking technique. This method can be used to identify the vibration characteristics of a structure by applying the singular value decomposition to the output response spectral density matrix. FDD is applicable for both impact vibration and ambient vibration tests.

Damping ratios are estimated from a mode-isolated and free decay response obtained by an inverse Fourier transformation of the output spectrum after applying a zero-padding technique (117). FDD method is an output only method. Therefore, no input information is required for the analysis process.

Acceleration time histories measured from the sensor at the mid-span of S1 and S2 samples under the hammer impact vibration tests are shown in Figure 5.21. Each test group is tested 5 times and therefore 50 acceleration time histories are recorded for each test group S1 and S2. The fast Fourier transform spectra of these acceleration response in the mid-span are shown in Figure 5.22. The identified modal characteristics of S1 and S2 are shown in Table 5.2. The identified first three mode shapes for the S1 and S2 samples, including two bending modes and one torsional mode, are shown in Figure 5.23 and Figure 5.24. As shown in Table 5.2, the first three natural frequencies of S2 are slightly higher than those of S1, which is caused by the addition of the BFRP sheet on the surface of the FRG skin. The results demonstrate that the applied BFRP sheet can slightly increase the stiffness of the panel, which leads to the increase in natural frequencies. However, the damping ratios are nearly the same for S1 and S2, which means the application of BFRP sheet might not be able to change the damping properties of the developed sandwich panels.

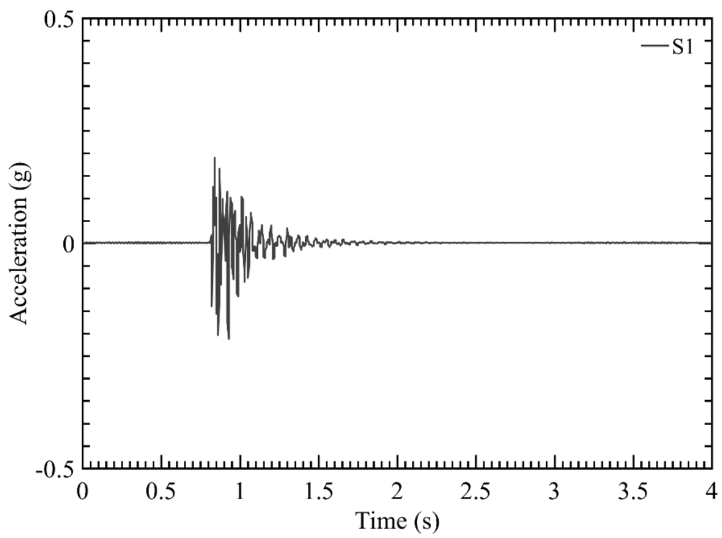

(a)

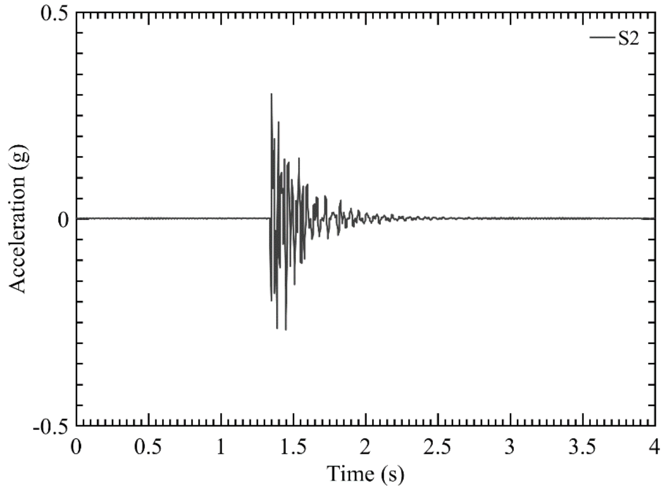

(b)

Figure 5.21 Measured acceleration response at the mid-span of specimens: (a) S1; (b) S2.

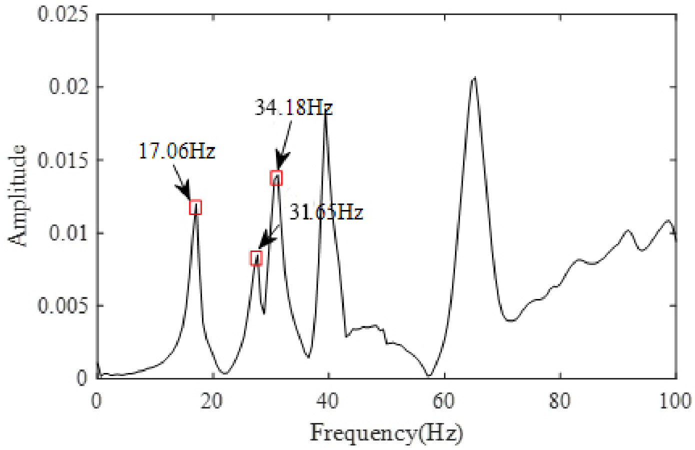

(a)

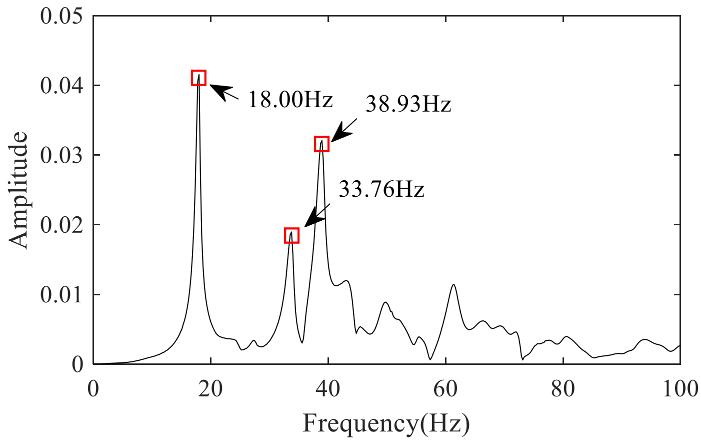

(b)

Figure 5.22 Fast Fourier spectrum of the measured acceleration time histories: (a) S1; (b) S2

Table 5.2 Identified modal frequencies and damping ratios of S1 and S2

Mode	S1		S2	
	Natural frequency (Hz)	Damping ratio	Natural frequency (Hz)	Damping ratio
1	17.06	0.05	18.00	0.052
2	31.65	0.04	33.76	0.042
3	34.18	0.058	38.93	0.055

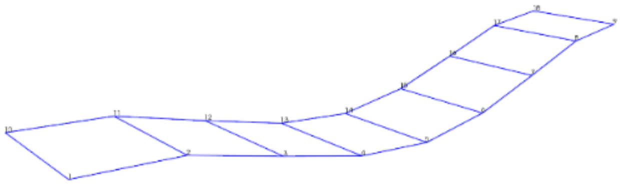

(a)

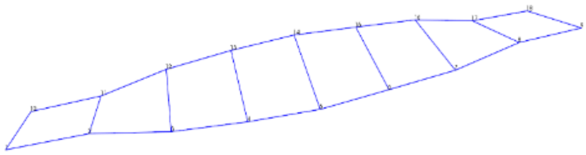

(b)

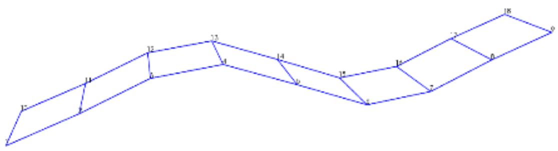

(c)

Figure 5.23 Identified mode shapes of S1: (a) First mode; (b) Second mode; (c) Third mode

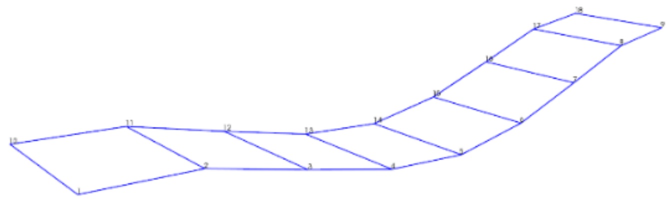

(a)

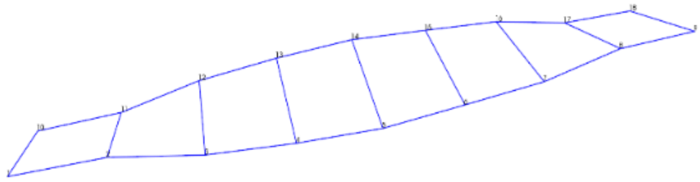

(b)

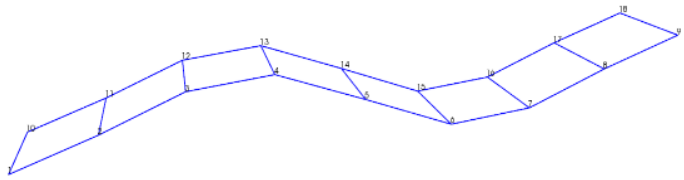

(c)

Figure 5.24 Identified mode shapes of S2: (a) First mode; (b) Second mode; (c) Third mode

5.6 Finite element modal analysis of the sandwich panel

5.6.1 Finite element models

Two different models are developed for the finite element analysis to calculate the vibration characteristics of the developed sandwich panels. The first model uses solid elements to build the finite element model of the sandwich panel. The detailed geometries of the sandwich panel including the skin layers and the PUR foam layer of the tested specimens are taken to build the finite element model. For comparison, a second model is developed using the equivalent shell element therefore the detailed geometries of the skin layers and core layer of the sandwich panel are not exactly replicated. Instead, equivalent shell thickness is used to develop the finite element model to obtain the vibration characteristics of the sandwich panel. The material properties of FRG, PUR foam and BFRP can be found in Table 4.6, Table 4.1, and Table 5.1

For the solid element model, the commercially available finite element analysis package ABAQUS 6.13-1 is used with ABAQUS CAE as the pre- and post-processor. C3D8 solid element is used to model both the FRG skin layer and the PUR foam core. The element size for the FRG skin layer is defined as 50 mm × 50 mm × 15 mm and the element size for the PUR foam core is 50 mm × 50 mm × 50 mm. The simply-support boundary condition is applied to the finite element model and the effective span is set as 2100 mm in accordance with the experimental study. For the sample S2, all the details of the finite element model are the same as those for the sample S1. The BFRP sheet is also modelled using the C3D8R solid element, with an element size of 50 mm × 50 mm × 0.24 mm. It should be noted that in this model, only solid element is used. The aspect ratio of the solid element for the BFRP sheet is very large which is likely to make the element and simulation unstable. Nonetheless, since the simulation is limited to modal analysis only and the contribution of BFRP sheet to the stiffness is not prominent, solid element is still used in the simulation. If structural response is needed, shell element should be a better choice for modelling the BFRP sheet. The finite element models developed for S1 and S2 using solid elements are shown in Figure 5.25.

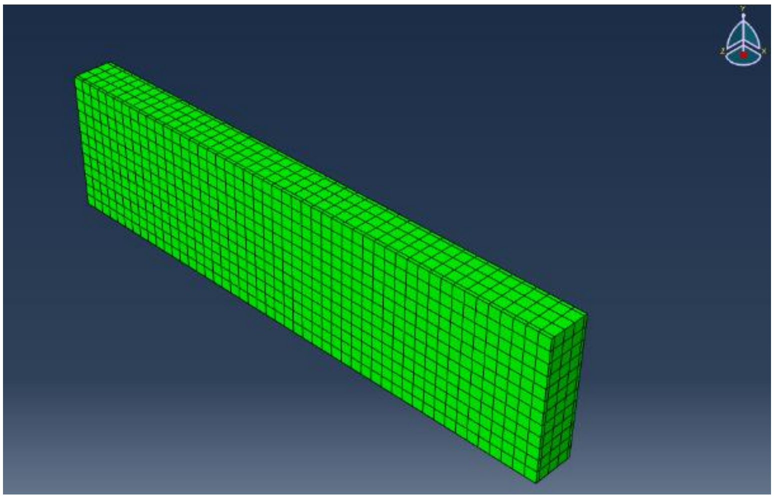

(a)

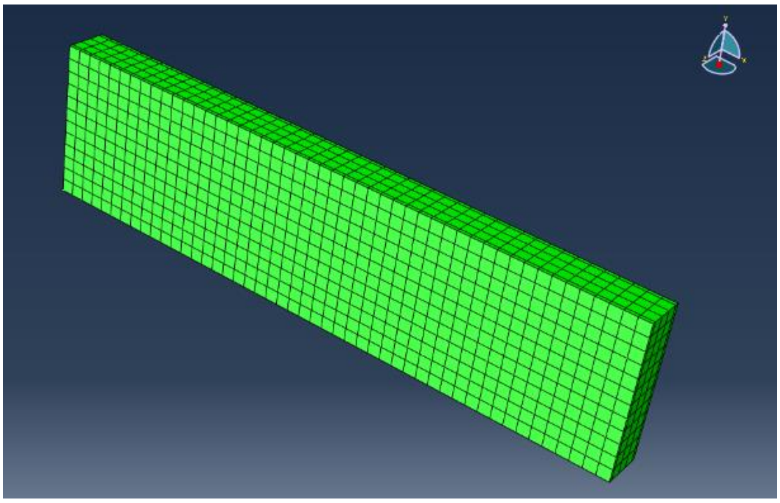

(b)

Figure 5.25 3D solid element model for vibration analysis: (a) S1; (b) S2

For the equivalent shell element model, the four nodes isoperimetric shell element in Abaqus is used to build the finite element model. Each node has six degrees of freedom, three for translational displacements and three for rotational displacements. The used shell element is called the 'general-purpose element' since it can be performed for a wide range of applications. This element can be used as thin shells or thick shells. Its formulation does not rely on a single theory but a patchwork of several concepts to make the element as effective as possible. The transverse shear is treated in the same manner as that in the Mindlin-Reisner theory, also known as the first-order shear deformation theory. The transverse shear is taken into account and the shear stress is considered to be constant through the thickness.

Five independent kinematic variables are used: the displacement field u, v, w and the rotations of the normal regarding the mid-surface β_x and β_y. The displacement field can be written as the following equations:

$$u(x, y, z) = u_0(x, y) + z\beta_x(x, y) \tag{5.1}$$

$$v(x, y, z) = v_0(x, y) + z\beta_y(x, y) \tag{5.2}$$

$$w(x, y, z) = w_0(x, y) \tag{5.3}$$

where *z* is the thickness direction. The first order shear deformation theory comes from the development at the first order in *z* of *u(x,y,z)* and *v(x,y,z)*. The strain field can be expressed by the following equations:

$$\varepsilon_{xx} = u_{0,x} + z\beta_{x,x} \tag{5.4}$$

$$\varepsilon_{yy} = v_{0,y} + z\beta_{y,y} \tag{5.5}$$

$$\varepsilon_{zz} = 0 \tag{5.6}$$

$$\gamma_{xy} = \left(u_{0,y} + v_{0,x}\right) + z\left(\beta_{x,y} + \beta_{y,x}\right) \tag{5.7}$$

$$\gamma_{yz} = \beta_y + w_{0,y} \tag{5.8}$$

$$\gamma_{xz} = \beta_x + w_{0,x} \tag{5.9}$$

The transverse shear strain is constant through the thickness while the 3D elasticity theory predicts a quadratic variation. A correction coefficient κ is used to account for the approximation and a correct prediction of the strain energy is given as

$$\gamma_{\alpha z} = \kappa\left(\beta_\alpha + w_{0,\alpha}\right) \ \alpha = x, y \tag{5.10}$$

where κ is the correction factor, and κ can be found by two ways. Reissner proposes to correct the transverse shear energy for a plate in pure bending (κ = 5/6) while Mindlin matches the first anti-symmetric mode of vibration due to transverse shear ($\kappa = \pi^2/12$) (118). This is valid for a homogeneous and isotropic plate. The first order shear deformation theory provides good results for thin and thick plates for most of the encountered problems. For a sandwich plate, κ can be computed by shear stiffness by matching the potential energy of the external forces with the strain energy of the system. If the assumption is $E_c \ll E_f$ and $t \ll c$, κ can be found equal to 1.

The section properties of the laminated structures across the thickness direction can be calculated by the first order shear theory (119), as shown in Figure 5.26. The strain energy can be expressed as

$$U = \frac{1}{2}\int(\varepsilon^T\sigma + \gamma^T\tau)dV = \frac{1}{2}\int u^T \int\left[B_m^T D^k B_m + B_m^T z D^k B_m + B_f^T z^2 B_m + B_f^T z^2 D^k B_f\right] dz \cdot u \cdot dA + \frac{1}{2}\int u^T \int[B_c^T D_c^k B_c]\, dz \cdot u \cdot dA \tag{5.11}$$

where B_m, B_f and B_c are the membrane component, bending component, and shear component of strain-displacement matrices, respectively. The stiffness matrix can be decomposed into more components:

$$K^{(e)} = K^{(e)}_{mm} + K^{(e)}_{mf} + K^{(e)}_{fm} + K^{(e)}_{ff} + K^{(e)}_{cc} \tag{5.12}$$

where $K^{(e)}$ is the stiffness matrix, $K^{(e)}_{mm}$ is the membrane part of the stiffness matrix, $K^{(e)}_{mf}$ and $K^{(e)}_{fm}$ are the membrane-bending coupling components, $K^{(e)}_{ff}$ is the bending part, and $K^{(e)}_{cc}$ is the shear part. They are given as

$$K^{(e)}_{mm} = \sum_{k=1}^{nc} \int B_m^T D^k B_m (z_{k+1} - z_k) dA \tag{5.13}$$

$$K^{(e)}_{mf} = \sum_{k=1}^{nc} \int B_m^T D^k B_f \frac{1}{2} (z_{k+1}^2 - z_k^2) dA \tag{5.14}$$

$$K^{(e)}_{fm} = \sum_{k=1}^{nc} \int B_f^T D^k B_m \frac{1}{2} (z_{k+1}^2 - z_k^2) dA \tag{5.15}$$

$$K^{(e)}_{ff} = \sum_{k=1}^{nc} \int B_f^T D^k B_f \frac{1}{3} (z_{k+1}^3 - z_k^3) dA \tag{5.16}$$

$$K^{(e)}_{cc} = \sum_{k=1}^{nc} \int B_c^T D^k B_c \frac{1}{3} (z_{k+1} - z_k) dA \tag{5.17}$$

where *nc* denotes the number of layers across the thickness direction.

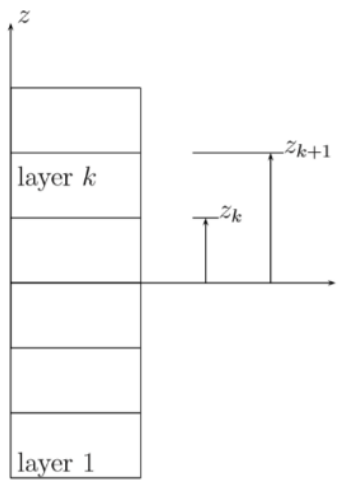

Figure 5.26 Laminated structures: organization of layers in the thickness direction (119)

The same samples are modelled but with shell elements (S4R element) in Abaqus 6.13. The shell element size is 50 mm × 50 mm and the finite element models for S1 and S2 are shown in Figure 5.27, respectively. The boundary condition is also the same as that for the solid element model.

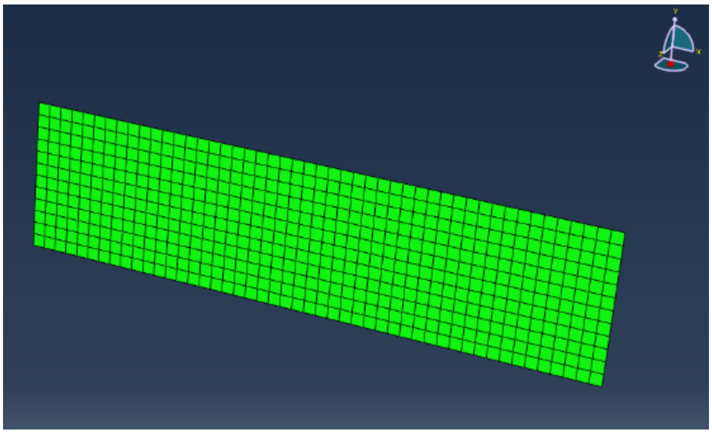

(a)

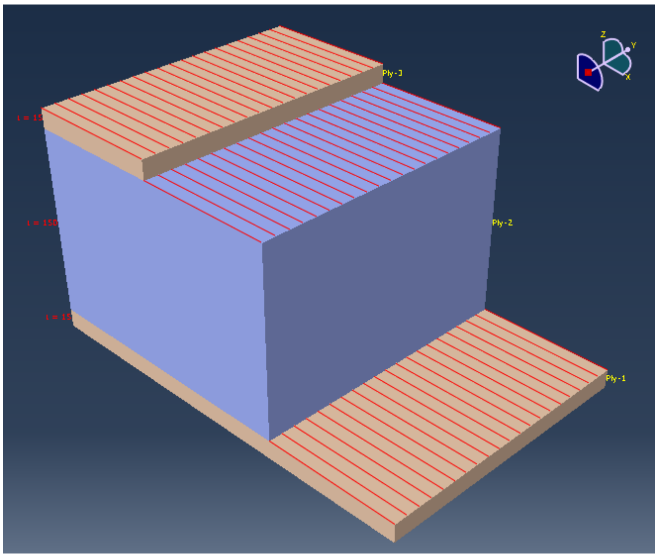

(b)

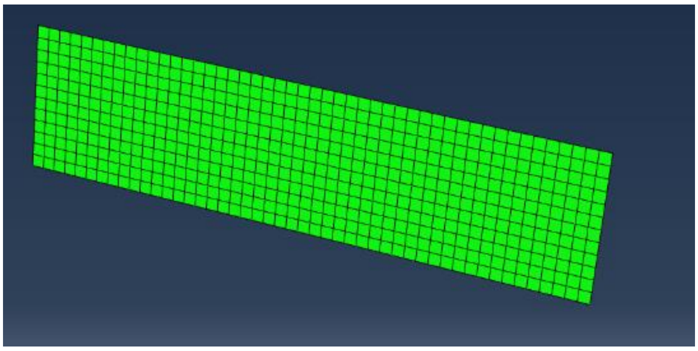

(c)

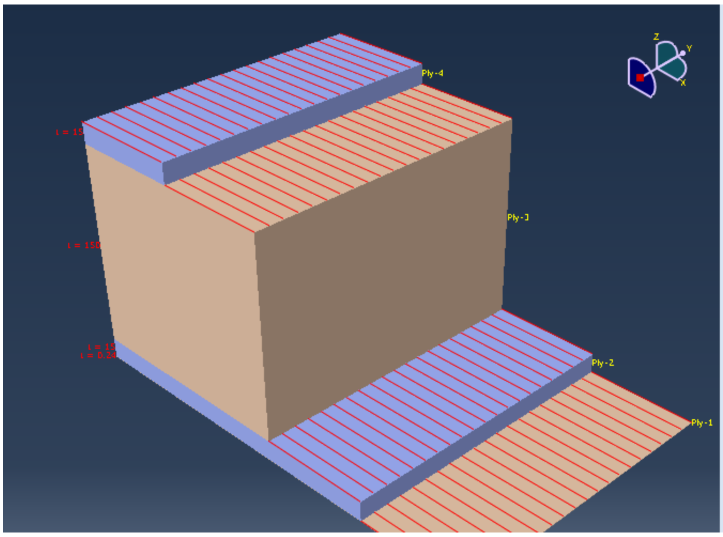

(d)

Figure 5.27 Shell element model for the free vibration analysis: (a) S1; (b) Section for S1; (c) S2; (d) Section for S2

5.6.2 Finite element modelling results

The first three natural frequencies obtained from the finite element analysis are compared with the experimental results for the samples S1 and S2, as shown in Table 5.3 and Table 5.4. Natural frequencies obtained from the finite element analysis for S1 and S2 by the solid element and equivalent shell element methods, as shown in Table 5.3 and Table 5.4, agree with the identified results well from the forced hammer impact vibration tests. The corresponding mode shapes for S1 and S2 by finite element analysis using solid element and shell element are shown in Figure 5.28 and Figure 5.29. Coordinate Modal Assurance Criterion (COMAC) is adopted to compare the mode shapes generated by finite element analysis and the identified ones from the forced hammer impact vibration tests. COMAC has been applied to indicate the consistency between two mode shapes at certain degrees of freedom and can be calculated using the following formula (120), once the mode pairs have been identified:

$$COMAC_j = \frac{\left(\sum_{l=1}^{L} \Psi_{X_{lj}} \Psi_{A_{lj}}\right)^2}{\sum_{l=1}^{L} \Psi_{X_{lj}}^2 \sum_{l=1}^{L} \Psi_{A_{lj}}^2} \tag{5.18}$$

where j represents the j^{th} degree of freedom, $\Psi_{A_{lj}}$ is the mode shape of the data set A and the l^{th} mode pair, and $\Psi_{X_{lj}}$ is the mode shape of the data set X and the l^{th} mode pair. For two modes, COMAC has a value between 0.0 to 1.0. If two modes have poor correlation across all the degrees of freedom, it will have a value close to 0.0. If two mode shapes are identical, it will have a value of 1.0.

The COMAC values are calculated to compare the mode shapes from finite element analysis using both solid element and equivalent shell element and the identified ones from the forced hammer impact vibration test. The results of COMAC values of the first three modes for S1 and S2 are shown in Table 5.5 and Table 5.6. As observed, the COMAC values of S1 and S2 for the first three modes are close to 1. It can be concluded that the mode shapes obtained from the finite element analysis with the solid element and equivalent shell element are nearly identical as those identified for S1 and S2 in experimental tests (Figure 5.26). The finite element analysis by both the solid element and equivalent shell element can predict the vibration characteristics of the sandwich panel accurately, but the finite element analysis with shell element is much more efficient than that with solid element. For example, the total calculation time for the modal analysis of S1 using solid elements is 1.4 s, but it only needs 0.4 s for the same analysis by shell elements.

Table 5.3 Natural frequency of the first three modes from the finite element analysis for S1

Mode	FEA result (Hz)		Test result (Hz)	Relative error (%)	
number	SE	ESE		SE	ESE
1	17.72	17.87	17.06	3.9	4.7
2	32.49	33.4	31.65	2.7	5.5
3	35.60	36.46	34.18	4.2	6.7

*SE = solid element, ESE = equivalent shell element

Table 5.4 Natural frequency of the first three modes from the finite element analysis for S2

Mode number	FEA result (Hz) SE	FEA result (Hz) ESE	Test result (Hz)	Relative error (%) SE	Relative error (%) ESE
1	18.02	18.09	18.00	0.1	0.5
2	33.56	33.86	33.76	0.6	0.3
3	36.40	36.83	38.93	6.5	5.4

* SE = solid element, ESE = equivalent shell element

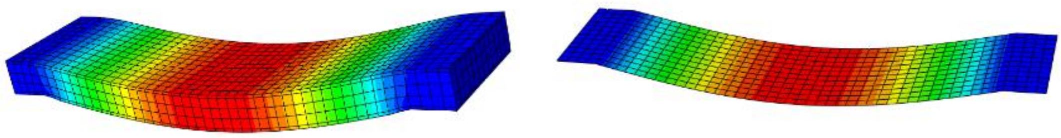

(a) Mode 1

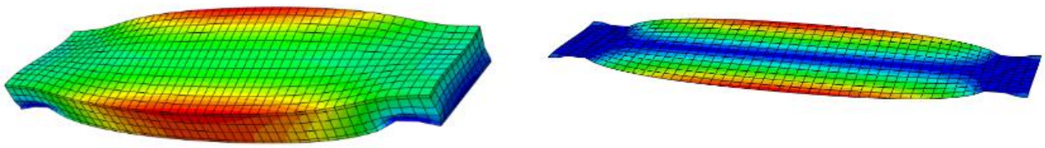

(b) Mode 2

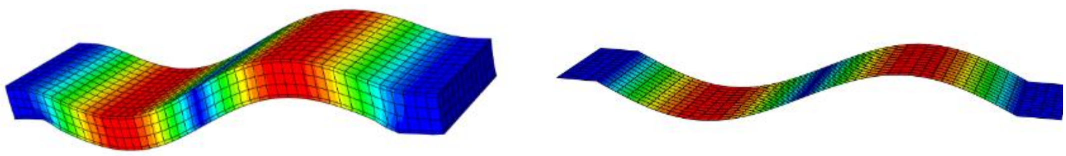

(c) Mode 3

Figure 5.28 The first three mode shapes from the finite element analysis for S1: (a) First mode; (b) Second mode; (c) Third mode

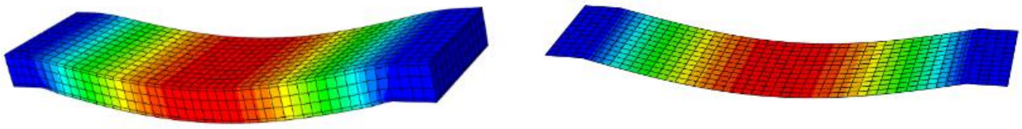

(a) Mode 1

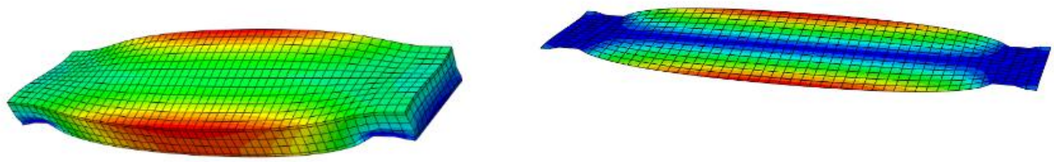

(b) Mode 2

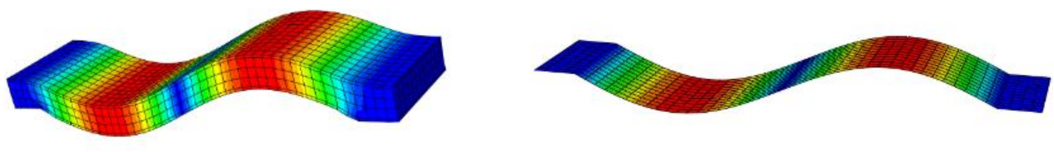

(c) Mode 3

Figure 5.29 The first three mode shapes from the finite element analysis for S2: (a) First mode; (b) Second mode; (c) Third mode

Table 5.5 COMAC values for S1 from test and finite element analysis

Test	SE			ESE		
result	1st mode	2nd mode	3rd mode	1st mode	2nd mode	3rd mode
1st mode	0.991	0.000	0.000	0.989	0.000	0.000
2nd mode	0.000	0.995	0.000	0.000	0.991	0.000
3rd mode	0.000	0.000	0.984	0.000	0.000	0.980

Table 5.6 COMAC values for S2 from test and finite element analysis

Test result	SE 1st mode	SE 2nd mode	SE 3rd mode	ESE 1st mode	ESE 2nd mode	ESE 3rd mode
1st mode	0.992	0.000	0.000	0.990	0.000	0.000
2nd mode	0.000	0.995	0.000	0.000	0.989	0.000
3rd mode	0.000	0.000	0.975	0.000	0.000	0.969

5.7 Summary

In this chapter, structural performance of the full-size sandwich panels under four-point bending and axial compressive loading and the vibration characteristics of sandwich panels are studied. Two types of sandwich panels are prepared for four-point bending test. The first one (S1) is a sandwich panel applying FRG as the skin and PUR foam as the core. The second type (S2) is the same as the first type (S1) except strengthened by BFRP sheets on the bottom FRG skin. The structural behaviours of these two types of sandwich panels under four-point bending are studied. The failure mode of S1 is the skin tensile failure and the failure mode of S2 is the PUR foam core failure under four-point bending. The BFRP sheet attached to the bottom skin layer of the developed sandwich panel shifts the failure mode of the panel from skin tensile failure to core shear failure. The critical failure load of S2 is higher than that of S1 by 26% owing to the addition of the BFRP sheets. In addition, the structural performance of the full-size sandwich panel (C1) is studied by conducting the quasi-static axial compressive test. The failure mode of the panel is global buckling followed by the delamination between the FRG skin layer and the PUR foam core layer under axial compressive loading. The critical collapse load is 145 kN under axial compressive load. The analytical models in Chapter 4 can give reasonable predications of the experimental tests in this chapter.

The forced hammer impact vibration tests are conducted to study the vibration characteristics of the developed sandwich panels. Natural frequencies and damping ratios of the identified first three modes are very close for S1 and S2 specimens, indicating that the applied BFRP sheet does not change the vibration characteristics significantly. The finite element analyses by using the solid element and equivalent shell element are conducted and can accurately estimate the modal information of the sandwich panels, but the shell element is much more efficient in terms of calculation time. These finite element modelling techniques will be applied in the next chapter to investigate the serviceability of using the developed sandwich panels for building floors.

6 Vibration serviceability of the geopolymer composite lightweight sandwich panels under human walking activity

6.1 Introduction

In recent years, the demand for sustainability and industrialisation of buildings has promoted researchers and industries to develop innovative lightweight materials and structures that are fast to construct and flexible in their intended final applications (121). Some researchers believe that the design of long-span or the application of lightweight floor construction may be governed by serviceability requirements rather than strength and dynamic performance (70). Human perception of vibrations is very sensitive, and excessive exposure to annoying vibrations causes discomfort and possible health problems for occupants. The sources causing the vibrations of buildings can be classified into two categories: external sources and internal sources (62). External sources refer to building excitations caused by ground vibrations due to passing traffic, wind excitations, or airborne acoustic excitations. Internal sources can generally be considered to include mechanical excitation and human-induced excitation. Examples of mechanical vibrations include lifts, air-conditioning or ventilation plant, heavier office machinery in commercial premises, and appliances such as vacuum cleaners and washing machines in household premises. Human-induced excitation is generally created by dynamic human activities, such as walking, running, jumping, and dancing. Human-induced excitation is the most common and important internal source of dynamic excitation. These typical human activities can induce periodical dynamic loads with different frequencies on the building floor, which might cause excessive vibrations that disturb the comfort of occupants (122). Many slender structures have been found to have difficulties in satisfying the vibration serviceability under human-induced excitations, such as footbridges (123), staircases (124), and open-plan floors (125). The causes of these types of vibration problems are found to be the near resonance of one or more modes of structural vibrations because the range of natural frequencies of these light and slender structures may be coincided with the dominant frequencies of the dynamic loads induced by human activities (126-128). Therefore, newly constructed buildings applying lightweight material might suffer vibration problems under different human activities.

Since one major application of the sandwich panel is to be applied as the floor panels for the prefabricated buildings, this chapter studies the serviceability of a composite floor system that applies the developed sandwich panel as the floor slab under human walking loads by finite element analysis. Three different damping levels of the composite floor are assumed for the evaluation of vibration serviceability. The vibration serviceability is assessed in terms of different vibration assessment parameters of response factor of a_{rms} and *VDVs*. Then, the influence of the composite floor length on the vibration serviceability is studied by finite element analysis under continuous human walking load.

6.2 Human walking load model

The potential for annoying vibrations of contemporary building floors remains high possibility under human-induced loading. As a consequence, the vibration serviceability design has drawn much attention for modern floor designs (129). Some design guidelines are available now at the design stage to predict the vibration response for the assessment of vibration serviceability of buildings floors, including AISC DG11 (130), CRSI (131), SCI P354 (121), CCIP-016 (132), and CSTR43 (133). The application of current guidelines is generally for a single pedestrian at the design stage, where a deterministic walking load model is utilized to represent actual walking(129), which is also the type of human walking load adopted for this study. The gait cycle analysis is the theoretical basics for the human walking load model and is introduced below.

Normal human walking is defined as the gait that people use at low speeds (134). The duration of a complete gait cycle is divided into two periods: stance and swing phase, as shown in Figure 6.1. The stance phase is the phase when the foot is on the ground, which is initiated with ‘heel strike’ and ends with ‘toe off’ of the same foot. This entire process occupies 60% of the entire gait cycle. The swing phase refers to the toe off to the next initial contact on the ground, which constitutes approximately 40% of the remaining gait cycle. There is also a time when both feet are in contact with the ground, i.e., the initial contact of the right foot occurs while the left foot is still on the ground. This period is known as double support or double limb stance, and occurs twice in the gait cycle - at the beginning and end of the stance phase (135).

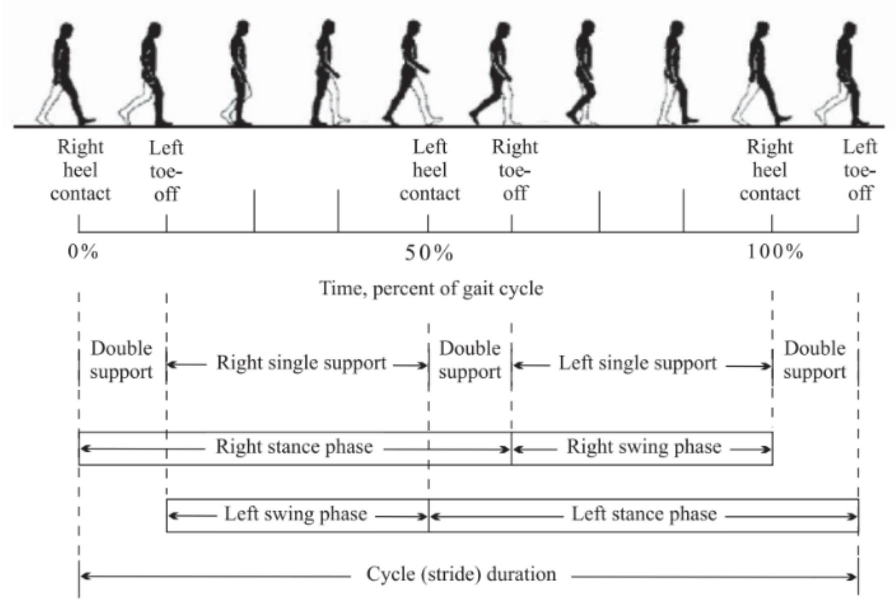

Figure 6.1 Gait cycle (126)

The entire gait cycle can exert the generation of ground reaction forces as shown in Figure 6.2. The whole stance period can be divided into the following sequences: initial contact (IC), loading response (LR), midstance (MSt), terminal stance (TSt) and preswing (PSw). Initially, the ground reaction force is generated by the strikes of the heel on the ground (IC). Then, the impact force is followed quickly by the loading response (LR). During this phase, the foot fully touches the ground and the vertical ground reaction force reaches the first peak (F1). The period of midstance (MSt) follows the LR phase, which is a process of decreasing the ground reaction force. The decrease is because of the shift in the centre of the body weight from one leg to another leg (126). The TSt phase begins with the heel rise and continues until the opposite foot strikes the ground, which follows the second peak of the ground reaction force. Finally, the vertical force pattern starts descending to zero in parallel with the preswing phase and drops to zero at the end of the toe off (TO) phase, as shown in Figure 6.2.

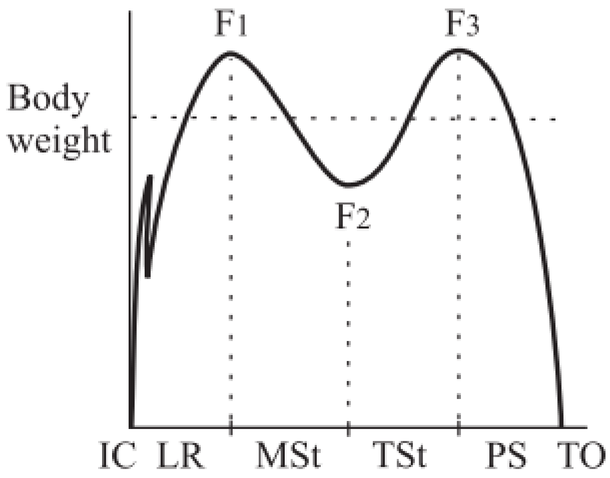

Figure 6.2 Vertical force graph with all five phases of gait occurring during the stance phase (126)

To predict or assess the vibration serviceability of structures under footfall excitation, it is crucial to calculate the vibration response of a structure occupied and dynamically excited by pedestrians. The accuracy of the prediction and assessment relies mainly on the adequate mathematical representation of dynamic loading induced by human motion. Several research results (121, 136, 137) have shown that the vertical loading induced by human motion could be represented by Fourier series, which include a static loading part of individual weight and a sum of harmonic components of dynamic loadings:

$$F_p(t) = G + \sum_{i=1}^{n} G\lambda_i \sin\left(2\pi f_p t + \phi_i\right) \tag{6.1}$$

where, *G* is the static weight of an individual and taken as 746 N according to Ref (138), *i* is the order of the harmonic, n is the total number of harmonics and the Fourier coefficient of the i^{th} harmonic, and f_p is the frequency of repetitive loading (*Hz*), ϕ_i is the phase change of the i^{th} harmonic and λ_i is the Fourier coefficient of the *ith* harmonic generally known as dynamic loading factor (DLF).

DLFs are the Fourier coefficients of the harmonic component and have been investigated by previous studies (139, 140) and incorporated into some design guidelines on the vibration response of civil engineering structures, such as Concrete Society Technical Report 43 Appendix G (CSTR43), Concrete Centre Industry Publication (CCIP-016) and the Steel Construction Institute Publication (SCI P345).

Kerr (139) collected nearly 1000 vertical ground reaction force records, which were single footfall force generated by 40 individuals. The recorded ground reaction forces covered a frequency range from 1 Hz to 3 Hz. The results showed that only the first harmonic of DLF values exhibited a clear trend related to the step rate and the rest of the harmonics were scattered. This study is the most comprehensive database on the ground reaction force induced by human walking available worldwide. It was incorporated into CSTR43 and CCIP-016 as the footfall force for designing and assessing the vibration serviceability of structures under pedestrian loading.

Young (141) collected the data published by Kerr and others and developed more accurate design guidelines on the vibration serviceability of civil engineering structures such as floors and footbridges. SCI (142) derived four harmonics of DLFs based on evaluation of pace frequencies which is widely used by researchers and designers. According to Ref (142) the static weight G is taken as 745 N and the numerical values of the first Four Fourier coefficients λ_i and phase angle ϕ_i are listed in Table 6.1. The generated human walking force model at the walking frequency of 1.8 Hz is shown in Figure 6.3. As discussed, the walking load model applies Fourier coefficients to simulate the continuous ground reaction force induced by human walking activity.

Table 6.1 Parameters for the walking force model (142)

Mode of walking	f_p (Hz)	Numerical coefficient for 1st four harmonics				Phase angle ϕ_i			
		λ_1	λ_2	λ_3	λ_4	ϕ_1	ϕ_2	ϕ_3	ϕ_4
Slow Walk	1.8	0.26	0.1	0.06	0.06				
Normal Walk	2.0	0.26	0.1	0.06	0.06	0	$\pi/2$	$\pi/2$	$\pi/2$
Fast Walk	2.2	0.52	0.1	0.06	0.06				

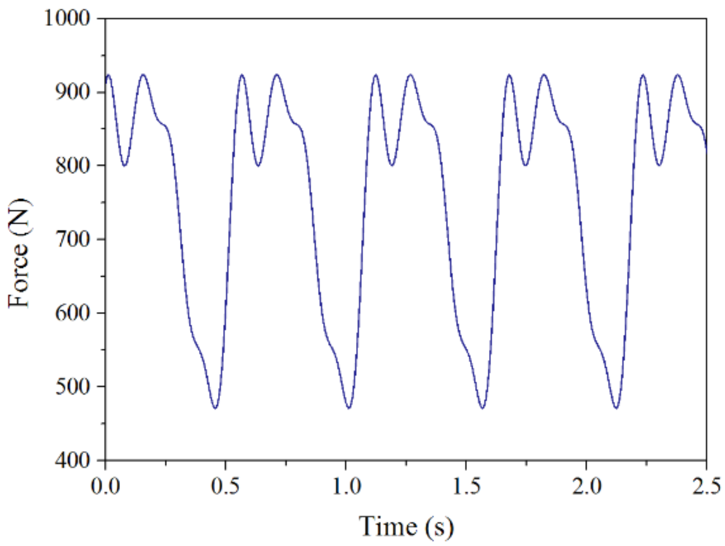

Figure 6.3 Dynamic load function for one-person walking (f_p = 1.8 Hz)

6.3 Structural model

Prefabricated buildings include different types of buildings depending on their production methods. In this study, one type of prefabricated building is chosen to evaluate the vibration serviceability performance of the proposed lightweight sandwich panels.

A composite floor system (143) is adopted in the present study to evaluate the vibration serviceability performance of the proposed lightweight sandwich panels that are applied as floor panels. The composite floor system is subjected to a human walking load and is supported by steel columns. The structural floor system is composed of composite girders and a 150 mm thick concrete slab. The details of the structural system are shown in Figure 6.4 and Figure 6.5. The used beam is VS I550×64, which is 550 mm high and the girder is VS I450×51, with a height of 450 mm. Detailed information regarding the beam and girder can be found in Table 6.2.

The reinforced concrete slab is originally used for the composite floor system. For this study, the reinforced concrete slab is replaced by the developed lightweight sandwich panel. The critical failure load for the lightweight panel can be calculated by Eq. (4.2). The predicted critical failure load is 16 *kPa*, which is larger than the design load (5 *kPa* for office or work areas according to Ref (144)). The vibration serviceability of the structural floor system with the developed sandwich panels is studied using finite element analysis. During the analysis, the length of the floor system L1 is 9 m and the length L2 is 8 m as shown in Figure 6.4.

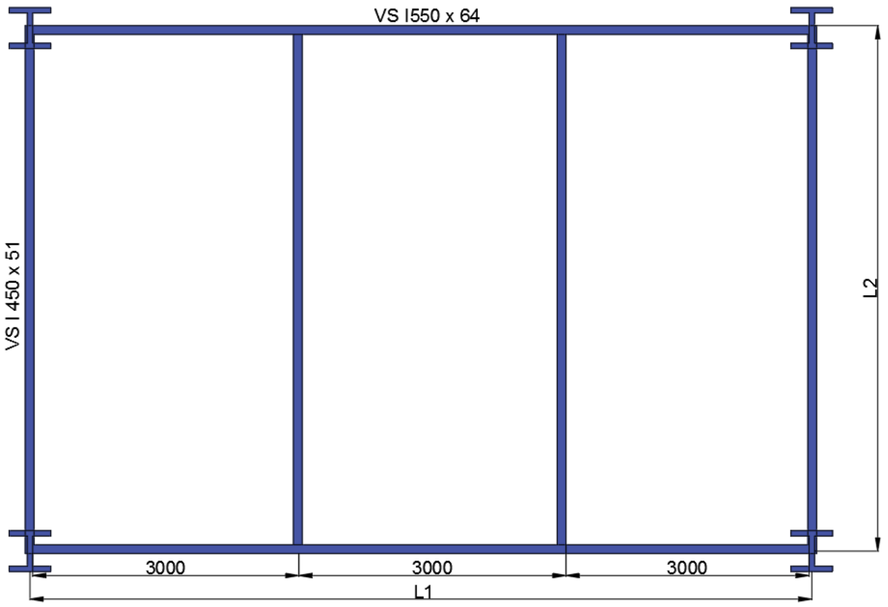

Figure 6.4 Structural floor system layout

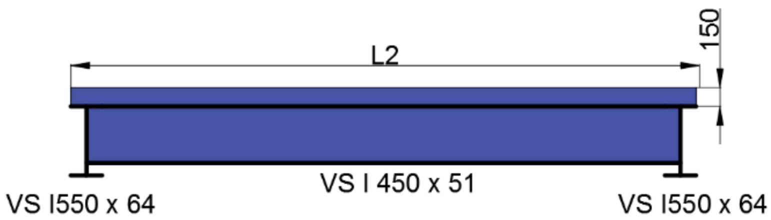

Figure 6.5 Section of the structural floor system

Table 6.2 Detailed dimensions of the components of the structural floor system

Type of structural		Height (mm)	Flange width (mm)	Top flange thickness (mm)	Bottom flange thickness (mm)	Web thickness (mm)
Beam	VS I550 64	550	250	9.5	9.5	6.3
	VS I450 51	450	200	9.5	9.5	6.3
Column	CS I 300 62	300	300	9.5	9.5	6.3

6.4 Finite element model

6.4.1 Damping ratio

The damping model depicts the energy dissipation of a structure. The actual mechanism of the damping in a structure is very complex, and thus is quite difficult to model. One of the most commonly used damping models to simulate the damping mechanism of a structure is Rayleigh damping model. This model represents damping as a function of mass and stiffness; therefore, it is very convenient and simple to apply to the numerical simulation. Rayleigh damping model is expressed as

$$C = \alpha M + \beta K \tag{6.2}$$

where M and K are the mass matrices and stiffness matrices of the structure, respectively; α and β are the damping model coefficients, which can be determined by natural frequency f_r and damping ratio ξ_r of the first two modes with the following equation:

$$\xi_r = \frac{\alpha}{2f_r} + \frac{\beta f_r}{2} \tag{6.3}$$

If damping ratios and frequencies for the first two consecutive modes (m^{th} and n^{th}) are known, α and β can be obtained by solving two simultaneous equation as shown in the following equation:

$$\begin{Bmatrix} \xi_m \\ \xi_n \end{Bmatrix} = \frac{1}{2}\begin{bmatrix} 1/f_m & f_m \\ 1/f_n & f_n \end{bmatrix} \tag{6.4}$$

Damping in the floor system of buildings is very important for its vibration serviceability. Normally, the damping ratio of concrete and steel deck composite floors is within the range from 1.5% to 2% (145-147). In addition, the damping ratio of a conventional floor can be increased by to 4.5% to 6% because of the floor finish, placement of the furniture, and arrangement of the partitioned walls (148, 149). Therefore, the total damping (D) of the entire floor system comes from three different contributions. The first part is the structural damping of the floor structure (D_1), the second part is from the furniture, partition, or equipment (D_2), and the last part is from permanent installations and finishing (D_3). The suggested contribution of different damping parts is shown in Table 6.3 based on ISO 10137. As a result, the effect of damping ratios on the vibration serviceability of the floor system shown in Figure 6.4 are studied. Three different damping scenarios from low to high are considered as shown in Table 6.4. The damping ratio of FD1 is assumed as low damping level and the damping ratio of FD2 represents the medium damping level. The damping ratio of FD3 is obtained by the force hammer impact vibration test in Chapter 5 and represents the high damping level scenario for the composite floor system. The assumed low to high damping level ranges from the damping ratio of 1% to 5% of the composite floor system, which should be able to cover the reasonable damping range of a building structure in service.

Table 6.3 Damping from each structural component

Type	Damping (% of critical damping)
Structural damping D_1	
Concrete	2%
Steel	1%
Composite	1%
Damping due to furniture D_2	
Traditional office for 1 to 3 persons with separation walls	2%
Paperless office	0%
Open-plan office	1%
Library	1%
Houses	1%
Schools	0%
Gymnasium	0%
Damping due to finishing D_3	
Ceiling under floor	1%
Free floating floor	0%
Swimming screed	1%

Table 6.4 Different scenarios for damping ratio for composite floor system

Floor ID	Damping ratio (%)	
	Bending Mode 1	Bending Mode 2
FD1	1	1
FD2	3	3
FD3	5	5.8

6.4.2 Finite element models of the floor system

The commercially available finite element analysis software Abaqus 6.13 is used to build the finite element model of the structural floor system. The columns, beams, and girders are simulated as the beam element (B31) and the developed sandwich floor panel is simulated as the composite shell element (S4R). The material properties used for the finite element analysis are shown in Table 6.5. The Poisson's ratio of PUR foam is taken as 0.3, according to Ref (98). The detailed finite element models are shown in Figure 6.6. The length of the beam element is 50 mm and the size of the shell element is 50 mm × 50 mm. The columns are fixed on the ground and upper level of the building.

Table 6.5 Material properties adopted for the finite element models

	Steel	FRG	PUR foam
Density (*kg/m*^{3})	7600	2000	35
Elastic modulus (*GPa*)	205	13	0.005
Poisson's ratio	0.25	0.3	0.3

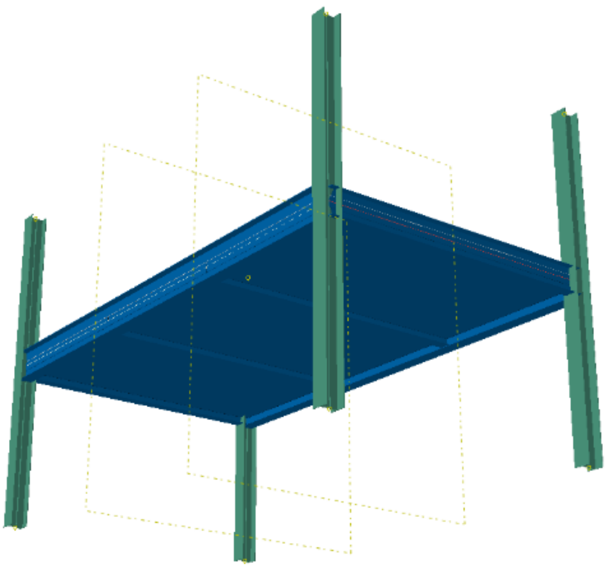

(a)

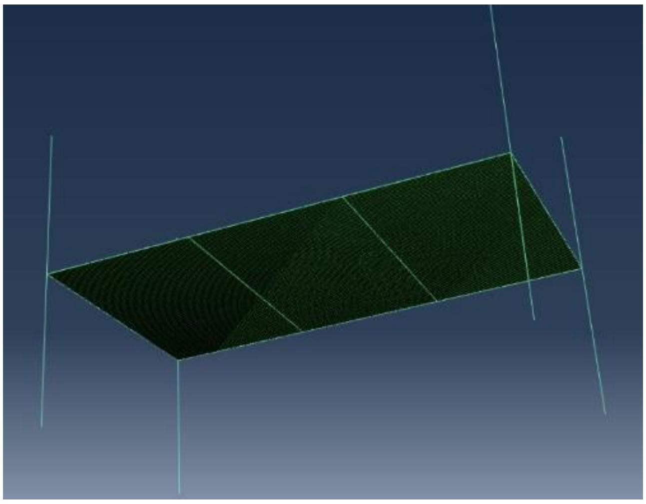

(b)

Figure 6.6 Finite element model: (a) Geometry of floor system; (b) Finite element model

6.5 Finite element model predictions of floor vibrations under pedestrian load and serviceability check

6.5.1 Free vibration analysis of the composite floor system

Modal analysis is conducted by using the finite element model to obtain the modal frequencies of the structural floor systems. The first six modes of floor systems are shown in Figure 6.7. Natural frequencies of the floor systems are shown in Table 6.6. As observed, the fundamental frequency of the composite floor system is 10.12 Hz, which is higher than the highest frequency component of human walking load model (8.8 Hz) show in Table 6.1. It means that resonance will not happen for the composite floor under the applied human walking load model.

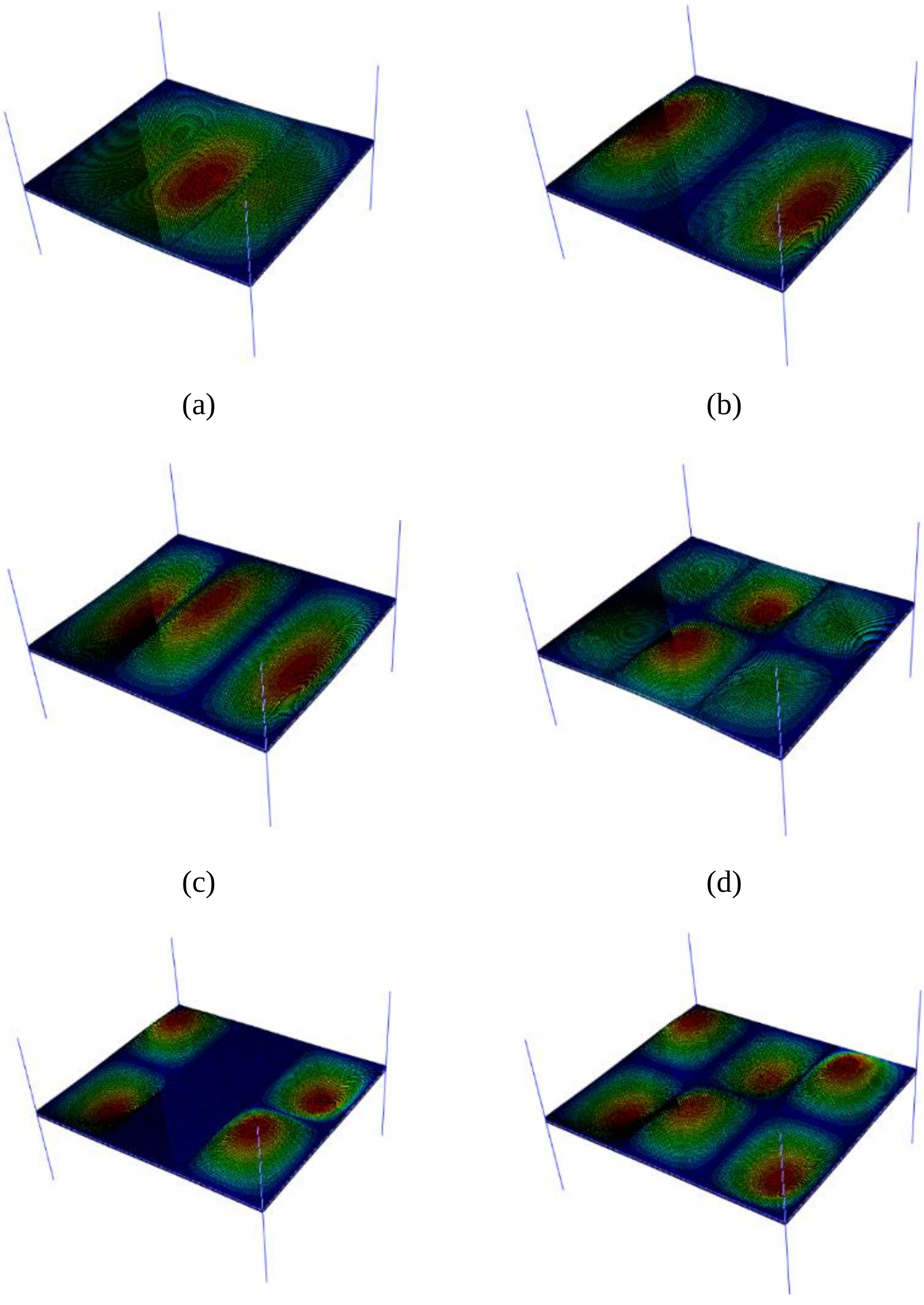

Figure 6.7 The first six vibration modes of the composite floor system: (a) 1st mode; (b) 2nd mode; (c) 3rd mode; (d) 4th mode; (e) 5th mode; (f) 6th mode

Table 6.6 Natural frequencies (Hz) of the composite floor system

L1 (m)	L2 (m)	Mode 1	Mode 2	Mode 3	Mode 4	Mode 5	Mode 6
9	8	10.12	13.35	15.77	17.55	18.84	19.11

6.5.2 Vibration serviceability analysis of the composite floor system with different damping levels

Transit dynamic analysis is performed by Abaqus 6.13 using continuous walking loads to obtain the response of the composite floor system with the developed sandwich panel. The transit dynamic analysis is more appropriate than the steady state analysis of the composite floor system. The acceleration response of building floors due to a single person walking, and a group of people walking with the dynamic distributed loads, are calculated, similar to those in the previous studies (150, 151). The acceleration response at the midspan point is analysed for vibration serviceability evaluation, since the largest amplitude happened at the midspan point of the composite floor system, as presented in a previous study [142].

As discussed in Section 2.3, response of a floor structure can be evaluated in terms of acceleration for the vibration serviceability assessment, in which both the peak acceleration and Root-Mean Square acceleration (a_{rms}) can be used. Peak acceleration is the highest value of acceleration resulting from the excitation on structures. However, it cannot include the influence of the duration of the response. a_{rms} is an average expression of the acceleration time history, and shows a more significant influence on the vibration serviceability than the peak acceleration (142). In addition, the acceleration is also filtered by the weighting method which is given on the comfort baseline of human's perception and this method is widely used by different guidelines as discussed in Section 2.3. Three different walking speeds are used to represent the typical walking activities occurring on the building floor, which are 1.8 Hz, 2.0 Hz, and 2.2 Hz, representing slow walking, normal walking and fast walking, respectively. The acceleration time history from finite element analysis, frequency weighted acceleration and RMS value for the composite floor system with different damping levels (FD1, FD2, and FD3) are shown in Figure 6.8 ~ Figure 6.10, respectively. As observed, the frequency weighted time histories of acceleration are slightly smaller than the original acceleration time history. It is because that the frequency weighting function basically increases the frequency components humans are sensitive and decreases frequency components humans are not sensitive as shown in Figure 2.7. Apparently, the amplitude of original acceleration time history, frequency weighted time history and RMS value increase when the walking frequency increases for the composite floor system with different damping levels FD1, FD2, and FD3.

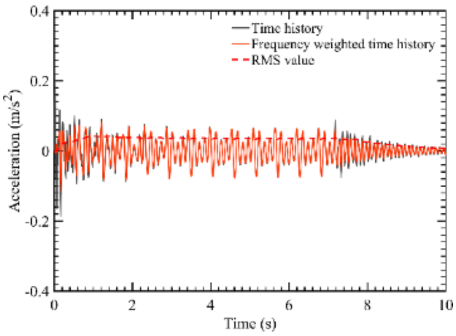

(a)

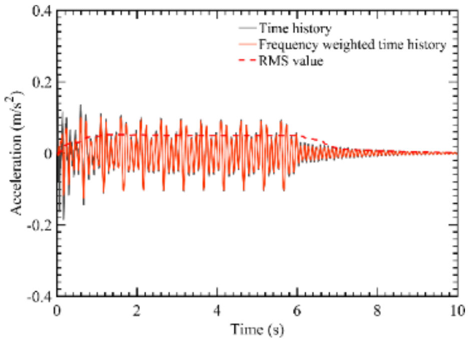

(b)

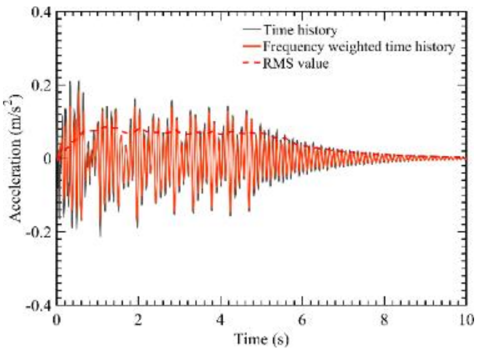

(c)

Figure 6.8 Acceleration history of the FD1: (a) 1.8 Hz; (b) 2.0 Hz; (c) 2.2 Hz

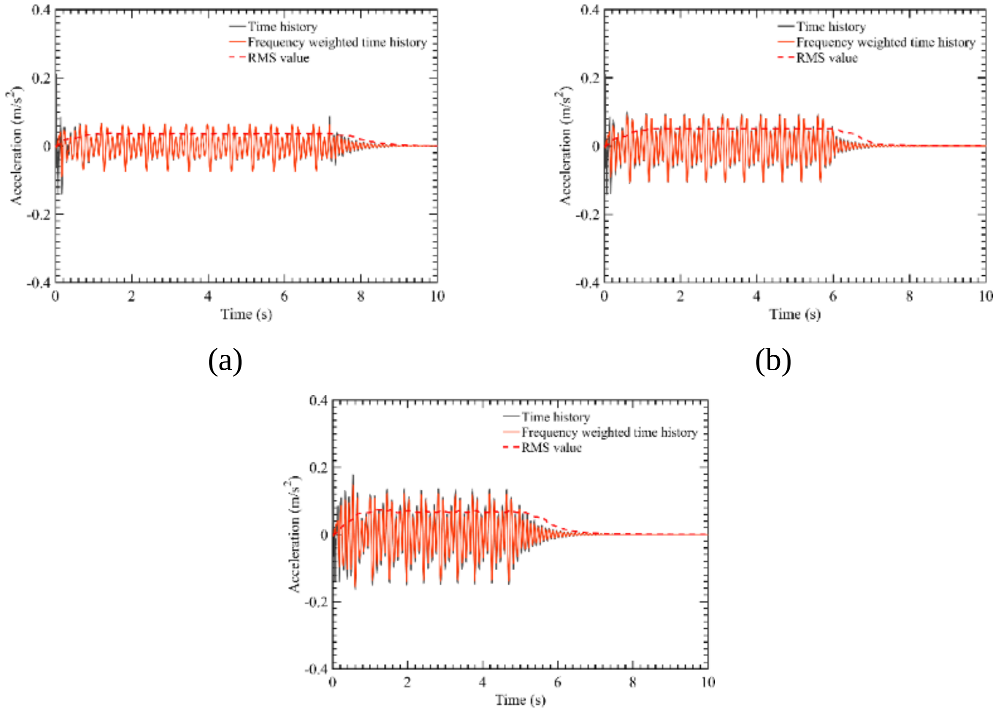

(a) (b)

(c)

Figure 6.9 Acceleration history of the FD2: (a) 1.8 Hz; (b) 2.0 Hz; (c) 2.2 Hz

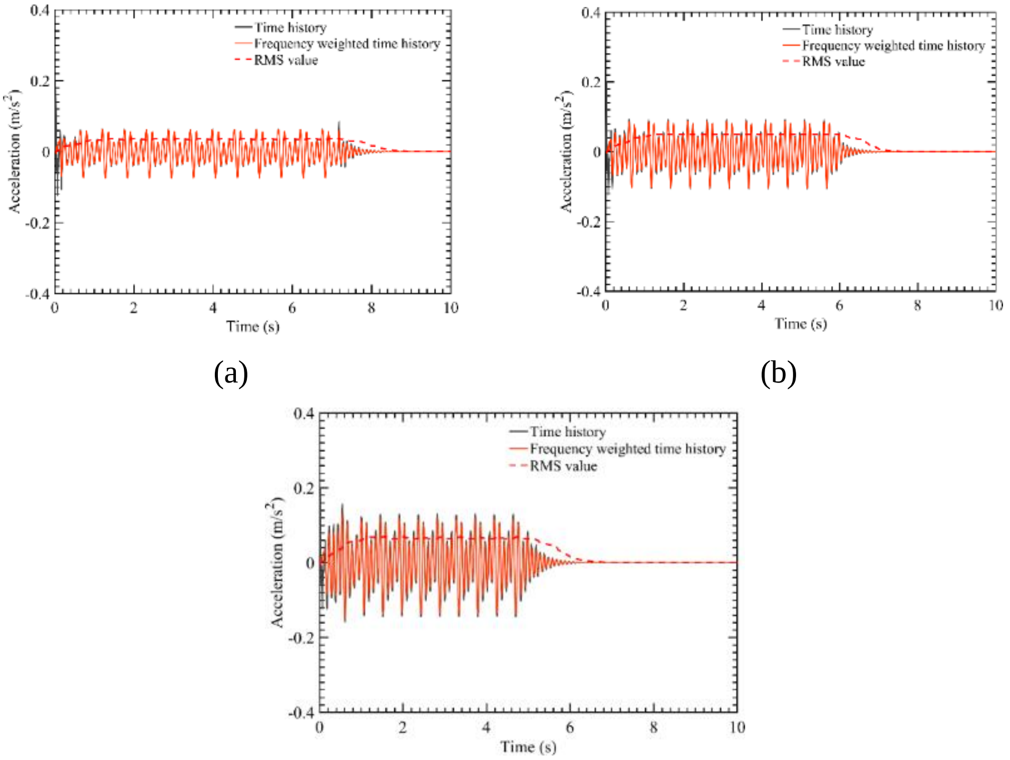

(a) (b)

(c)

Figure 6.10 Acceleration history of the FD3: (a) 1.8 Hz; (b) 2.0 Hz; (c) 2.2 Hz

a_{rms} and *VDV* of acceleration responses are calculated according to Eq. (2.1) and Eq. (2.4) for the composite floor systems with different damping levels FD1, FD2, and FD3. The values of a_{rms} and *VDV*s of the composite floor with different damping levels are shown in Figure 6.11 and Figure 6.12, respectively. The *VDV*s in Figure 6.12 are the vibration dose values of single walking event happened on the composite floor. The overall vibration serviceability assessment results of the composite floor system are shown in Table 6.7. As observed in Figure 6.11 and Figure 6.12, the a_{rms} and *VDV* of composite floor increases when the walking frequency increases from 1.8 Hz to 2.2 Hz. In addition, the value of a_{rms} and *VDV* decreases when the damping level of the composite floor system increases from FD1 to FD3.

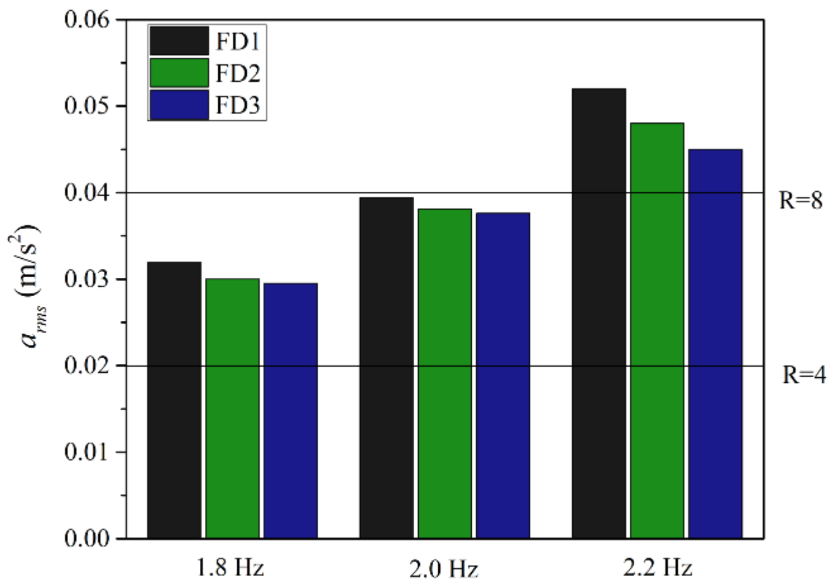

Figure 6.11 a_{rms} result for FD1, FD2, and FD3

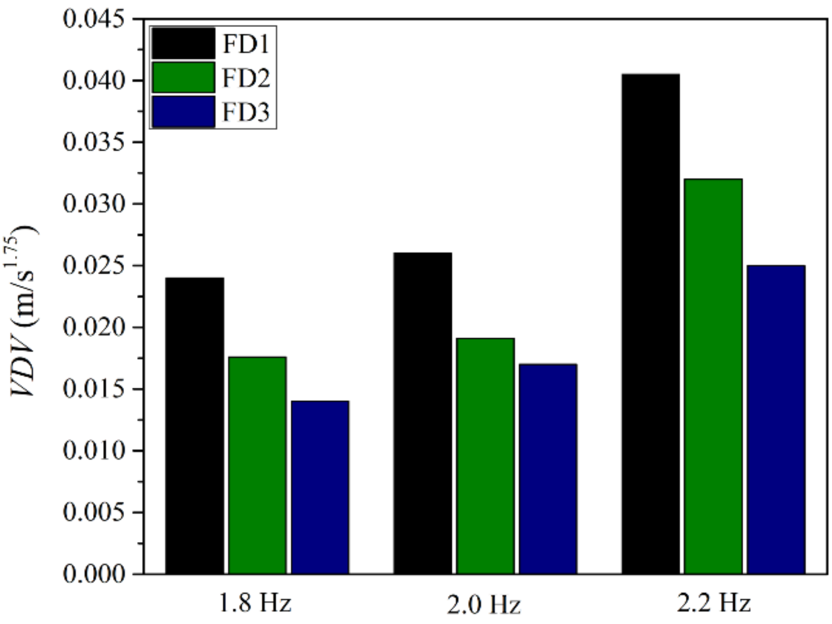

Figure 6.12 VDVs result for FD1, FD2, and FD3

As observed in Figure 6.11, a_{rms} values for composite floor with damping ratio of FD1, FD2, and FD3 subjected to the walking frequency of 1.8 Hz and 2.0 Hz are between response factors of 4 to 8, which indicates good vibration serviceability. However, the a_{rms} values with the walking frequency of 2.2 Hz are higher than 0.04 m/s^2 corresponding to a response factor of 8, which means the vibration serviceability might not be satisfied in terms of a_{rms} criterion. Apparently, vibration serviceability becomes more severe when the walking frequency increases. However, the value of a_{rms} from one single activity of occupants on the floor might not be able to reflect the real vibration serviceability through the whole duration of the use of floor. Furthermore, a_{rms} averages the effect of vibration amplitude through the duration of the walking activity. As a result, total vibration dose values (VDV_t) are suggested to be more reasonable for the assessment of vibration serviceability by serval guidelines since it accumulates the effect of the vibration amplitude through the duration of service of the floors. VDV_t can be calculated by using Eq. (2.4) for the duration of 16 hours on the daytime and the results are shown in Table 6.7 and Figure 6.13. The threshold of VDV_t can be taken as 0.4 m/s$^{1.75}$ for 16 hours on daytime according to Table 2.3. As observed, VDV_t values of FD1, FD2, and FD3 with walking frequencies ranged from 1.8 Hz to 2.2 Hz are smaller than the threshold of VDV_t. It indicates the composite floor system applying developed lightweight sandwich panel with damping levels of FD1, FD2, and FD3 has a good vibration serviceability performance under human walking activities. As shown in Figure 6.13, VDV_t decreases when the damping of the composite floor system increases from FD1 to FD3. It reflects that the damping of the structures can affect the vibration serviceability of the composite floor effectively. Increasing damping of the composite floor system can decrease the VDV_t effectively.

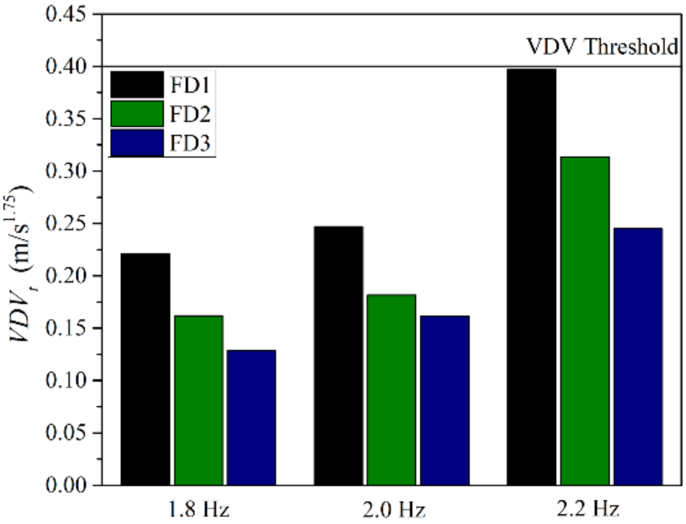

Figure 6.13 VDV_t results for FD1, FD2, and FD3

n_a is the number of event occurrences that might be able to cause vibration serviceability problems and is more straightforward to show the adverse effects of the excessive vibration of floors. n_a can be calculated according to the VDV_t threshold (0.4 m/s$^{1.75}$ for 16 H on daytime according to Table 2.3) by Eq.(2.4). The n_a values are shown based on one minute to make it easier and clearer to assess the possibility of the occurrence of walking activities in Table 6.7. For example, the values of n_a of FD1, FD2, and FD3 with the walking frequency of 2.0 Hz (normal walking speed) are 58/min, 200/min, and 319/min, which are not likely to happen for an office or residential floor. The smallest value of n_a is 10/min corresponding to FD1 under the walking frequency of 2.2 Hz, which means 10 activities per minutes happen and last for 16 hours per day will cause adverse effect of excess vibrations. A single walking activity every minute in an office or residential floor during the day is an unlikely occurrence [142]. As a result, the vibraiton serviceabilty of the composite floor can also be assessed to have a low possbility to cause the adverse effects in terms of the assessment parameter of n_a.

Table 6.7 The vibration serviceability assessment result for the composite floor with different damping levels (FD1, FD2, and FD3)

Floor ID	f_p (Hz)	a_{rms} (m/s^2)	VDV (m/s$^{1.75}$)	VDV_t (m/s$^{1.75}$)	n_a
FD1	1.8	0.0319	0.0240	0.2208	77160 (80/min)
	2.0	0.0394	0.0260	0.2470	566029 (58/min)
	2.2	0.0520	0.0405	0.3969	9515 (10/min)
FD2	1.8	0.0300	0.0176	0.1619	266802 (277/min)
	2.0	0.0381	0.0191	0.1815	192356 (200/min)
	2.2	0.0480	0.0320	0.3136	24414 (25/min)
FD3	1.8	0.0295	0.0140	0.1288	666389 (694/min)
	2.0	0.0376	0.0170	0.1615	306509 (319/min)
	2.2	0.0450	0.0250	0.2450	65536 (68/min)

6.5.3 Vibration serviceability analysis of the composite floor system with different floor lengths (L2)

The influence of the floor length on the vibration serviceability of the composite floor system with the developed lightweight sandwich panel is studied. As shown in Figure 6.4, the floor length L1 is fixed as 9 m long and the floor length L2 is taken as 8 m, 10 m, and 12 m, respectively. Modal analysis is conducted by using the finite element model to obtain the modal frequencies of the structural floor systems. The first six modal frequencies of the analysed composite floor system with L2 equals to 8 m, 10 m, and 12 m are shown in Table 6.8. The vibration frequencies decease when L2 increases from 8 m to 12 m as listed in Table 6.8.

Table 6.8 Natural frequencies of the composite floor system with different floor length

L2 (m)	Mode 1	Mode 2	Mode 3	Mode 4	Mode 5	Mode 6
8	10.12	13.35	15.77	17.55	18.84	19.11
10	8.8	12.2	15.2	16.4	17.8	18.2
12	6.3	9.6	13.4	13.8	15.7	16.7

Transit dynamic analysis is performed by Abaqus 6.13 using continuous walking loads to obtain the response of the composite floor system. Continuous human walking load with the walking frequency equals to 2 Hz representing normal walking speed is considered, and the details of the load model can be found in Eq.(6.1). The damping of the composite floor is considered as high damping level (FD3), since the identified damping of the developed sandwich panel has high damping as presented in Chapter 5. The acceleration time history of the midspan point from finite element analysis, frequency weighted acceleration and RMS value for the studied composite floor system with different floor lengths are shown in Figure 6.14. As observed, the amplitudes of the acceleration time history, frequency weighted time history and RMS value increase when the floor length L2 increases. It is because the composite floor with a larger L2 has a lower fundamental frequency.

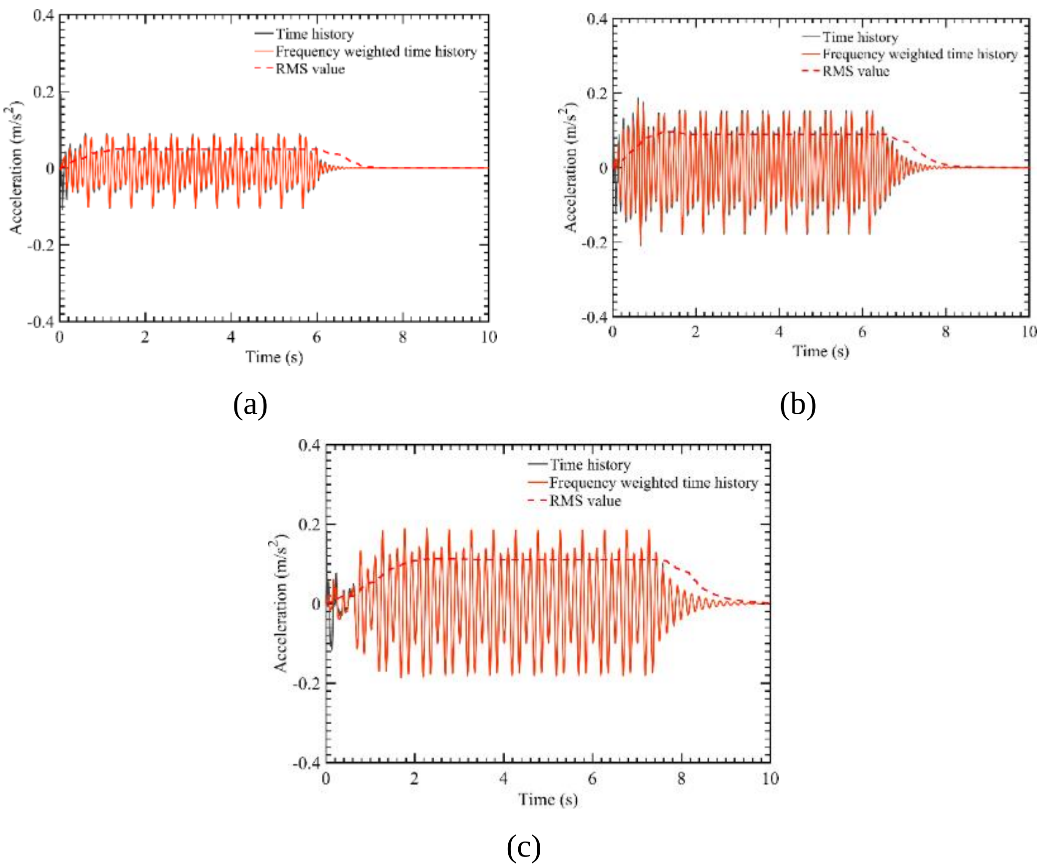

Figure 6.14 Acceleration history of the composite floor system with different length: (a) L2 = 8 m; (b) L2 = 10 m; (c) L2 = 12m

The vibration assessment results based on the vibration dose values for the composite floor with different length (L2) are shown in Table 6.9. VDV_t is calculated based on the VDV of the composite floor with the walking frequency equal to 2 Hz for 16 hours duration at daytime and the results are also shown in Figure 6.15. As observed, the VDV_t of the composite floor increases when L2 increase from 8 m to 12 m. The higher value of VDV_t indicates the composite floor with larger L2 is more likely to have the vibration serviceability problem. The VDV_t for the composite floor with L2 equal to 8 m, 10 m, and 12 m are all smaller than the VDV threshold (0.4 m/s$^{1.75}$), indicating the composite floor has good vibration serviceability even when L2 increases to 12 m. The smallest value of n_a is 33/min for the composite floor with the length of L2 equal to 12 m under a normal walking speed, which means it needs 33 times of walking per minute and last for 16 hours in the daytime to cause the adverse comments of the vibration serviceability.

Table 6.9 Vibration serviceability assessment results of the composite floor with different floor length

Floor length L2 (m)	f_p (Hz)	a_{rms} (m/s^2)	VDV (m/s$^{1.75}$)	VDV_t (m/s$^{1.75}$)	n_a
8	2.0	0.0376	0.017	0.16	306509 (319/min)
10		0.0724	0.025	0.24	65536 (68/min)
12		0.091	0.033	0.31	31604 (33/min)

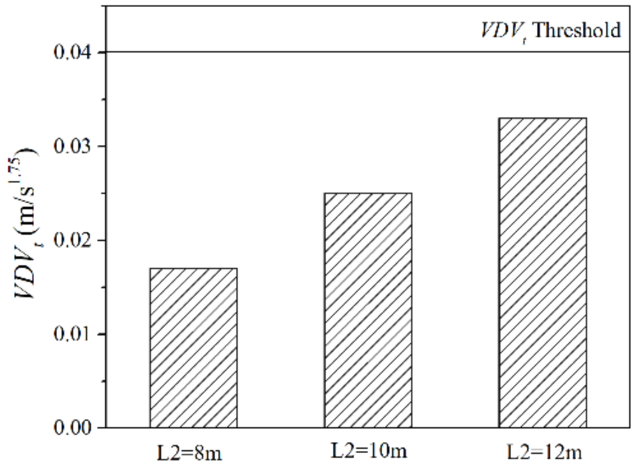

Figure 6.15 VDV_t of the composite floor with different floor length L2

6.6 Summary

This chapter investigates the vibration serviceability of a composite floor system of a prefabricated building with the developed sandwich panel under human walking activity. The sandwich panel tested in Chapter 5 is used as floor and subjected to walking loads. First, the vibration serviceability of the composite floor with different damping levels under continuous walking load is studied. The vibration serviceability is assessed in terms of the different vibration assessment parameters based on a_{rms} and

VDVs. Then, the influence of the composite floor length on the vibration serviceability is studied. The research results of this chapter show that the fundamental frequency of the composite floor system is higher than the dominant frequencies of the dynamic loads induced by human activities, so the resonance does not happen. a_{rms} and VDV values for the composite floor system with different damping levels increase when the walking frequencies increase from 1.8 Hz to 2.2 Hz, and a_{rms} and VDV decrease when the damping level of the composite floor increases from FD1 to FD3. The vibration serviceability of the composite floor satisfies the serviceability criteria in terms of the vibration dose value VDV_t. The finite element analysis results show that increasing the length of the composite floor system up to 12 m can still meet the serviceability criteria according to the VDV_t.

7 Conclusions and recommendations

7.1 Conclusions

This thesis develops a new type of lightweight sandwich panel for prefabricated buildings considering the eco-design for sustainability. This panel is made from FRG composite skin layers with a PUR foam core. The mechanical properties and vibration characteristics of the FRG as the skin layers for the developed sandwich panel are studied by quasi-static tests and hammer impact vibration tests in Chapter 3. The influence of methylcellulose on the mechanical properties and vibration characteristics of GP and FRG are studied. The inclusion of CS and HSPE fibres successfully changes the damage pattern from brittle to ductile. The addition of the fibres effectively suppresses the development of multiple micro-cracks of GP under quasi-static compressive loads. Adding methylcellulose is beneficial for increasing not only the load bearing capacity of GP and FRG but also the ductility of FRG. As indicated by the toughness and the toughness indices, the FRG developed in the present study has a good energy absorption capacity. Adding methylcellulose to the FRG enhances its toughness and toughness indices. Adding methylcellulose slightly decreases the SMOE and DMOE of both the GP and FRG and increased their damping ratios.

The failure mechanisms of the sandwich panel under point loading and edgewise compression test are studied using the DIC method in Chapter 4. The core shear failure modes of the developed sandwich panels change with the thickness-to-span ratios. The failure mode changes from 45° shear crack to delamination between the FRG skin and PUR foam when the *c/L* changed from 0.1 to 0.3. The sandwich panel with PUR foam core of higher density (96 kg/m^3) experiences skin tensile failure. The analytical models for predicting the critical failure load for the sandwich panel are proposed, and the results match reasonably well with the experimental results. The failure mode of sandwich panel under edgewise compressive load changes from the skin shear failure to global buckling, when *c/L* changed from 1 to 0.33. The analytical models for predicting the critical failure load under edgewise compressive load are proposed and give reasonable predictions as compared with the experimental results.

The structural performance and vibration characteristics of the full-size sandwich panel are studied in Chapter 5. Two types of sandwich panels are considered for flexural loading test. The first type (S1) applies the FRG as the skin layers and the PUR foam as the core layer. The second type (S2) is S1 strengthened with BFRP sheets on the bottom layer of the FRG skin. The BFRP sheet attached to the bottom skin layer of the developed sandwich panel changes the failure mode from skin tensile failure to foam core shear failure. The addition of the BFRP sheet effectively increases the critical failure load by about 26%. In addition, the structural performance of the sandwich panel without strengthening under axial compression loading is studied. The failure mode is global buckling. The forced hammer impact vibration test results show that the natural frequencies and modal damping of the identified first three modes are very close for S1 and S2, indicating that the applied BFRP sheet does not change the vibration characteristics significantly. The finite element analysis by using the solid element and equivalent shell element can obtain the modal information of the sandwich panels accurately, but using the shell elements is much more efficient than solid element in terms of calculation time.

The vibration serviceability of a composite floor system of a prefabricated building with the developed sandwich panels under human walking activity is investigated in Chapter 6. The fundamental frequency of the composite floor system is higher than the dominant frequencies of the dynamic loads induced by human activities, therefore the resonance does not happen. The vibration serviceability of the composite floor satisfies the vibration serviceability criteria defined in terms of the vibration dose value VDV_t. Higher damping levels of the composite floor system are beneficial for the vibration serviceability. The finite element analysis results show that the floor length increased up to 12 m can still have good vibration serviceability in terms of VDV_t.

Overall, an innovative lightweight sandwich panel system is developed by this research for prefabricated buildings. The sandwich panel system includes FRG skins and PUR foam core. It has good mechanical properties and reasonable vibration serviceability, light weight and low cost, therefore great potentials for application in prefabricated structures.

7.2 Future research recommendations

Based on the experiences and results obtained from the present study, the following suggestions are made for future research.

The present study only considers the structural behaviour under bending moment and compressive load of the composite panel. The connection between two prefabricated lightweight sandwich panels or the connection of the developed lightweight sandwich panel with other structural components such as beams or girders and frames are not fully investigated. In reality, the developed sandwich panel would be applied with conjunct panels and other components. Therefore, the structural performance of the developed sandwich panel with connections should be considered for future study.

In addition, only bending moment and compressive load are considered in the present study. A combination of different loading conditions, as well as extreme loading conditions should be considered for future studies. For example, windborne debris impact is considered as an extreme loading condition for buildings in Australia. Therefore, studies on the performance of the developed lightweight sandwich panels under windborne debris impact load should be conducted.

In addition, the present study only examines a basic type of sandwich structure. The FRG skin layer and the PUR foam core layer are assembled by using epoxy resin. It has been reported that the application of shear keys can increase the structural performance of sandwich panels. Therefore, different types of sandwich panels using various shear keys could be developed and their performance under different loading conditions could be studied.

Reference

1. Boafo FE, Kim J-H, Kim J-T. Performance of modular prefabricated architecture: case study-based review and future pathways. Sustainability. 2016;8(6):558.
2. Gunawardena T. Behaviour of prefabricated modular buildings subjected to lateral loads 2016.
3. La Rosa AD, Recca A, Gagliano A, Summerscales J, Latteri A, Cozzo G, et al. Environmental impacts and thermal insulation performance of innovative composite solutions for building applications. Construction and Building Materials. 2014;55:406-14.
4. Programme UNE. Environment for development, available at http://www.unep.org/sbci/AboutSBCI/Background.asp. [Available from: http://www.unep.org/sbci/AboutSBCI/Background.asp.
5. Energy USDo. Building energy data book, available at http: //buildingsdatabook.eren.doe.gov/ChapterIntro1.aspx. [
6. Commission E. data available at http://ec.europa.eu/energy/en/topics/energy-efficiency/buildings; [
7. Directive 2010/31/EU of the European Parliament and of the Council of 19 May 2010 on the energy performance of building [
8. Directive 2012/27/EU of the European Parliament and of the Council of 25 October 2012 on energy efficiency, amending Directives 2009/125/EC and 2010/30/EU and repealing Directives 2004/8/EC and 2006/32/EC Text with EEA relevance. [
9. Board ABC. Building Code of Australia (BCA) 2011. Australia2011.
10. Energy ECE. Transport and GHG Emissions, Trends to 2050 (Reference Scenario (2013)) [
11. Asdrubali F, D'Alessandro F, Schiavoni S. A review of unconventional sustainable building insulation materials. Sustainable Materials and Technologies. 2015;4:1-17.
12. Alam M, Singh H, Limbachiya M. Vacuum Insulation Panels (VIPs) for building construction industry–A review of the contemporary developments and future directions. Applied energy. 2011;88(11):3592-602.
13. Nyers J, Kajtar L, Tomić S, Nyers A. Investment-savings method for energy-economic optimization of external wall thermal insulation thickness. Energy and Buildings. 2015;86:268-74.
14. Al-Homoud DMS. Performance characteristics and practical applications of common building thermal insulation materials. Building and Environment. 2005;40(3):353-66.
15. Jelle BP. Traditional, state-of-the-art and future thermal building insulation materials and solutions – Properties, requirements and possibilities. Energy and Buildings. 2011;43(10):2549-63.
16. Pan Z, Feng KN, Gong K, Zou B, Korayem AH, Sanjayan J, et al. Damping and microstructure of fly ash-based geopolymers. Journal of Materials Science. 2012;48(8):3128-37.

17. Benhelal E, Zahedi G, Shamsaei E, Bahadori A. Global strategies and potentials to curb CO2 emissions in cement industry. Journal of cleaner production. 2013;51:142-61.
18. Noushini A, Hastings M, Castel A, Aslani F. Mechanical and flexural performance of synthetic fibre reinforced geopolymer concrete. Construction and Building Materials. 2018;186:454-75.
19. Jaillon L, Poon CS. The evolution of prefabricated residential building systems in Hong Kong: A review of the public and the private sector. Automation in Construction. 2009;18(3):239-48.
20. Richard R-B. Industrialised building systems: reproduction before automation and robotics. Automation in construction. 2005;14(4):442-51.
21. Tam VWY, Tam CM, Zeng SX, Ng WCY. Towards adoption of prefabrication in construction. Building and Environment. 2007;42(10):3642-54.
22. Badir YF, Kadir MA, Hashim AH. Industrialized building systems construction in Malaysia. Journal of architectural engineering. 2002;8(1):19-23.
23. Mastali M, Valente IB, Barros JAO, Gonçalves DMF. Development of innovative hybrid sandwich panel slabs: Experimental results. Composite Structures. 2015;133:476-98.
24. Shams A, Stark A, Hoogen F, Hegger J, Schneider H. Innovative sandwich structures made of high performance concrete and foamed polyurethane. Composite Structures. 2015;121:271-9.
25. Shams A, Horstmann M, Hegger J. Experimental investigations on Textile-Reinforced Concrete (TRC) sandwich sections. Composite Structures. 2014;118:643-53.
26. Shams A, Hegger J, Horstmann M. An analytical model for sandwich panels made of textile-reinforced concrete. Construction and Building Materials. 2014;64:451-9.
27. Mousa MA, Uddin N. Structural behavior and modeling of full-scale composite structural insulated wall panels. Engineering Structures. 2012;41:320-34.
28. Abdolpour H, Garzón-Roca J, Escusa G, Sena-Cruz JM, Barros JAO, Valente IB. Development of a composite prototype with GFRP profiles and sandwich panels used as a floor module of an emergency house. Composite Structures. 2016;153:81-95.
29. Smakosz Ł, Tejchman J. Evaluation of strength, deformability and failure mode of composite structural insulated panels. Materials & Design (1980-2015). 2014;54:1068-82.
30. Estrada-Martínez S, Mollón V, Bonhomme J. Improvements to the procedure for flexural testing, on two spans, of full wood-based sandwich panel subject to uniform load. Construction and Building Materials. 2016;102:281-96.
31. Williams Portal N, Flansbjer M, Zandi K, Wlasak L, Malaga K. Bending behaviour of novel Textile Reinforced Concrete-foamed concrete (TRC-FC) sandwich elements. Composite Structures. 2017;177:104-18.
32. Shaikh FUA. Review of mechanical properties of short fibre reinforced geopolymer composites. Construction and Building Materials. 2013;43:37-49.
33. Hardjito D, Rangan BV. Development and properties of low-calcium fly ash-based geopolymer concrete. 2005.
34. Nath P, Sarker PK. Effect of GGBFS on setting, workability and early strength properties of fly ash geopolymer concrete cured in ambient condition. Construction and Building materials. 2014;66:163-71.

35. Pan Z, Sanjayan JG, Kong DL. Effect of aggregate size on spalling of geopolymer and Portland cement concretes subjected to elevated temperatures. Construction and Building Materials. 2012;36:365-72.
36. Thokchom S, Ghosh P, Ghosh S. Performance of fly ash based geopolymer mortars in sulphate solution. Journal of engineering science and technology review. 2010;3(1):36-40.
37. Khan MZN, Shaikh FuA, Hao Y, Hao H. Synthesis of high strength ambient cured geopolymer composite by using low calcium fly ash. Construction and Building Materials. 2016;125:809-20.
38. Timakul P, Rattanaprasit W, Aungkavattana P. Improving compressive strength of fly ash-based geopolymer composites by basalt fibers addition. Ceramics International. 2016;42(5):6288-95.
39. Habel K, Viviani M, Denarié E, Brühwiler E. Development of the mechanical properties of an ultra-high performance fiber reinforced concrete (UHPFRC). Cement and Concrete Research. 2006;36(7):1362-70.
40. Hao Y, Hao H. Dynamic compressive behaviour of spiral steel fibre reinforced concrete in split Hopkinson pressure bar tests. Construction and Building Materials. 2013;48:521-32.
41. Banthia N, Nandakumar N. Crack growth resistance of hybrid fiber reinforced cement composites. Cement and Concrete Composites. 2003;25(1):3-9.
42. Bernal S, De Gutierrez R, Delvasto S, Rodriguez E. Performance of an alkali-activated slag concrete reinforced with steel fibers. Construction and building Materials. 2010;24(2):208-14.
43. Ranjbar N, Mehrali M, Mehrali M, Alengaram UJ, Jumaat MZ. High tensile strength fly ash based geopolymer composite using copper coated micro steel fiber. Construction and building materials. 2016;112:629-38.
44. Yan S, He P, Jia D, Yang Z, Duan X, Wang S, et al. Effect of fiber content on the microstructure and mechanical properties of carbon fiber felt reinforced geopolymer composites. Ceramics International. 2016;42(6):7837-43.
45. Yu R, Spiesz P, Brouwers H. Development of an eco-friendly Ultra-High Performance Concrete (UHPC) with efficient cement and mineral admixtures uses. Cement and Concrete Composites. 2015;55:383-94.
46. Aydın S, Baradan B. The effect of fiber properties on high performance alkali-activated slag/silica fume mortars. Composites Part B: Engineering. 2013;45(1):63-9.
47. Lin T, Jia D, He P, Wang M, Liang D. Effects of fiber length on mechanical properties and fracture behavior of short carbon fiber reinforced geopolymer matrix composites. Materials Science and Engineering: A. 2008;497(1-2):181-5.
48. Provis JL, Duxson P, van Deventer JS. The role of particle technology in developing sustainable construction materials. Advanced Powder Technology. 2010;21(1):2-7.
49. Banthia N, Bindiganavile V, Jones J, Novak J. Fiber-reinforced concrete in precast concrete applications: Research leads to innovative products. PCI journal. 2012;57(3).
50. Alomayri T, Shaikh F, Low IM. Synthesis and mechanical properties of cotton fabric reinforced geopolymer composites. Composites Part B: Engineering. 2014;60:36-42.
51. Chen R, Ahmari S, Zhang L. Utilization of sweet sorghum fiber to reinforce fly ash-based geopolymer. Journal of Materials Science. 2014;49(6):2548-58.
52. Shaikh F. Deflection hardening behaviour of short fibre reinforced fly ash based geopolymer composites. Materials & Design. 2013;50:674-82.

53. Nematollahi B, Sanjayan J, Ahmed Shaikh FU. Tensile strain hardening behavior of PVA fiber-reinforced engineered geopolymer composite. Journal of Materials in Civil Engineering. 2015;27(10):04015001.
54. Ferone C, Roviello G, Colangelo F, Cioffi R, Tarallo O. Novel hybrid organic-geopolymer materials. Applied Clay Science. 2013;73:42-50.
55. Hussain M, Varely R, Cheng Y, Mathys Z, Simon G. Synthesis and thermal behavior of inorganic–organic hybrid geopolymer composites. Journal of applied polymer science. 2005;96(1):112-21.
56. Kong X-M, Wu C-C, Zhang Y-R, Li J-L. Polymer-modified mortar with a gradient polymer distribution: preparation, permeability, and mechanical behaviour. Construction and Building Materials. 2013;38:195-203.
57. Lee NK, Kim EM, Lee HK. Mechanical properties and setting characteristics of geopolymer mortar using styrene-butadiene (SB) latex. Construction and Building Materials. 2016;113:264-72.
58. Colangelo F, Roviello G, Ricciotti L, Ferone C, Cioffi R. Preparation and characterization of new geopolymer-epoxy resin hybrid mortars. Materials. 2013;6(7):2989-3006.
59. Gao J, Wang Z, Zhang T, Zhou L. Dispersion of carbon fibers in cement-based composites with different mixing methods. Construction and Building Materials. 2017;134:220-7.
60. Akbar AY, Lestari Y, Ramadhan G, Candra SA, Sugiarti E. The influence of carboxy methyl cellulose (CMC) and solution pH on carbon fiber dispersion in white cement matrix. Applied Mechanics and Materials. 2014;493:661-5.
61. Fu X, Chung D. Improving the bond strength of concrete to reinforcement by adding methylcellulose to concrete. ACI Materials Journal. 1998;95:601-8.
62. Setareh M. Vibration serviceability of a building floor structure. II: Vibration evaluation and assessment. Journal of Performance of Constructed Facilities. 2010;24(6):508-18.
63. (ISO) IOfS. Mechanical vibration and shock - Evaluation of human exposure to whole body vibration - Part 1: General requirements,ISO 2631-1, 2nd Ed. Geneva1997.
64. (ISO) IOfS. Mechanical vibration and shock—Evaluation of human exposure to whole-body vibration—Part 2: Vibration in buildings (1 Hz to 80 Hz). ISO 2631-2, 2nd Ed. Geneva2003.
65. Organization IS. Bases for design of structures - serviceability of buildings and walkways against vibrations. ISO 10137; 2007.
66. (BSI) BSI. Measurement and evaluation of human exposure to whole-body mechanical vibration and repeated shock. BS 6841. London1987.
67. (BSI) BSI. Guide to evaluation of human exposure to vibration in buildings - Part 1: Vibration soures other than blasting. BS 6472-1. London2008.
68. Rasmussen G. Human body vibration exposure and its measurement. The Journal of the Acoustical Society of America. 1983;73(6):2229-.
69. Griffin M. Predicting the feeling of vibration in buildings. Proceedings of the Institute of Acoustics. 2007;29(2):15pp.
70. Rijal R, Samali B, Shrestha R, Crews K. Experimental and analytical study on dynamic performance of timber floor modules (timber beams). Construction and Building Materials. 2016;122:391-9.
71. Ellis B. Serviceability evaluation of floor vibration induced by walking loads. Structural Engineer. 2001.

72. ASTM C618-12a. Standard specification for coal fly ash and raw or calcined natural pozzolan for use in concrete. ASTM International, 2012.
73. ASTM C109. Standard test method for compressive strength of hydraulic cement mortars. ASTM International, 2008.
74. Shaikh FUA. Deflection hardening behaviour of short fibre reinforced fly ash based geopolymer composites. Materials & Design. 2013;50:674-82.
75. ASTM C1609. Standard test method for flexural performance of fiber-reinforced concrete (using beam with third-point loading). ASTM international, 2012.
76. ASTM C215. Standard Test Method for Fundamental Transverse, Longitudinal, and Torsional Resonant Frequencies of Concrete Specimens. Standard Test Method for Fundamental Transverse, Longitudinal, and Torsional Resonant Frequencies of Concrete Specimens," ASTM International, 2008.
77. Magalhães F, Cunha Á, Caetano E, Brincker R. Damping estimation using free decays and ambient vibration tests. Mechanical Systems and Signal Processing. 2010;24(5):1274-90.
78. Noushini A, Samali B, Vessalas K. Effect of polyvinyl alcohol (PVA) fibre on dynamic and material properties of fibre reinforced concrete. Construction and Building Materials. 2013;49:374-83.
79. Mishra PC, Singh VK, Narang KK, Singh NK. Effect of carboxymethyl-cellulose on the properties of cement. Materials Science and Engineering: A. 2003;357(1):13-9.
80. Liu W, Zhang J, Rethore G, Khairoun K, Pilet P, Tancret F, et al. A novel injectable, cohesive and toughened Si-HPMC (silanized-hydroxypropyl methylcellulose) composite calcium phosphate cement for bone substitution. Acta Biomaterialia. 2014;10(7):3335-45.
81. Bashar II, Alengaram UJ, Jumaat MZ, Islam A, Santhi H, Sharmin A. Engineering properties and fracture behaviour of high volume palm oil fuel ash based fibre reinforced geopolymer concrete. Construction and Building Materials. 2016;111:286-97.
82. Gao J, Sun W, Morino K. Mechanical properties of steel fiber-reinforced, high-strength, lightweight concrete. Cement and Concrete Composites. 1997;19(4):307-13.
83. Desbrières J, Hirrien M, Ross-Murphy SB. Thermogelation of methylcellulose: rheological considerations. Polymer. 2000;41(7):2451-61.
84. Khan MZN, Hao Y, Hao H, Shaikh FUA. Mechanical properties of ambient cured high strength hybrid steel and synthetic fibers reinforced geopolymer composites. Cement and Concrete Composites. 2018;85:133-52.
85. Khan MZN, Hao Y, Hao H, Shaikh FUA, Liu K. Mechanical properties of ambient cured high-strength plain and hybrid fiber reinforced geopolymer composites from triaxial compressive tests. Construction and Building Materials. 2018;185:338-53.
86. Nematollahi B, Sanjayan J, Shaikh FUA. Comparative deflection hardening behavior of short fiber reinforced geopolymer composites. Construction and Building Materials. 2014;70:54-64.
87. joo Kim D, Naaman AE, El-Tawil S. Comparative flexural behavior of four fiber reinforced cementitious composites. Cement and concrete Composites. 2008;30(10):917-28.
88. ASTM C1018. Standard Test Method for Flexural Toughness and First-Crack Strength of Fiber-Reinforced Concrete (withdrawn 2006)1997: ASTM International.

89. Naaman A, Reinhardt H, editors. Characterization of high performance fiber reinforced cement composites—HPFRCC. High performance fiber reinforced cement composites; 1995.
90. Banghai J, Zhibin L, Fangyun L. Failure mechanism of sandwich beams subjected to three-point bending. Composite Structures. 2015;133:739-45.
91. McCormack TM, Miller R, Kesler O, Gibson LJ. Failure of sandwich beams with metallic foam cores. International Journal of Solids and Structures. 2001;38(28):4901-20.
92. Triantafillou TC, Gibson LJ. Failure mode maps for foam core sandwich beams. Materials Science and Engineering. 1987;95:37-53.
93. Lei H, Yao K, Wen W, Zhou H, Fang D. Experimental and numerical investigation on the crushing behavior of sandwich composite under edgewise compression loading. Composites Part B: Engineering. 2016;94:34-44.
94. Cote F, Biagi R, Bart-Smith H, Deshpande VS. Structural response of pyramidal core sandwich columns. International Journal of Solids and Structures. 2007;44(10):3533-56.
95. Zhang Z, Richardson M. Visualisation of barely visible impact damage in polymer matrix composites using an optical deformation and strain measurement system (ODSMS). Composites Part A: Applied Science and Manufacturing. 2005;36(8):1073-8.
96. Blaber J, Adair B, Antoniou A. Ncorr: open-source 2D digital image correlation matlab software. Experimental Mechanics. 2015;55(6):1105-22.
97. Fathi A, Keller J-H, Altstaedt V. Full-field shear analyses of sandwich core materials using Digital Image Correlation (DIC). Composites Part B: Engineering. 2015;70:156-66.
98. Abeysinghe CM, Thambiratnam DP, Perera NJ. Dynamic performance characteristics of an innovative Hybrid Composite Floor Plate System under human-induced loads. Composite Structures. 2013;96:590-600.
99. Naaman AE, Reinhardt H-W. Proposed classification of HPFRC composites based on their tensile response. Materials and structures. 2006;39(5):547-55.
100. ASTM C618-12a, Standard specification for coal fly ash and raw or calcined natural pozzolan for use in concrete. ASTM International, 2012.
101. Chen W, Pham TM, Sichembe H, Chen L, Hao H. Experimental study of flexural behaviour of RC beams strengthened by longitudinal and U-shaped basalt FRP sheet. Composites Part B: Engineering. 2018;134:114-26.
102. ASTM C39. Standard test method for compressive strength of cylindrical concrete specimens. ASTM International, 2012.
103. ASTM C 469, Standard test method for static modulus of elasticity and Poisson's ratio of concrete in compression. ASTM International, 2002.
104. Wille K, El-Tawil S, Naaman AE. Properties of strain hardening ultra high performance fiber reinforced concrete (UHP-FRC) under direct tensile loading. Cement and Concrete Composites. 2014;48:53-66.
105. ASTM C1609/1609M. Standard test method for flexural performance of fiber-reinforced concrete (Using beam with third point loading). ASTM Interantional, 2012.
106. ASTM D7249/7249M. Standard test method for facing properties of sandwich constructions by long beam flexure. ASTM International, 2006.
107. ASTM C364/C364M. Standard test method for edgewise compressive strength of sandwich constructions. ASTM International, 2007.

108. Junes A, Si Larbi A. An indirect non-linear approach for the analysis of sandwich panels with TRC facings. Construction and Building Materials. 2016;112:406-15.
109. Allen HG. Analysis and design of structural sandwich panels: the commonwealth and international library: structures and solid body mechanics division: Elsevier; 2013.
110. Harte AM, Fleck NA, Ashby MF. Sandwich panel design using aluminum alloy foam. Advanced Engineering Materials. 2000;2(4):219-22.
111. Fleck NA, Sridhar I. End compression of sandwich columns. Composites Part A: applied science and manufacturing. 2002;33(3):353-9.
112. Yang B, Wang Z, Zhou L, Zhang J, Tong L, Liang W. Study on the low-velocity impact response and CAI behavior of foam-filled sandwich panels with hybrid facesheet. Composite structures. 2015;132:1129-40.
113. Gdoutos E, Daniel IM, Wang K-A. Compression facing wrinkling of composite sandwich structures. Mechanics of materials. 2003;35(3-6):511-22.
114. Leone M, Centonze G, Colonna D, Micelli F, Aiello M. Fiber-reinforced concrete with low content of recycled steel fiber: Shear behaviour. Construction and Building Materials. 2018;161:141-55.
115. Lee B-C, Lee K-W, Byun J-H, Kang K-J. The compressive response of new composite truss cores. Composites Part B: Engineering. 2012;43(2):317-24.
116. Brincker R, Zhang L, Andersen P, editors. Modal identification from ambient responses using frequency domain decomposition. Proc of the 18*'International Modal Analysis Conference (IMAC), San Antonio, Texas; 2000.
117. Kim BH, Stubbs N, Park T. A new method to extract modal parameters using output-only responses. Journal of sound and vibration. 2005;282(1-2):215-30.
118. Reddy JN. An introduction to the finite element method. New York. 1993;27.
119. Ferreira AJ. MATLAB codes for finite element analysis: solids and structures: Springer Science & Business Media; 2008.
120. Allemang RJ. The modal assurance criterion–twenty years of use and abuse. Sound and vibration. 2003;37(8):14-23.
121. Smith AL, Hicks SJ, Devine PJ. Design of floors for vibration: A new approach: SCI Publication P354, Ascot; 2009.
122. Sandun De Silva S, Thambiratnam DP. Dynamic characteristics of steel–deck composite floors under human-induced loads. Computers & Structures. 2009;87(17-18):1067-76.
123. Živanović S, Pavic A, Reynolds P. Vibration serviceability of footbridges under human-induced excitation: a literature review. Journal of Sound and Vibration. 2005;279(1-2):1-74.
124. Kerr S, Bishop N. Human induced loading on flexible staircases. Engineering Structures. 2001;23(1):37-45.
125. Pavic A, Reynolds P. Vibration serviceability of long-span concrete building floors. Part 1: Review of background information. Shock and Vibration Digest. 2002;34(3):191-211.
126. Racic V, Pavic A, Brownjohn JMW. Experimental identification and analytical modelling of human walking forces: Literature review. Journal of Sound and Vibration. 2009;326(1-2):1-49.
127. Mercier H, Ammann WJ, Deischl F, Eisenmann J, Floegl I, Hirsch GH, et al. Vibration problems in structures: practical guidelines: Birkhäuser; 2012.
128. Bachmann H, Ammann W. Vibrations in structures: induced by man and machines: Iabse; 1987.

129. Muhammad ZO, Reynolds P. Vibration serviceability of building floors: performance evaluation of contemporary design guidelines. Journal of Performance of Constructed Facilities. 2019;33(2):04019012.
130. Murray TM, Allen D, Ungar EE, Davis DB. Vibrations of steel-framed structural systems due to human activity: American Institute of Steel Construction; 2016.
131. Fanella D, Mota M. Design guide for vibrations of reinforced concrete floor systems. Concrete Reinforcing Steel Institute (CRSI): Schaumburg, IL, USA. 2014.
132. Willford MR, Young P, CEng M. A design guide for footfall induced vibration of structures: Concrete Society for The Concrete Centre; 2006.
133. Pavic A, Willford M. Vibration Serviceability of Posttensioned Concrete Floors. Post-Tensioned Concrete Floors Design Handbook. Appendix G, Technical Report 43; 2005.
134. Perry J, Davids JR. Gait analysis: normal and pathological function. Journal of Pediatric Orthopaedics. 1992;12(6):815.
135. Whittle MW. Gait analysis: an introduction: Butterworth-Heinemann; 2014.
136. Bachmann H, Ammann WJ, Deischl F, Eisenmann J, Floegl I, Hirsch GH, et al. Vibration problems in structures: practical guidelines: Birkhäuser; 2012.
137. Standardization IOf. Bases for Design of Structures--serviceability of Buildings and Walkways Against Vibrations: ISO; 2007.
138. Li Q, Fan J, Nie J, Li Q, Chen Y. Crowd-induced random vibration of footbridge and vibration control using multiple tuned mass dampers. Journal of Sound and Vibration. 2010;329(19):4068-92.
139. Kerr S. Human induced loading on staircases PhD thesis. University of London. 1998.
140. Willford M, Field C, Young P. Improved methodologies for the prediction of footfall-induced vibration. Building Integration Solutions2006. p. 1-15.
141. Young P, editor Improved floor vibration prediction methodologies. ARUP vibration seminar; 2001.
142. Gonilha JA, Correia JR, Branco FA. Dynamic response under pedestrian load of a GFRP–SFRSCC hybrid footbridge prototype: Experimental tests and numerical simulation. Composite Structures. 2013;95:453-63.
143. Behnia A, Chai HK, Ranjbar N, Behnia N. Finite element analysis of the dynamic response of composite floors subjected to walking induced vibrations. Advances in Structural Engineering. 2013;16(5):959-73.
144. Autralia S. Structural design actions Part 1: Permanent, imposed and other actions. AS/NZS 11701: 2002. 2002.
145. Osborne K, Ellis B. Vibration design and testing of a long-span lightweight floor[Lloyds Corporation 1958 building]. Structural Engineer. 1990;68:181-6.
146. Wyatt T. Design guide on the vibration of floors: Steel Construction Institute London; 1989.
147. De Silva SS, Thambiratnam DP. Dynamic characteristics of steel–deck composite floors under human-induced loads. Computers & Structures. 2009;87(17-18):1067-76.
148. Murray T. Floor vibrations: tips for designers of office buildings. Structure. 2000:26-30.
149. Elnimeiri M, Iyengar H, editors. Composite floor vibrations: predicted and measured. Steel Structures; 1989: ASCE.
150. Ellis B. On the response of long-span floors to walking loads generated by individuals and crowds. Structural Engineer. 2000;78(10):17-25.

151. Mudiyanselage A, Abeysinghe CM. Static and dynamic performance of lightweight hybrid composite floor plate system: Queensland University of Technology; 2012.

APPENDIX I

STATEMENTS OF THE CONTRIBUTION OF CO-SUTHORS

Statement of contrition of others

The experimental and analytical studies in this thesis was primarily designed and conducted by the candidate (Yanqiang Cui). Significant contributions to the works were also provided by co-authors. Contribution of the co-authors are described below.

Yanqiang Cui, Prof. Hong Hao, Associate Prof. Jun Li, and Dr. Wensu Chen defined the objectives of the proposed research and relevant methodologies. Experimental tests, results analysis, analytical studies, and numerical simulations were carried out by Yanqiang Cui. The manuscripts were written by Yanqiang Cui with revisions and editions from Prof. Hong Hao, Associate Prof. Jun Li, and Dr. Wensu Chen. All of them also provided additional intellectual input in the discussions of analysis and interpretations of results.

To whom it may concern

I, Yanqiang Cui, contributed experimental investigations, data analysis and wrote the manuscript which was revised and edited by the co-authors to the paper titled "**Effect of Adding Methylcellulose on Mechanical and Vibration Properties of Geopolymer Paste and Hybrid Fiber-Reinforced Geopolymer Composite**".

(__________)

I, as a co-author, endorse that this level of contribution by the candidate indicated above is appropriate.

(Prof. Hong Hao)	(___________)
(Associate Prof. Jun Li)	(___________)
(Dr. Wensu Chen)	(___________)